Aspects of Gravitational Clustering

THESIS SUBMITTED
By
Jayanti Prasad
FOR THE DEGREE OF
Doctor of Philosophy
IN
Physics
TO THE
University of Allahabad

Harish-Chandra Research Institute

Chhatnag Road, Jhunsi, Allahabad-211019

2008

CERTIFICATE

It is certified that the work incorporated in the thesis **Aspects of Gravitational Clustering** submitted by Mr. **Jayanti Prasad** was carried out by the candidate under my supervision at the **Harish-Chandra Research Institute** for the degree of **Doctor of Philosophy**. The work reported in this thesis is original and has not formed the basis of award of any degree or diploma of any University or Institution. Such material obtained from other sources has been duly acknowledged in the thesis.

Prof. Jasjeet Singh Bagla

(Thesis supervisor)

Jayanti Prasad

(Candidate)

Acknowledgments

There are many people in and outside HRI who have helped me to reach this stage.

First of all, I would like to thank my supervisor, Prof. Jasjeet Singh Bagla, for many insightful conversations during the development of the ideas in this thesis, and for being a constant source of encouragement and support. I would also like to thank all my instructors in HRI for the wonderful physics courses which they gave during our course work. I am indebted to Dr. L. Sriramkumar and Prof. T. R. Seshadri for their guidance and help at various stages. I would also like to thank all the members of the supporting staff at HRI for helping me to fix various practical problems.

I would always be grateful to my friends and colleagues in HRI who helped directly or indirectly to make HRI an interesting place to live and work in. I would specially like to thank Pomita Ghoshal for helping me in various ways.

I am grateful to SISSA (Italy) and ICTP (Italy) for sponsoring my Croatia trip for NOVICOSMO 2005 and ICTP trip for the Summer School in Astroparticle Physics 2006 respectively. Numerical experiments for this study were carried out at cluster computing facility in the Harish-Chandra Research Institute (http://cluster.hri.res.in). This research has made use of NASA's Astrophysics Data System (http://www.adsabs.harvard.edu/).

Abstract

Gravitational clustering leads to formation of galaxies, clusters of galaxies and other large scale structures in the universe. The main theme of this thesis is to study aspects of gravitational clustering in an expanding universe.

The primordial density fluctuations which are imprinted in the CMBR sky amplify due to gravity and lead to structure formation. As long as these fluctuations are small, they grow independently at various scales and their growth is correctly predicted by the linear perturbation theory. However, when fluctuations become large, mode coupling becomes important. Cosmological N-body simulations are the main tool for studying nonlinear gravitational clustering.

This thesis can be divided into two parts. In the first part (Chapter 2 and Chapter 3), we discuss consequences of mode coupling in nonlinear gravitational clustering and try to understand how perturbations at various scales affect the growth of one another. In particular we focus on the effects of perturbations at small scales (substructure) on the growth of perturbations at larger scales. In the second part (Chapter 4, Chapter 5 and Chapter 6) we study limitations of cosmological N-body simulations due to finite volume. We try to understand how size of the simulation volume affects various physical quantities of interest like two-point correlation function, mass function, formation and destruction rate, Skewness etc. A very short chapter-wise summary of the thesis is as follows.

In Chapter 1 we give an introduction of Friedmann-Robertson-Walker (FRW) model and discuss basics of structure formation required for the study. We start with an overview of observations of large scale structure of the universe and motivate FRW model in §1.1. A few generic solutions of the Friedmann's equations are discussed in §1.2. We discuss dynamics of objects in an expanding background and give a short introduction of mode coupling in §1.3. We introduce commonly used

statistical indicators of gravitational clustering like power spectrum, two-point correlation function and mass variance in §1.4. We discuss semi-analytical models of nonlinear gravitational clustering like spherical collapse model and Press-Schechter formalism in §1.5. We also give a brief introduction of the Zeldovich approximation and the adhesion approximation in §1.5. We end this chapter with an overview of cosmological N-body simulations in §1.6.

In Chapter 2 we address the issue of mode coupling in nonlinear gravitational clustering and ask how presence of small scale perturbations (substructure) affects the growth of perturbations at large scales. We study the collapse of a plane wave, which represents a large scale perturbation, in the presence and absence of substructure (Bagla, Prasad & Ray, 2005). We find that the plane wave collapses to a thin sheet (pancake) which gets thinner when small scale perturbations are introduced isotropically. We conclude that the scattering between clumps (formed due to collapse of small scale perturbations) helps in the dynamical relaxation of the plane wave and the pancake becomes thinner. Apart from this, in this study we also try to model the effects of small scale perturbations in the form of artificial viscosity. Applying the Burger's equation, we find that it is possible to find a common value of viscosity for every multistream region which forms due to the collapse of the plane wave.

In Chapter 3 we study the role of substructure in gravitational clustering using a set of numerical experiments i.e., cosmological N-body simulations (Bagla & Prasad, 2008). In this study we consider models which are more general than the models which we have considered in the earlier study (Chapter 2) for our investigations. We simulate the collapse of a pure power law model ($n = -1$) and considering it as the reference model we also simulate two other models in which we either suppress or enhance power at small scales. We analyze our results using visual comparison (slices), two point correlation function, Skewness and number density. We find that the effects of substructure on the collapse of perturbations at larger scales are not as significant in a general case as they are in the case of planar collapse.

The second part of this thesis contains results of our investigation of effects of finite box size in cosmological N-body simulations. In Chapter 4 we present a prescription for estimating the errors in various physical quantities of interest due to finite size of cosmological N-body simulations (Bagla & Prasad, 2006). We mainly focus on corrections in mass variance, mass function, multiplicity function and comoving number density in this chapter. We also discuss the applications of our prescription for a power law ($n = -2$) and LCDM models. We show that the number density of low mass haloes is overestimated when the size of the simulation box is reduced at the expense of the density of more massive haloes. We also show that the correction due to finite box size is maximum at the scale of nonlinearity for mass function and falls at small and large scales. The main conclusion which we draw from this study is that simulations with little or no power at large scales are not affected by the finite size of the simulation box. For other models the effects of a finite box size are important.

We continue our investigation of effects of finite box size in cosmological N-body simulations in Chapter 5. We begin with a quick review of the Press-Schechter formalism and following the prescription of (Sasaki, 1994) show that the rate of change of number density of haloes, in a given mass range around a mass scale, can be split into formation rate (the rate at which haloes in that mass range form due to merging of smaller haloes) and the destruction rate (the rate at which haloes in that mass mass range merge and form bigger haloes). Following the formalism which we have developed in Chapter 4, in this chapter we give analytic expressions for correction in formation and destruction rate and discuss their application for power law ($n = -2$) and LCDM models (Prasad, 2007). We also apply our formalism to find corrections in merger rate.

In Chapter 6 we study the effects of box size on Skewness and present a detailed comparison of our analytical results with N-body simulations (Bagla, Prasad & Khandai, 2008). We compute average two point correlation function, Skewness and number density of collapsed haloes and compare these with N-body simulations. We have found that in most cases theoretical estimates fit the results of simulations. We also give an analytic expression for corrections in Kurtosis (S_4) and study the effects of finite volume of cosmological simulations on pair velocity.

This thesis is based on the following publications:

1. Bagla J.S., Prasad J. and Ray S. 2005, MNRAS **360**, 194 (astro-ph/0408429)
   Gravitational collapse in an expanding background and the role of substructure I: Planar collapse.

2. Bagla J.S. and Prasad J 2008, Submitted to MNRAS (arXiv:0802.2796 [astro-ph])
   Gravitational collapse in an expanding background and the role of substructure II: Excess

power at small scales and its effect on collapse of structures at large

3. Bagla J.S. and Prasad J. 2006, MNRAS **370**, 993 (astro-ph/0601320)
   Effects of the size of cosmological N-Body simulations on physical quantities – I: Mass Function.

4. Prasad J. 2007, J. Astrophys. Astr. **28**, 117 (astro-ph/0702557)
   Effects of the size of cosmological N-Body simulations on physical quantities –II: Formation and destruction rate.

5. Bagla J.S., Prasad J. and Khanadai N., 2008, Submitted to MNRAS (arXiv:0804.1197[astro-ph])
   Effects of the size of cosmological N-Body simulations on physical quantities – III: Skewness

Contents

List of Figures

Chapter 1

Introduction

Observations show that galaxies in the universe are moving away from each other due to expansion of the universe (Hubble expansion), discovered by Edwin Hubble (Hubble, 1929). If we extrapolate the density and temperature of the universe back in time then they diverge at a moment of time in the past, called the big bang.

The matter distribution in the universe at very large scale is uniform, however, at small scales it is highly clustered. The earliest measurement of fluctuations in the universe is in the form of temperature anisotropies of Cosmic Microwave Background Radiation (CMBR). The presence of anisotropies in the CMBR at all scales measured by WMAP and other experiments shows that the matter and radiation distribution in the early universe was not perfectly uniform; there were fluctuations of the order of one part in 10^5 (Smoot et al., 1992; Hinshaw et al., 2003; Hinshaw et al., 2007). Gravitational amplification of the primordial density perturbations imprinted in the CMBR is generally assumed to be responsible for structure formation in the universe (Peebles, 1980; Peebles, 1993; Padmanabhan, 1993; Liddle & Lyth, 2000; Bernardeau et al., 2002; Padmanabhan, 2002; Peacock, 1999).

The homogeneous and isotropic model of the universe, called the Friedmann-Robertson-Walker (FRW) model, is introduced in §1.1. Some of the important solutions of FRW model are discussed in §1.2. We discuss the dynamics of particles in an expanding background and mode coupling in nonlinear gravitational clustering in §1.3. Some of the important statistical measures of gravitational clustering are discussed in §1.4. We give an overview of various aspects of nonlinear gravitational clustering in §1.5. A brief overview of cosmological N-body simulations is given in §1.6.

1.1 Friedmann-Robertson-Walker (FRW) model

Gravity is the main force at very large scales and is described by Einstein's field equation of general relativity.

$$R_{\mu\nu} - \frac{1}{2}Rg_{\mu\nu} = \frac{8\pi G}{c^4}T_{\mu\nu} \tag{1.1}$$

Here $R_{\mu\nu}$ is the curvature tensor which represents the geometrical structure of the universe and $T_{\mu\nu}$ is the energy-momentum tensor which represents the various species of matter and energy in the universe.

The universe at very large scales is homogeneous and isotropic (cosmological principle). As a result of homogeneity and isotropy at large scales the geometrical structure of the universe is given by the following space-time metric called the FRW metric (Friedmann, 1922; Robertson, 1929; Walker, 1936; Lematre, 1931a; Lematre, 1931b)

$$ds^2 = c^2dt^2 - a^2(t)\left[\frac{dr^2}{1-kr^2} + r^2(d\theta^2 + \sin^2\theta d\phi^2)\right] \tag{1.2}$$

The FRW metric is characterized by two parameters named the spatial curvature or the curvature constant k and the time dependent function $a(t)$ called the scale factor. As a consequence of general theory of relativity the functional form of $a(t)$ depends on the matter and energy content of the universe and the value of the curvature constant k depends on the total energy content of the universe. If we normalize the scale factor appropriately then k can take one of the three values $0, \pm 1$.

The FRW metric can also be written in the following form :

$$ds^2 = a^2[d\eta^2 - \{d\chi^2 + r^2(d\theta^2 + \sin^2\theta d\phi^2)\}] \tag{1.3}$$

where η (called conformal time) and χ are defined as follows.

$$\eta = \int \frac{cdt}{a(t)} \quad \text{and} \quad \chi = \begin{cases} r, & \text{for } k = 0; \\ \sin^{-1} r, & \text{for } k = 1; \\ \sinh^{-1} r, & \text{for } k = -1; \end{cases} \tag{1.4}$$

The matter and energy in the universe can be taken in the form of a perfect fluid which is characterized by the following energy-momentum tensor $T_{\mu\nu}$ in a coordinate system in which the fluid remains stationary i.e., the comoving frame

$$T_{\mu\nu} = \rho V_\mu V_\nu - P(g_{\mu\nu} - V_\mu V_\nu) \tag{1.5}$$

Here $V_\mu = (1,0,0,0)$ is the four velocity of the fluid and ρ and P are its energy density and pressure respectively.

1.1.1 Friedmann equations

On the basis of the FRW metric (equation (1.2)) and the energy-momentum tensor for a perfect fluid (equation (1.5)), Einstein field equation (1.1) can be written in terms of the following pair of equations called the Friedmann equations

$$\frac{\dot{a}^2}{a^2} + \frac{k}{a^2} = \frac{8\pi G\rho}{3} \tag{1.6}$$

and

$$2\frac{\ddot{a}}{a} + \left(\frac{\dot{a}^2}{a^2} + \frac{k}{a^2}\right) = -8\pi GP \tag{1.7}$$

Using equation (1.6) we can rewrite equation (1.7) in the following form:

$$\frac{\ddot{a}}{a} = -\frac{4\pi G}{3}(\rho + 3P) \tag{1.8}$$

The Friedmann equations (1.6) and (1.8) are generally written in terms of the Hubble parameter $H(t)$, the density parameter $\Omega(t)$ and the deceleration parameter $q(t)$ which are defined as follow:

$$H(t) \equiv \frac{1}{a(t)}\frac{da(t)}{dt} = \frac{\dot{a}}{a}; \quad \Omega(t) = \frac{\rho(t)}{\rho_c(t)} \text{ where } \rho_c(t) = \frac{3H^2(t)}{8\pi G}; \quad q(t) = -\frac{a(t)\ddot{a}(t)}{\dot{a}(t)^2} \tag{1.9}$$

Here $\rho_c(t)$ is called the critical density. In terms of these parameters equation (1.6) can be written as

$$k = H^2 a^2(\Omega - 1) \tag{1.10}$$

by convention

$$k = \begin{cases} 0; & \text{for } \rho = \rho_c \text{ or } \Omega = 1 \\ 1; & \text{for } \rho > \rho_c \text{ or } \Omega > 1 \\ -1; & \text{for } \rho < \rho_c \text{ or } \Omega < 1 \end{cases} \tag{1.11}$$

The universe is said to be spatially flat, closed and open for $k = 0, 1$ and -1 respectively. Equation (1.8) can be written as

$$q = \frac{3\Omega}{2}(\frac{1}{3} + w) \tag{1.12}$$

Equation (1.12) shows that the expansion of the universe slows down with time i.e., decelerates for $w > -1/3$.

Friedmann equations (1.6) and (1.8), do not have any stationary solution. In order to get such solution, Einstein added a constant Λ called the cosmological term in the field equation (1.1). This term was abandoned soon after the discovery of the expansion of the universe and was assumed to be zero. However, recent observations have shown that this is not the case, i.e., this term is nonzero. When we consider a nonzero cosmological constant then we get the following set of the Friedmann equations

$$\frac{\dot{a}^2}{a^2} + \frac{k}{a^2} = \frac{8\pi G\rho}{3} + \frac{\Lambda}{3} \tag{1.13}$$

and

$$\frac{\ddot{a}}{a} = -\frac{4\pi G}{3}(\rho + 3P) + \frac{\Lambda}{3} \tag{1.14}$$

Friedmann equations (1.13) and (1.14). have three unknown variables $a(t), \rho(t)$ and $p(t)$ and in order to make this system closed one more equation is needed which can be taken in the form of the following energy conservation equation

$$d(\rho a^3) = -Pd(a^3) \tag{1.15}$$

Substituting $P = w\rho$, the above equation can be solved as

$$\rho(a) \propto a^{-3(1+w)} \tag{1.16}$$

for specific values of w:

$$\rho(a) \propto \begin{cases} \frac{1}{a^3}; & \text{for nonrelativistic matter } (w = 0) \\ \frac{1}{a^4}; & \text{for relativistic matter } (w = 1/3) \\ \text{constant;} & \text{for cosmological constant } (w = -1) \end{cases} \tag{1.17}$$

using equation (1.17), Friedman equation (1.13) can be written as

$$H^2(t) = H_0^2 \left[\Omega_m \left(\frac{a_0}{a}\right)^3 + \Omega_r \left(\frac{a_0}{a}\right)^4 + \Omega_\Lambda + (1 - \Omega) \left(\frac{a_0}{a}\right)^2\right] \tag{1.18}$$

1.1.2 Cosmological redshift

The observed wavelength λ_{obs} of electromagnetic waves which we receive at time $t = t_{obs}$ from the distant parts of the universe is found to be greater than their emitted wavelength λ_{em} due to expansion of the universe. This is called the cosmological redshift ($z = \lambda_{obs}/\lambda_{em} - 1$). In order to find a relation between the scale factor $a(t)$ and cosmological redshift z, we consider a source of light at a radial distance r from an observer and assume that the source emits two pulses of light at time t_{em} and $t_{em} + dt_{em}$ and they are received by the observer at time t_{obs} and $t_{obs} + dt_{obs}$ respectively then from equation (1.2)

$$\int_0^r \frac{dr'}{\sqrt{1-kr'^2}} = \int_{t_{em}}^{t_{obs}} \frac{cdt'}{a(t')} = \int_{t_{em}+dt_{em}}^{t_{obs}+dt_{obs}} \frac{cdt'}{a(t')} \tag{1.19}$$

which gives (Weinberg, 1972)

$$\frac{dt_{obs}}{dt_{em}} = \frac{a(t_{em})}{a(t_{obs})} \tag{1.20}$$

because the comoving distance between the two points does not change.

If the the actual wavelength of light pulse is λ_{em} and we observe it at wavelength λ_{obs} then

$$1+z = \frac{\lambda_{obs}}{\lambda_{em}} = \frac{\nu_{em}}{\nu_{obs}} = \frac{dt_{obs}}{dt_{em}} = \frac{a(t_{obs})}{a(t_{em})} = \frac{1}{a} \tag{1.21}$$

1.2 Solutions of the Friedmann equations

1.2.1 Einstein-de Sitter model

This is the simplest cosmological model and we will use it for most of the studies in the present thesis. If we consider a flat cosmological model i.e., $k = 0$ and assume $\Omega_r = \Omega_\Lambda = 0, \Omega_m = 1$ then the Friedmann equation (1.6) can be easily solved in the following form

$$a(t) = a(t_0)\left(\frac{t}{t_0}\right)^{2/3} \quad \text{where} \quad t_0 = \frac{2}{3H_0} \tag{1.22}$$

1.2.2 Closed and open models

In the case of closed matter dominated model, i.e., $\Omega_m > 1$, Friedmann equation (1.6) can be written as

$$\frac{\dot{a}^2}{a^2} = H_0^2 \left[\Omega_m \left(\frac{a_0}{a} \right)^3 + (1 - \Omega_m) \left(\frac{a_0}{a} \right)^2 \right]$$

This equation can be easily solved in the following parametric form

$$\begin{aligned} a &= \frac{a_{max}}{2} (1 - \cos\theta)\, ; \;\; a_{max} = a(t_0) \left(\frac{\Omega_m}{\Omega_m - 1} \right) \\ t &= \frac{t_{max}}{\pi} (\theta - \sin\theta)\, ; \;\; t_{max} = \frac{\Omega_m}{2H_0(\Omega_m - 1)^{3/2}} \end{aligned} \tag{1.23}$$

From the above equations we note that in this case the universe starts expansion at the big bang ($\theta = 0$), reaches a maximum size ($\theta = \pi$) and finally collapses in a big crunch ($\theta = 2\pi$).

In the case of matter dominated open universe i.e., $\Omega_m < 1$ or $k = -1$, we get the following parametric solutions.

$$\begin{aligned} a &= \frac{a_{max}}{2} (\cosh\theta - 1)\, ; \;\; a_{max} = a(t_0) \left(\frac{\Omega_m}{1 - \Omega_m} \right) \\ t &= \frac{t_{max}}{\pi} (\sinh\theta - \theta)\, ; \;\; t_{max} = \frac{\Omega_m}{2H_0(1 - \Omega_m)^{3/2}} \end{aligned} \tag{1.24}$$

In this case the universe keeps expanding forever.

1.3 Cosmological density field

1.3.1 Dynamics of particles in an expanding universe

In a homogeneous and isotropic universe cosmological objects move only due to the expansion of the universe. In presence of density fluctuations gravitational force due to these fluctuations plays an important role in the dynamics.

In absence of clustering, the distance $\mathbf{r}(t)$ between any two objects in the universe changes as :

$$\mathbf{r}(t) \propto a(t) \;\text{ or }\; \mathbf{r}(t) = a(t)\mathbf{x}$$

Here $\mathbf{x}$ is comoving distance and it does not change with time for a homogeneous and isotropic universe. However, when there is clustering of matter

$$\mathbf{r}(t) = a(t)\mathbf{x}(t) \tag{1.25}$$

and velocity is given by

$$\dot{\mathbf{r}}(t) = \dot{a}(t)\mathbf{x}(t) + a(t)\dot{\mathbf{x}}(t) = \mathbf{v}_h + \mathbf{v}_p \tag{1.26}$$

The above equation shows that one part of the velocity of objects is contributed by the expansion of the universe i.e., $\mathbf{v}_h$, and another part $\mathbf{v}_p$, called the peculiar velocity, is contributed by the gravitational force due to density fluctuations. The gravitational potential that drives the dynamics can also be split into two parts, ϕ_b due to the smooth universe and ϕ due to density fluctuations around the smooth background.

From equation (1.26) we can write

$$\ddot{\mathbf{r}}(t) = \ddot{a}(t)\mathbf{x}(t) + 2\dot{a}(t)\dot{\mathbf{x}}(t) + a\ddot{\mathbf{x}}(t) = -\nabla(\phi_b + \phi) \tag{1.27}$$

The terms corresponding to the background expansion are identified as

$$\ddot{a}(t)\mathbf{x}(t) = -\nabla_r\phi_b(t) \quad \text{or} \quad \phi_b(t) = -\frac{1}{2}a(t)\ddot{a}(t)x^2 \tag{1.28}$$

The remaining parts represent the equation of motion of the object due density fluctuations

$$a\ddot{\mathbf{x}}(t) + 2\dot{a}(t)\dot{\mathbf{x}}(t) = -\nabla_r\phi \tag{1.29}$$

or

$$\frac{d^2\mathbf{x}(t)}{dt^2} + 2\frac{\dot{a}(t)}{a(t)}\frac{d\mathbf{x}(t)}{dt} = -\frac{\nabla_r\phi(\mathbf{x},t)}{a(t)} = -\frac{\nabla_x\phi(\mathbf{x},t)}{a^2(t)} \tag{1.30}$$

and in terms of the peculiar velocity $\mathbf{v}_p = \mathbf{v}$:

$$\frac{d\mathbf{v}(t)}{dt} + \frac{\dot{a}(t)}{a(t)}\mathbf{v}(t) = -\frac{\nabla_x\phi(\mathbf{x},t)}{a(t)} \tag{1.31}$$

This equation also shows that when the distribution of matter is uniform, the peculiar velocity decays as $\mathbf{v}(t) \propto 1/a(t)$ with the expansion of the universe. In such a case there is no gravitational process for generating $\mathbf{v}$.

1.3.2 Mode coupling

The cosmological density perturbations are characterized by density contrast $\delta(x,t)$ which is defined as follows

$$\delta(\mathbf{x},t) = \frac{\rho(\mathbf{x},t) - \rho_b(t)}{\rho_b(t)} \tag{1.32}$$

Here $\rho_b(r)$ is the average density of the universe.

The gravitational potential $\phi(\mathbf{x},t)$ due density fluctuations is given by

$$\nabla_x^2 \phi(\mathbf{x},t) = 4\pi G \rho_b(t) a^2 \delta(\mathbf{x},t) \tag{1.33}$$

and due to smooth background

$$\nabla_x^2 \phi_b(t) = 4\pi G \rho_b(t) a^2 \tag{1.34}$$

In a flat cosmological model $(k = 0)$ the density contrast $\delta(\mathbf{x},t)$ can be decomposed into its fourier components

$$\delta(\mathbf{x},t) = \int \frac{d^3\mathbf{k}}{(2\pi)^3} \delta_{\mathbf{k}}(t) \exp(i\mathbf{k}.\mathbf{x}) \tag{1.35}$$

and inverse transform

$$\delta_{\mathbf{k}}(t) = \int \frac{d^3\mathbf{x}}{V} \delta(\mathbf{x},t) \exp(-i\mathbf{k}.\mathbf{x}) \tag{1.36}$$

We can consider the density field to represent an underlying distribution of point particles

$$\rho(\mathbf{x},t) = \frac{1}{a^3(t)} \sum_{i=1}^{N} m_i \delta_D(\mathbf{x} - \mathbf{x}_i(t)) \tag{1.37}$$

Where δ_D is the Dirac delta function. The average density $\rho_b(t)$ can then be written as

$$\rho_b(t) = \frac{1}{V} \int d^3\mathbf{x} \rho(\mathbf{x},t) = \frac{M}{Va^3}; \text{ where } M = \sum_{i=1,N} m_i \tag{1.38}$$

and the density contrast

$$\delta(\mathbf{x},t) = \frac{\rho(\mathbf{x},t)}{\rho_b(t)} - 1 = \frac{V}{M} \sum_{i=1,N} m_i \delta_D(\mathbf{x} - \mathbf{x}_i) - 1 \tag{1.39}$$

or in fourier space

$$\delta_{\mathbf{k}}(t) = \frac{1}{M} \sum_{i=1,N} m_i \exp(-i\mathbf{k}.\mathbf{x}_i) - \delta_D^3(\mathbf{k}) \tag{1.40}$$

from equation (1.40) we can write

$$\ddot{\delta}_{\mathbf{k}} + 2\frac{\dot{a}}{a}\delta_{\mathbf{k}} = \frac{1}{M}\sum_{i=1,N} m_i \left[-i\mathbf{k}.\left(\ddot{\mathbf{x}}_i + 2\frac{\ddot{a}}{a}\dot{\mathbf{x}}_i\right) - (\mathbf{k}.\mathbf{x}_i)^2\right]\exp(-i\mathbf{k}.\mathbf{x}_i)$$

The RHS of the above equation can be simplified using equation (1.30)

$$\ddot{\delta}_{\mathbf{k}} + 2\frac{\dot{a}}{a}\delta_{\mathbf{k}} = \frac{1}{M}\sum_{i=1,N} m_i \left[-i\mathbf{k}.\left(-\frac{\nabla\phi_i}{a^2}\right) - (\mathbf{k}.\mathbf{x}_i)^2\right]\exp(-i\mathbf{k}.\mathbf{x}_i) \tag{1.41}$$

From Poisson equation (1.33) we can write

$$-\frac{\nabla_x\phi(\mathbf{x})}{a^2} = 4\pi G\sum_{k\neq 0}\frac{i\mathbf{k}\delta_{\mathbf{k}}(t)}{k^2}\exp(i\mathbf{k}.\mathbf{x})$$

and so equation (1.41) can be written as

$$\ddot{\delta}_{\mathbf{k}} + 2\frac{\dot{a}}{a}\dot{\delta}_{\mathbf{k}} = 4\pi G\rho_b\delta_{\mathbf{k}} + A_{\mathbf{k}} - B_{\mathbf{k}} \tag{1.42}$$

where

$$A_{\mathbf{k}} = 2\pi G\rho_b \sum_{\mathbf{k}'\neq 0,\mathbf{k}\neq\mathbf{k}'}\left[\frac{\mathbf{k}'.\mathbf{k}}{|\mathbf{k}'|^2} + \frac{\mathbf{k}.(\mathbf{k}-\mathbf{k}')}{|\mathbf{k}-\mathbf{k}'|^2}\right]\delta_{\mathbf{k}'}\delta_{\mathbf{k}-\mathbf{k}'} \tag{1.43}$$

and

$$B_{\mathbf{k}} = \frac{1}{M}\sum_{i=1,N} m_i(\mathbf{k}.\dot{\mathbf{x}}_i)^2\exp(-i\mathbf{k}.\mathbf{x}_i) \tag{1.44}$$

Here $A_{\mathbf{k}}$ and $B_{\mathbf{k}}$ characterize mode coupling between different scales in non linear gravitational clustering. From equation (1.42) we observe that for all $\mathbf{k}$ with $A_{\mathbf{k}} - B_{\mathbf{k}} = 0$, perturbations at various scales evolve independently and the equation can be easily solved analytically i.e., the linear regime. However, for a general case equation (1.42) cannot be solved analytically unless $A_{\mathbf{k}} - B_{\mathbf{k}} = 0$.

1.3.3 Linear limit

In the case when amplitude of density perturbation is small i.e., $\delta_k \ll 1$, we neglect the mode coupling and write equation (1.42) as

$$\ddot{\delta}_{\mathbf{k}} + 2\frac{\dot{a}}{a}\dot{\delta}_{\mathbf{k}} = 4\pi G\rho_b\delta_{\mathbf{k}} \tag{1.45}$$

Equation (1.45) can be easily solved for an Einstein-de Sitter model i.e., $a(t) \propto t^{2/3}$ and $\rho_0 = 1/6\pi G t^2$.

$$\delta_{\mathbf{k}}(t) = At^{2/3} + Bt^{-1} \quad \text{or} \quad \delta_{\mathbf{k}}(a) = Aa + Ba^{-3/2} \tag{1.46}$$

Note that the first part of the above equation can be identified with the growing mode and the second part with the decaying mode. It can be shown that the Hubble parameter $H(t)$ which is given by equation (1.18) is also a solution of equation (1.45) and coincides with the decaying solution (if $\Omega_r = 0$ and $w_{de} = -1$). Using the method of Wronskian the growing solution $b(t)$ can be written as

$$b(t) \propto \frac{X^{1/2}}{a} \int^{a} \frac{da}{X^{3/2}}; \; X = \frac{a^2 H^2}{H_0^2} \tag{1.47}$$

For a flat cosmological model with nonrelativistic matter and cosmological constant

$$X = 1 + \Omega_m \left(\frac{1}{a} - 1 \right) + \Omega_\Lambda (a^2 - 1) \tag{1.48}$$

If we use the growing solution $b(t)$ as a "time" parameter then the equation of motion (1.31) can be written as

$$\frac{d\mathbf{u}}{db} = -\frac{3}{2}\frac{Q}{b}(\mathbf{u} - \mathbf{g}) \tag{1.49}$$

where

$$\mathbf{u} = \frac{d\mathbf{x}}{db}; \; \mathbf{g} = -\nabla\psi \text{ where } \psi = \frac{2}{3H_0^2\Omega_m}\phi; \text{ and } Q = \left(\frac{\rho_b}{\rho_c}\right)\left(\frac{\dot{a}b}{a\dot{b}}\right)^2 \tag{1.50}$$

1.4 Statistical measures of gravitational clustering

1.4.1 Two point correlation function and power spectrum

In a uniform (Poisson) distribution of point particles with average number density $\bar{n}$, the joint probability $dP(1,2)$ of finding two particles in two infinitesimal volume elements δV_1 and δV_2 around positions $\mathbf{r}_1$ and $\mathbf{r}_2$ respectively is given by

$$dP(1,2) = \bar{n}^2 \delta V_1 \delta V_2 \tag{1.51}$$

In this case the probability of finding a particle in a volume element δV_1 is independent of the probability of finding a particle in a volume element δV_2. However, this is not the case when there is clustering of particles and the joint probability is modified

$$dP(1,2) = \bar{n}^2 \delta V_1 \delta V_2 \left[1 + \xi(\mathbf{r}_1, \mathbf{r}_2)\right] \tag{1.52}$$

Here $\xi(\mathbf{r}_1,\mathbf{r}_2)$ is called the two point correlation function which can depend on $\mathbf{r}_1$ and $\mathbf{r}_2$ only through $|\mathbf{r}_1-\mathbf{r}_2|$ for a statistically homogeneous and isotropic distribution of points i.e., $\xi(\mathbf{r}_1,\mathbf{r}_2)=\xi(|\mathbf{r}_1-\mathbf{r}_2|)=\xi(|\mathbf{r}_{12}|)$. The two point correlation function $\xi(r)$ can also be defined in terms of the conditional probability $dP(1|2)$ of finding a particle (labeled “1”) in an infinitesimal volume δV around the position $\mathbf{r}$ given that there is another particle (labeled “2”) at $\mathbf{r}=0$.

$$dP(1|2)=\bar{n}\delta V\left[1+\xi(\mathbf{r})\right] \tag{1.53}$$

The two point correlation function $\xi(r)$ and density contrast $\delta(\mathbf{x})$ are related as

$$\xi(r)=\langle\delta(\mathbf{x}+\mathbf{r})\delta(\mathbf{x})\rangle \tag{1.54}$$

Here averaging is done over an ensemble of large spatial regions of the universe that are statistically independent from each other. If we write density contrasts $\delta(\mathbf{x}+\mathbf{r})$ and $\delta(\mathbf{x})$ in terms of Fourier components and simplify equation (1.54) we get

$$\xi(r)=\int\frac{d^3\mathbf{k}}{(2\pi)^3}P(k)\exp(i\mathbf{k}.\mathbf{r}) \tag{1.55}$$

Here $P(k)$ is called the power spectrum and is defined as

$$\langle\delta_{\mathbf{k}}\delta^{\star}_{\mathbf{k}'}\rangle=(2\pi)^3\delta_D^{(3)}(\mathbf{k}-\mathbf{k}')P(k) \tag{1.56}$$

Where $\delta_D^{(3)}(\mathbf{k}-\mathbf{k}')$ is the Dirac delta function. The two point correlation function $\xi(\mathbf{r})$ and power spectrum $P(k)$ are the two most important statistical measures used to study gravitational clustering. This is because in the case when cosmological perturbations are Gaussian, their statistical properties can be completely characterized by the two point correlation function $\xi(\mathbf{r})$ or power spectrum $P(k)$.

1.4.2 Mass variance

As a result of the homogeneity and isotropy of the universe the first moment or mean $<\delta>$ of the density contrast $\delta(\mathbf{x})$ vanishes. However, the second moment is nonzero and is given by

$$\sigma_\delta^2=\langle\delta^2\rangle=\frac{1}{2\pi^2}\int dkk^2P(k) \tag{1.57}$$

The above equation shows that σ_δ^2 does not converge for most power spectra and it does not contain information about the contribution of perturbations at various scales. Therefore, it is more useful to represent the second moment by mass variance $\sigma^2(r)$, which is the variance of the mass inside cells of various sizes, after smoothing the density by a window function W.

$$\sigma^2(r) = \frac{\langle (M- < M >)^2 \rangle}{< M >^2} = \frac{< \delta M^2 >}{< M >^2} = \frac{1}{2\pi^2} \int dk k^2 P(k) |W(k,r)|^2 \tag{1.58}$$

where $M = 4\pi\rho r^3/3$. For a spherical-top hat window $W(k,r)$ is given by

$$W(k,r) = 3\left(\frac{\sin kr - kr\cos kr}{k^3 r^3}\right) \tag{1.59}$$

and in real space

$$W(|x-x'|,r) \begin{cases} \frac{3}{4\pi r^3}; & \text{for } \; |x-x'| < r \\ 0; & \text{Otherwise} \end{cases} \tag{1.60}$$

It is more useful to express $\sigma^2(r)$ in the following form

$$\sigma^2(r) = \int \frac{dk}{k}\left(\frac{k^3 P(k)}{2\pi^2}\right)|W(k,r)|^2 = \int \frac{dk}{k}\Delta^2(k)|W(k,r)|^2 \tag{1.61}$$

In the above equation $\Delta^2(k) = k^3 P(k)/2\pi^2$ is called the dimensionless power spectrum which represents the power per logarithmic interval in k.

For a power law model i.e., $P(k) \propto k^n$ we get the following scaling relationship

$$\sigma^2(r) \propto r^{-(n+3)} \quad \text{and} \quad \sigma^2(M) \propto M^{-(n+3)/3} \tag{1.62}$$

or

$$\sigma^2(r) = \left(\frac{r}{r_{nl}}\right)^{-(n+3)} \quad \text{and} \quad \sigma^2(M) = \left(\frac{M}{M_{nl}}\right)^{-(n+3)/3} \tag{1.63}$$

Where the scale of nonlinearity r_{nl} is identified with the scale at which mass variance σ^2 becomes unity.

1.4.3 N-point correlation functions

We can generalize the definition of the two point correlation function as given by equation (1.52) and define the N-point correlation function $\xi_N(\mathbf{r}_1, \mathbf{r}_2, .., \mathbf{r}_n)$ in terms of the joint probability of finding particles in infinitesimal volume elements $\delta V_1, \delta V_2, ..., \delta V_N$ around the positions $\mathbf{r}_1, \mathbf{r}_2, ..., \mathbf{r}_N$ respectively.

We get the following equation for three point correlation function corresponding to equation (1.52)

$$dP(1,2,3) = \bar{n}^3 \delta V_1 \delta V_2 \delta V_3 \left[1 + \xi(1,2) + \xi(2,3) + \xi(3,1) + \zeta(1,2,3)\right] \tag{1.64}$$

Here ξ and ζ are two and three point correlation functions respectively.

The N-point correlation functions $\xi_N(\mathbf{r}_1, \mathbf{r}_2, ...\mathbf{r}_N)$ can also be written in terms of the connected parts of the joint ensemble average of density contrast $\delta(r)$ at N different spatial points $\mathbf{r}_1, \mathbf{r}_2, ..., \mathbf{r}_N$ (Bernardeau et al., 2002).

$$\xi_N(\mathbf{r}_1, \mathbf{r}_2, ...\mathbf{r}_N) = \langle \delta(\mathbf{r}_1)\delta(\mathbf{r}_2)...\delta(r_N)\rangle_c \tag{1.65}$$

If we represent density contrasts at positions $\mathbf{r}_1, \mathbf{r}_2, ..., \mathbf{r}_N$ by $\delta_1, \delta_2, ..., \delta_N$ respectively, then some of the low order correlation functions are as follows

$$\xi(\mathbf{r}_1, \mathbf{r}_2) = \langle \delta_1 \delta_2 \rangle_c = \langle \delta_1 \delta_2 \rangle - \langle \delta_1 \rangle_c \langle \delta_2 \rangle_c \tag{1.66}$$

$$\begin{aligned} \zeta(\mathbf{r}_1, \mathbf{r}_2, \mathbf{r}_3) &= \langle \delta_1 \delta_2 \delta_3 \rangle_c \\ &= \langle \delta_1 \delta_2 \delta_3 \rangle - \langle \delta_1 \delta_2 \rangle_c \langle \delta_3 \rangle_c - \langle \delta_2 \delta_3 \rangle_c \langle \delta_1 \rangle_c - \langle \delta_3 \delta_1 \rangle_c \langle \delta_2 \rangle_c - \langle \delta_1 \rangle_c \langle \delta_2 \rangle_c \langle \delta_3 \rangle_c \end{aligned} \tag{1.67}$$

The N-point correlation functions $\xi_N(\mathbf{r}_1, \mathbf{r}_2, ..., \mathbf{r}_N)$ are also called the *reduced N-point correlation functions* since they depend only on the fully connected parts of the graphs representing the complete correlations.

On the basis of the ensemble average of various power of density contrast at the same position, we can also define the moments of density contrast in the following way

$$\begin{aligned} m_1 &= < \delta >_c = < \delta > \\ m_2 &= < \delta^2 >_c = < \delta^2 > - < \delta >_c^2 \\ m_3 &= < \delta^3 >_c = < \delta^3 > -3 < \delta^2 >_c^2 < \delta >_c - < \delta >_c^3 \end{aligned} \tag{1.68}$$

When the density field is Gaussian, its statistical properties can be completely characterized by the two point correlation function and the power spectrum. However, for a non-Gaussian case we need to specify correlation functions of all orders. It has been found that even if we begin with a purely Gaussian random field, gravitational clustering can generate non-Gaussianity and in that case higher moments are also needed to completely characterize the statistical properties of the density field.

1.4.4 The moments of counts in cells

Apart from the N-point correlation functions ξ_N, the statistical properties of cosmological density field for a general case can be represented by the moments of the number of objects (counts) in cells of different size (Peebles, 1980). In order to compute the moments of counts we put cells of equal size around the positions of randomly chosen particles and count the number of particles in these cells. In general, we divide cells into sub-cells that are sufficiently small such that a sub-cell can have either zero or one particle.

If we consider a sub-cell labeled by 'i' having n_i particles (1 or 0) in its volume dV_i and consider that the average density of particles is $\bar{n}$, then

$$\bar{n}dV_i = \langle n_i \rangle = \langle n_i^2 \rangle = \langle n_i^3 \rangle .... \tag{1.69}$$

The total number of particles in a cell (count) is given by

$$N = \sum_i n_i \tag{1.70}$$

From the above equation, the first moment of counts in cells μ_1 (mean) can be written as

$$\mu_1 = \langle N \rangle = \sum_i \langle n_i \rangle = \bar{n}V \tag{1.71}$$

Here $\bar{n}$ is the average number density of particles and V is the volume of the cell. In order to compute the second moment μ_2, we need to compute

$$\langle N^2 \rangle = \sum_i \langle n_i^2 \rangle + \sum_{i,j} \langle n_i n_j \rangle \tag{1.72}$$

In the above expression $< n_i n_j >$ can be related to the joint probability $dP(i,j)$ of finding the particles labeled by i and j in volume elements dV_i and dV_j respectively (see equation (1.52)).

$$\Longrightarrow \langle n_i n_j \rangle = \bar{n}^2 dV_i dV_j \left[1+\xi(\mathbf{r}_{ij})\right] \tag{1.73}$$

From equation (1.69), (1.71), (1.72) and equation (1.73)

$$\langle N^2\rangle = \bar{n}V + (\bar{n}V)^2 + \bar{n}^2 \int_V dV_i dV_j \xi(\mathbf{r}_{ij}) \tag{1.74}$$

The second moment μ_2 is given by

$$\begin{aligned}\mu_2 = \langle N^2\rangle - \langle N\rangle^2 &= \bar{n}V + \bar{n}^2 \int_V dV_i dV_j \xi(r_{ij}) \\ &= \mu_1 + \bar{n}^2 \int_V dV_i dV_j \xi_{ij} \end{aligned} \tag{1.75}$$

From the above equation we note that the second moment μ_2 and the average two point correlation function $\bar{\xi}_2$ are related in the following way

$$\bar{\xi} = \frac{1}{V^2} \int_V dV_i dV_j \xi(\mathbf{r}_{ij}) = \frac{1}{\mu_1^2}(\mu_2 - \mu_1) \tag{1.76}$$

In the same way we can relate the average three and four point correlation functions $\bar{\zeta}$ and $\bar{\eta}$ to the third and fourth moments μ_3 and μ_4 respectively.

$$\bar{\zeta} = \frac{1}{\mu_1^3}(\mu_3 - 3\mu_2 + 2\mu_1) \tag{1.77}$$

and

$$\bar{\eta} = \frac{1}{\mu_1^4}(\mu_4 - 6\mu_3 - 3\mu_2^2 + 11\mu_2 - 6\mu_1) \tag{1.78}$$

It has been found that in the hierarchical gravitational clustering the N-point average correlation functions $\bar{\xi}_N$ are related to the average two point correlation function $\bar{\xi}$ in the following way

$$\bar{\xi}_N = S_N \bar{\xi}^{N-1} \tag{1.79}$$

In practice estimates of moments are restricted to first few moments and one does not compute the full hierarchy.

1.5 Nonlinear gravitational clustering

The linear perturbation theory can be used for following the growth of density perturbations when $|\delta| \ll 1$. Galaxies and other large scale structures in the universe represent large fluctuations, i.e.,

$\delta \gg 1$; these have to be studied in an appropriate framework. In the present section we discuss some of the important approximations and semianalytic techniques which have been useful in modeling nonlinear gravitational clustering. In particular, we will discuss two approximations: the Zeldovich approximation and the adhesion approximation as these are most relevant for our studies. We also give a short overview of the spherical collapse model and the Press-Schechter formalism.

1.5.1 The Zeldovich Approximation

In order to model nonlinear gravitational clustering of matter, we work in the fluid limit and study dynamics in the Eulerian or Lagrangian framework. In the Eulerian system, physical properties like, density, etc., at fixed spatial positions are evolved using fluid equations. However, in the Lagrangian system, in place of evolving physical quantities at a fixed location, their values along the trajectories of fluid elements are evolved. Zeldovich (1970) proposed that linear perturbation theory for displacements in Lagrangian system can be used in the mildly-nonlinear regime for density contrast.

In the Zeldovich approximation the trajectory of a particle labeled by Lagrangian coordinate q is perturbed in the following way:

$$\mathbf{x}(\mathbf{q},t) = \mathbf{q} + b(t)\mathbf{p}(\mathbf{q}) \tag{1.80}$$

Where $\mathbf{p}(\mathbf{q})$ is the initial velocity and $b(t)$ is the linear growth factor. From the conservation of mass, initial density $\rho_0(q)$ and density $\rho(\mathbf{x},t)$ at time t are related as

$$\rho(\mathbf{x},t)d^3x = \rho_0(\mathbf{q})d^3q$$

or

$$\rho(\mathbf{x},t) = \frac{\rho_0(\mathbf{q})}{|\delta_{ij} - b(t)\mathcal{D}_{ij}(q)|} \tag{1.81}$$

Here $\mathcal{D}_{ij}(q) = -\partial_i p^j(q)$, is the deformation tensor. If we choose a coordinate system in which $\mathcal{D}_{ij}$ is diagonal and consider that the eigenvalues of $\mathcal{D}_{ij}$ are λ_1, λ_3 and λ_3 then

$$\rho(\mathbf{x},t) = \rho_0(\mathbf{q}) \prod_{i=1,2,3} [1 - b(t)\lambda_i(q)]^{-1} \tag{1.82}$$

In order to find an expression for $\mathbf{p}(\mathbf{q})$ we consider the small perturbation limit of equation (1.81)

$$\rho(\mathbf{x},t) \approx \rho_0(\mathbf{q})\left[1 + b(t)\nabla_q \mathbf{p}(\mathbf{q})\right] = \rho_0(\mathbf{q})\left[1 + b(t)\nabla_q \mathbf{p}(\mathbf{q})\right] \tag{1.83}$$

From the above equation density contrast is given by

$$\delta(\mathbf{x},t) = -b(t)\nabla_q \mathbf{p}(\mathbf{q}) \tag{1.84}$$

If we consider the initial velocity field $\mathbf{p}(\mathbf{q})$ irrotational i.e., $\mathbf{p}(\mathbf{q}) = \nabla_q \phi_0(\mathbf{q})$ then

$$\delta(\mathbf{x},t) = -b(t)\nabla_q^2 \phi_0(\mathbf{q}) \tag{1.85}$$

Comparing this equation with Poisson equation we get

$$\phi_0 = \frac{1}{4\pi G \rho_b a^2 b}\phi = \frac{a}{b}\psi \tag{1.86}$$

and so

$$\mathbf{p}(\mathbf{q}) = -\nabla\phi_0 = -\frac{a}{b}\nabla\psi \tag{1.87}$$

where ψ is given by equation (1.50). This is an interesting result because it shows that in the Zeldovich approximation the velocity $\mathbf{p}$ is proportional to $\nabla\phi(q)$. This approximation is used to set up initial condition in cosmological N-body simulations.

In the Zeldovich approximation, gravitational collapse of a three dimensional overdense region firstly occurs along the axis corresponding to the largest λ and leads to formation of a two dimensional sheet like structure of high density (finite two dimensional density) called a pancake. Since in the Zeldovich approximation velocity and acceleration are always parallel to each other, it fails to describe the motion of particles after their trajectories intersect each other. In order to rectify this problem and improve the validity of the Zeldovich approximation many suggestions have been proposed. One of these is known as the adhesion approximation (Kofman & Shandarin, 1988; Gurbatov et al., 1989; Weinberg & Gunn, 1990; Shandarin & Zeldovich, 1989; Matarrese et al., 1992; Brainerd et al., 1993; Bagla & Padmanabhan, 1994).

1.5.2 Adhesion approximation

Zeldovich approximation fails to take into account the change in gravitational potential when particles approach each other, or to change the direction of motion after shell crossing. As a result the thickness of the pancake keeps growing. In order to solve this problem, it has been suggested that particles can be confined to overdense regions by introducing an artificial viscosity term in the equation of motion (Kofman & Shandarin, 1988; Gurbatov et al., 1989; Weinberg & Gunn, 1990; Shandarin & Zeldovich, 1989). This approximation can be motivated from the Zeldovich approximation in the following way.

From equation (1.80) the peculiar velocity in Zeldovich approximation is

$$\mathbf{u} = a\dot{\mathbf{x}}(t) = a\dot{b}\mathbf{p}(\mathbf{q})$$

In terms of a new variable $\tilde{\mathbf{u}} = \mathbf{u}/a\dot{b}$, the above equation can be written as

$$\tilde{\mathbf{u}} = \mathbf{p}(\mathbf{q}) \tag{1.88}$$

as $\mathbf{p}(\mathbf{q})$ does not change with time so we can write

$$\frac{d\tilde{\mathbf{u}}}{db} = \frac{\partial\tilde{\mathbf{u}}}{db} + (\tilde{\mathbf{u}}.\nabla)\tilde{\mathbf{u}} = 0 \tag{1.89}$$

in the Adhesion approximation we replace RHS by a viscous term

$$\frac{\partial\tilde{\mathbf{u}}}{db} + (\tilde{\mathbf{u}}.\nabla)\tilde{\mathbf{u}}) = \nu\nabla^2\tilde{\mathbf{u}} \tag{1.90}$$

In the limit when ν is very small contribution to the RHS comes mainly from the regions where $\nabla^2\tilde{\mathbf{u}}$ is large i.e., caustics.

In order to solve equation (1.90) we need to supplement it by the continuity equation, which can be written in terms of a variable $\eta = a^2\rho$, in the following way

$$\frac{\partial\eta}{db} + \frac{\partial}{\partial x_i}(\eta\tilde{u}_i) = 0 \tag{1.91}$$

Equation (1.90) is called the Burger equation and can be solved analytically in one dimension in the following form

$$U(x,b) = \left(\frac{1}{4\pi\nu b}\right)^{1/2} \int_{-\infty}^{\infty} \exp\left[-\frac{\psi(q)}{2\nu} - \frac{(x-q)^2}{4\nu b}\right] dq$$

where $\tilde{u} = -\nabla\psi$ and $\tilde{u} = -2\nu\nabla lnU$.

1.5.3 Spherical collapse

The spherical collapse model is one of the examples in which an analytical prescription for finding the growth of perturbations in the nonlinear regime exists. In this case a spherical overdense region is modeled as a closed FRW universe ($k = 1$) in an otherwise uniform background which is modeled as a flat FRW universe ($k = 0$). The densities of the overdense region and background are evolved using Friedmann equations. In place of using Friedmann models, in what follows we will solve this problem using Newtonian mechanics which also gives the same results.

If we consider that the total mass within a shell region is M (which does not change during collapse) and the radius at time t is $R(t)$ then

$$\ddot{R}(t) = -\frac{GM}{R^2(t)} \tag{1.92}$$

and so

$$\frac{\dot{R}^2(t)}{2} = \frac{GM}{R} + E \tag{1.93}$$

Here E is an integration constant which can be identified with the total energy of the shell. If we consider that the energy of the system is negative, as is required for formation of a bound system, then the above equation can be solved with the following parametric solution

$$R(\theta) = \frac{GM}{2E}(1-\cos\theta) = A(1-\cos\theta) = \frac{R_{max}}{2}(1-\cos\theta) \tag{1.94}$$

$$t(\theta) = \frac{GM}{(2E)^{3/2}}(\theta-\sin\theta) = B(\theta-\sin\theta) = \frac{t_{max}}{\pi}(\theta-\sin\theta) \tag{1.95}$$

where $A^2 = 2EB^2, R_{max} = 2A, t_{max} = B\pi$.

Equation (1.94) shows that due to gravitational attraction, the expansion rate of the overdense regions slows down in comparison to the background. After reaching a maximum size R_{max} (called the turn-around radius) at time t_{max}, the overdense region stops expanding and begins to collapse

At turnaround:

$$E = \frac{GM}{R_{max}} \Longrightarrow R_{max} = \frac{GM}{E} = 2A \tag{1.96}$$

We expect the overdense region virializes before collapsing to $r = 0$. At virialization:

$$E = \frac{U}{2} = \frac{GM}{2R_{vir}} \Longrightarrow R_{vir} = \frac{GM}{2E} = \frac{R_{max}}{2} \tag{1.97}$$

From equation (1.94) we can write an expression for the density of the overdense region in the following way

$$\rho(t) = \frac{3M}{4\pi R^3(t)} = \frac{3M}{4\pi A^3(1-\cos\theta)^3} \tag{1.98}$$

If we model the expansion of background by the Einstein-de Sitter model then the background density $\rho_b(t)$ evolves as

$$\rho_b(t) = \frac{1}{6\pi G t^2} \tag{1.99}$$

From equation (1.98) and equation (1.99) we can write an expression for the nonlinear density contrast

$$1+\delta(t) = \frac{\rho(t)}{\rho_b(t)} = \frac{9}{2}\left(\frac{GMB^2}{A^3}\right)\frac{[\theta(t)-\sin\theta(t)]^2}{[1-\cos\theta(t)]^3}$$

Using the fact that $A^2 = 2EB^2$, and $E = GM/2A$, we get

$$1+\delta = \frac{9}{2}\frac{(\theta-\sin\theta)^2}{(1-\cos\theta)^3} \tag{1.100}$$

In order to compare the nonlinear and linear density contrast we expand the above equation around $\theta = 0$

$$1+\delta = \frac{9}{2}\frac{(\theta-\sin\theta)^2}{(1-\cos\theta)^3} = \frac{9}{2}\frac{\left[\theta-\left(\theta-\frac{\theta^3}{6}+\frac{\theta^5}{120}-..\right)\right]^2}{\left[1-\left(1-\frac{\theta^2}{2}+\frac{\theta^4}{24}\right)\right]^3} \approx 1+\frac{3}{20}\theta^2 \tag{1.101}$$

and so

$$\delta_l(\theta) = \frac{3}{20}\theta^2 \tag{1.102}$$

and in the linear limit

$$\theta(t) \approx \left(\frac{6\pi t}{t_{max}}\right)^{1/3}; \text{ and } R(t) \approx \frac{R_{max}}{4}\theta^2$$

and so

$$\delta_l(t) = \left(\frac{6\pi t}{t_{tmax}}\right)^{2/3} \text{ or } \delta_l(t) \propto a(t) \tag{1.103}$$

Note that this is exactly the same result as is given by linear perturbation theory (equation (1.46)). From equation (1.103) and (1.100) we can easily compute the linear and nonlinear density contrast respectively at the turn-around i.e., $\theta = \pi, t = t_{max}$

$$\delta_{turn} = \begin{cases} \frac{3(6\pi)^{2/3}}{20} \approx 1.06; & \text{for linear} \\ \frac{9\pi^2}{16} - 1 \approx 4.6; & \text{for nonlinear} \end{cases} \tag{1.104}$$

If we consider that the nonlinear density contrasts at the turn-around and virialization are δ_{turn} and δ_{vir} respectively and use the fact that $\rho \propto 1/R^3$, and $\rho_b \propto 1/t^2$, then

$$\frac{\delta_{vir}}{\delta_{turn}} = \frac{\rho_{vir}/\rho_b^{vir}}{\rho_{turn}/\rho_b^{turn}} = \left(\frac{R_{max}}{R_{vir}}\right)^3\left(\frac{t_{vir}}{t_{max}}\right)^2 \tag{1.105}$$

and so at the virialization i.e., $t_{vir} = 2t_{max}$, we get

$$\delta_{vir} = \begin{cases} \frac{3(12\pi)^{2/3}}{20} \approx 1.68; & \text{for linear} \\ 32\left[\frac{9\pi^2}{16}\right] - 1 \approx 176; & \text{for nonlinear} \end{cases} \tag{1.106}$$

1.5.4 The Press-Schechter formalism

The Press-Schechter formalism (Press & Schechter, 1974) models aspects of nonlinear gravitational clustering semi-analytically. In the Press-Schechter formalism the fraction of mass $F(M)$ in the collapsed objects at any time t, which have mass greater than M, is identified with the fraction of the initial volume for which the density contrast is greater than a critical value i.e., $\delta > \delta_c$. Here the critical density contrast δ_c is identified with the linearly extrapolated density contrast at time t, needed for virialization in spherical collapse model i.e., $\delta_c = 1.68$, for Einstein-de Sitter model. The main results of the Press-Schechter formalism can be derived in the following way.

If we consider that the initial density field is Gaussian, and smooth it over a scale r, using a spherical-top hat window function $W(x,r)$, then the probability of finding a spherical region with density contrast in range $[\delta, \delta + d\delta]$ is given by

$$P(\delta, r) = \frac{1}{\sqrt{2\pi\sigma(r)}} \exp\left(-\frac{\delta^2}{2\sigma^2(r)}\right) \tag{1.107}$$

where

$$\sigma^2(r) = \int \frac{dk}{k} \frac{k^3 P(k)}{2\pi^2} 9 \left(\frac{\sin kr - kr\cos kr}{(kr)^3}\right)^2 \tag{1.108}$$

In the Press-Schechter formalism the fraction of mass $F(M)$ in the collapsed objects with mass greater than M is identified with the fraction of the initial volume for which $\delta > \delta_c$.

$$F(M) = \int_{\delta_c}^{\infty} P(\delta, r) d\delta = \int_{\delta_c}^{\infty} \frac{1}{\sqrt{2\pi\sigma(r)}} \exp\left(-\frac{\delta^2}{2\sigma^2(r)}\right) d\delta = \frac{1}{2}\text{Erfc}\left[\frac{\delta_c}{\sigma\sqrt{2}}\right] \tag{1.109}$$

Here Erfc(x) is the complimentary error function.

This formalism does not take into account the mass in the underdense regions, which also collapses eventually. It underestimates the mass function $F(M)$ by a factor of two which is corrected by multiplying equation (1.109) by two.

$$F(M) = \frac{2}{\sqrt{\pi}} \int_{\delta_c/\sigma\sqrt{2}}^{\infty} e^{-x^2} dx = \text{Erfc}\left[\frac{\delta_c}{\sigma\sqrt{2}}\right] = \text{Erfc}\left(\frac{\nu}{\sqrt{2}}\right) \tag{1.110}$$

where $\nu = \delta_c/\sigma$. On the basis of equation (1.110) we can also compute the fraction of mass $f(M)dM$, called the multiplicity function, in the objects which have mass in the range $[M, M+dM]$.

$$f(M)dM = \frac{\partial F(M)}{\partial M} = \sqrt{\frac{2}{\pi}} \left(\frac{\delta_c}{\sigma(M)}\right) \left(\frac{-1}{\sigma(M)} \frac{\partial \sigma(M)}{\partial M}\right) \exp\left(-\frac{\delta_c^2}{2\sigma^2(M)}\right) dM \tag{1.111}$$

or

$$f(M)dM = \sqrt{\frac{2}{\pi}} \left|\frac{dln\sigma}{dM}\right| \nu \exp(-\nu^2/2) dM \tag{1.112}$$

and the comoving number density of objects $N(M)dM$ in the mass range $[M, M+dM]$ is

$$N(M)dM = \frac{\rho_b}{M} \times f(M)dM = \sqrt{\frac{2}{\pi}} \frac{\rho_b}{M^2} \left|\frac{dln\sigma}{dlnM}\right| \nu \exp(-\nu^2/2) dM \tag{1.113}$$

For a power law model i.e., $P(k) \propto Ak^n$

$$\sigma^2(M) = \left(\frac{M}{M_{nl}}\right)^{-(n+3)/3} \implies \left|\frac{dln\sigma}{dlnM}\right| = \frac{(n+3)}{6} \tag{1.114}$$

and so

$$N(M)dM = \frac{1}{\sqrt{2\pi}} \frac{\rho_b}{M^2} \frac{(n+3)}{3} \left(\frac{M}{M_{nl}}\right)^{-\frac{(n+3)}{6}} \exp\left[-\frac{\delta_c^2}{2} \left(\frac{M}{M_{nl}}\right)^{-(n+3)/3}\right] dM \tag{1.115}$$

1.6 Cosmological N-body simulations

In the case when there are no analytic methods available for modeling nonlinear gravitational clustering, numerical methods or cosmological N-body simulations are the main tools (Efstathiou et al., 1985; Sellwood, 1987; Hockney & Estwood, 1988; Bagla & Padmanabhan, 1997a; Bertschinger, 1998; Aarseth, 2003; Bagla, 2005; Dolag et al., 2008). In cosmological N-body simulations the gravitating matter is considered in the form of discrete particles and the trajectories of particles are integrated in an expanding background. The gravitational force at small scales is softened in order to avoid collisions as each N-body particle represents a large number of particles in the universe. The value of the softening scale (ϵ) and type of softening is decided on the basis of the model under consideration and the level of accuracy needed. At every time step the gravitational force acting on particles is computed and the positions and velocities of particles are updated self consistently. In order to represent the physical problem faithfully a large number of particles are considered which makes force computation very expensive i.e., it grows as $O(N^2)$.

In oder to get around the problem of force computation many techniques have been developed in which the force is approximated, at all scales or at some scales, at the cost of computational speed. In one of these techniques called the Particle Mesh method (PM) an artificial mesh is constructed in the simulation volume and physical quantities are extrapolated back and forth at the grid or mesh points using some extrapolation function (Bouchet & Kandrup, 1985; Efstathiou et al., 1985; Bagla & Padmanabhan, 1997a). The force is computed in Fourier space using Fast Fourier Transformation (FFT) which makes it computationally inexpensive i.e., the computational cost of force calculation grows as $O(N \log N)$ in place of $O(N^2)$. In PM method, the force at small scales is not calculated accurately and for better accuracy either the force computation is done directly or the mesh is refined. One of the very useful feature of this method is that periodic boundary conditions are incorporated automatically which makes this method suitable for cosmological simulations.

In another popular method called the Tree method (Barnes & Hut, 1986; Barnes & Hut, 1989; Bouchet & Hernquist, 1988) particles in cosmological simulations are assumed to be distributed in the form of a tree like hierarchy of cells. The largest or the root cell contains all particles and the smallest cell contains just one particle. In order to compute the force acting on a particle, a bunch of particles in a cell of size D at a distance d is represented by a single particle at the center of the mass of the cell if $D/d < \theta$. Here θ is an arbitrary parameter which is optimized for the model being simulated. In this case also the cost of force calculation grows as $O(N \log N)$ in place of $O(N^2)$. This method is accurate at small scales but it is slow; a method has been proposed called the TreePM method in which the force computation at large scales is done using the particle mesh techniques (Bagla, 2002; Bagla & Ray, 2003).

Chapter 2

Role of substructure- I: Planar collapse

2.1 Introduction

The cold dark matter (CDM) models of structure formation in the universe have been quite successful in explaining the features of matter distribution in observations and cosmological N-body simulations. Structure formation in a cold dark matter dominated universe takes place hierarchically i.e., structures at small scales form first and merge together and/or accrete matter from their surrounding and lead to structure formation at larger scales (Blumenthal et al., 1984; Davis et al., 1985; White & Frenk, 1991; Padmanabhan, 1993; Bernardeau et al., 2002). In this situation it becomes an interesting issue to investigate the effects of small scale perturbations or substructure on larger scales. This is one of the core issues of this thesis. In the present and the next chapter we will present the results of our studies of mode coupling in gravitational clustering. Our main focus will be on the effects of small scale perturbations on collapse of perturbations at large scales in cosmological N-body simulations. The main results outlined in this chapter have been published in Bagla, Prasad & Ray (2005).

In order to model structure formation in the universe the dynamics of perturbations at various scales have to be understood. It has been found that as long as the amplitude of density perturbations at any scale is small ($\delta \ll 1$), its growth can be studied using linear perturbation theory. However, once it becomes large ($\delta \approx 1$) linear perturbation theory no longer remains valid since perturbations at different scales start to couple with each other (mode coupling) and the system becomes nonlinear. Several studies have concluded that at the level of the second moment of density contrast (power spectrum, two point correlation function etc.) there are significant effects of perturbations at large scales on small scales but not vice versa.

On the basis of a set of numerical experiments Little, Weinberg & Park (Little, Weinberg & Park, 1991) showed that the appearance of nonlinear structures mainly depends on the initial power over a narrow range of wavenumbers around the scale of nonlinearity. In their numerical experiments they truncate or replace power at small scales by a different realization of a Gaussian random field and observe the effects of truncation or replacement of power on nonlinear structures. They argued that since power at $k < k_{nl}$ (k_{nl} is scale of nonlinearity) is always small and the growth of power at $k > k_{nl}$ is mainly governed by nonlinear evolution, therefore the appearance of nonlinear structures at any epoch is mainly governed by the power at the scale which is becoming nonlinear at that epoch.

In order to understand the significance of perturbations at various scales in gravitational clustering, Klypin & Melott (Klypin & Melott, 1992) proposed a measure called the Kinetic energy Ratio (KR) which depends on the power in a narrow range of scales. They pointed out that the shape of nonlinear structures at any scale does not depend on the power at much smaller scales which have already collapsed, and the power at much larger scales which mainly provides coherent motions. On the basis of a set of cosmological N-body simulations for power law models ($n = 1, -1, -3$), they found that in a highly nonlinear regime KR has a tendency of approaching a constant value i.e., $n = -1$.

Bagla & Padmanabhan (Bagla & Padmanabhan, 1997a) showed that in nonlinear gravitational clustering the transfer of power is mostly from large to small scales. On the basis of a set of numerical experiments, in which they either suppress or enhance initial power at small scales, they showed that due to flow of power during nonlinear evolution, the index of power spectrum at small scales moves asymptotically towards $n = -1$. They showed that this result agrees with the earlier studies (Klypin & Melott, 1992) and remains valid even when extra power is added at small scales. They also showed that nonlinear evolution leads to transfer of power from small to large scales also by forming a k^4 tail in power spectrum. This is significant only if the initial power spectrum is steeper than k^4 which rarely happens (Peebles, 1974; Peebles, 1980; Zeldovich, 1965).

In order to understand the effects of small scale structures on the collapse of large scale perturbations, Evrard & Crone (Evrard & Crone, 1992) carried out a set of numerical experiments and found that the collapse of large scale perturbations is insensitive to the presence of structures at small scales. This result was contrary to the "previrilization" hypothesis of Peebles (Davis & Peebles, 1977; Peebles, 1990) which says that non-radial motion due to substructure can retard the gravitational collapse of large scale perturbations. Evrard & Crone argued that non-radial motions and delayed collapse in Peebles's finding came about due to external torques from the inhomogeneous surrounding, not from substructure within the test cluster itself. The priviralization hypothesis predicts that the critical density contrast for spherical collapse at least a factor of five larger than what is general considered.

In the violent-relaxation framework of Lynden-Bell (Lynden-Bell, 1967) the presence of substructure can lead coarse grain phase space density towards an equilibrium value without disturbing the fine grain phase space density i.e., mixing in phase space. Weinberg (Weinberg, 2001) also pointed out that substructure can play an important role in the evolution of a system of collisionless particles in phase space. The presence of substructure in the surroundings of a collapsing structure can lead to very strong non-radial motion inside it and can slow down its collapse (Peebles, 1990). Transverse motions can lead to a change in the density profiles of haloes (Peebles, 1990; Subramanian, 2000). Gravitational interaction between small clumps can bring in an effective collisionality even for a collisionless fluid (Ma & Bertschinger, 2004; Ma & Boylan-Kolchin, 2004). Thus it is important to understand the role played by substructure in gravitational collapse and relaxation in the context of an expanding background. In particular, we would like to know if this leaves an imprint on the non-linear evolution of the correlation function. The effect of substructure on collapse and relaxation of larger scales is another manifestation of mode coupling.

We study the interplay of clumping at small scales with the collapse and relaxation of perturbations at much large scales. In the present study we show that perturbations at small scales can affect collapse of large scale perturbations, particularly when these are highly symmetric. We model large scale perturbations in the form of a plane wave. We find that dynamical relaxation of the plane wave is faster in the presence of substructure. Scattering of substructures and the resulting enhancement of transverse motions of haloes in the multistream region leads to a thinner pancake. In turn, collapse of the plane wave leads to formation of more massive haloes as compared to the collapse of substructure in the absence of the plane wave. The formation of more massive haloes happens without any significant increase in the total mass in the collapsed haloes. In one of the numerical experiments in this study we use the Burger's equation to model the collapse and find that the preferred value of viscosity in the framework of the Adhesion model (Gurbatov et al., 1989) depends primarily on the number of streams in a region.

The plan of the chapter is as follows. In §2.2 we give the basic equations for the dynamics of gravitational clustering in an expanding universe. In section §2.3 we discuss some toy models which we simulated for our study. We discuss the results of our study in section §2.4 and give the main conclusions in section §2.5.

2.2 Gravitational clustering

2.2.1 Dynamics of gravitational clustering

In an expanding background the amplitude of density perturbations $\delta_{\mathbf{k}}$ can be evolved using the following nonlinear equation

$$\frac{d^2\delta_{\mathbf{k}}}{dt^2} + 2\frac{\dot{a}}{a}\frac{d\delta_{\mathbf{k}}}{dt} = \left(\frac{3H_0^2\Omega_m}{2}\right)\frac{\delta_{\mathbf{k}}}{a^3} + A_{\mathbf{k}} - B_{\mathbf{k}} \tag{2.1}$$

where $A_{\mathbf{k}}$ and $B_{\mathbf{k}}$ are given by equation (1.43) and (1.44) respectively.

As has been discussed earlier (see §1.3.2), the above equation is a non-linear second order partial differential equation which can be solved only in situations when either the nonlinear coupling terms $A_{\mathbf{k}}$ and $B_{\mathbf{k}}$ are zero or $A_{\mathbf{k}} - B_{\mathbf{k}} = 0$. It can be shown that the individual virialized objects that satisfy the condition $2T + U = 0$, where T and U are the kinetic and potential energy respectively, do not make any contribution towards the growth of perturbations through mode coupling (Peebles, 1974) at much larger scales, i.e. the leading contribution to $A_{\mathbf{k}} - B_{\mathbf{k}}$ vanishes as $|\mathbf{k}| \longrightarrow 0$. The contribution of mode coupling due to interaction of such objects is not known.

Approximate approaches to structure formation can be developed by ignoring the interaction of well-separated scales. The evolution of density perturbations can be modeled as a combination of non-linear collapse at small scales, and the collapsed objects can be displaced using quasi-linear approximations (Bond & Mayers, 1996; Monaco et al., 2002a; Taffoni, Monaco and Theuns, 2002). These approaches yield an acceptable description of properties of collapsed objects and their distribution for a first estimate. PINICCHIO (Monaco et al., 2002a; Taffoni, Monaco and Theuns, 2002) provides sufficient information about halo properties and merger trees for use with semi-analytic models of galaxy formation. The efficacy of these models puts an upper bound on the effects of mode coupling that we are studying here.

2.3 Numerical Experiments

In order to investigate the effects of small scale perturbations or substructure on perturbations at large scales we carried out a set of numerical experiments using cosmological N-body simulations. In these experiments we considered perturbations at two widely separated scales i.e., the large scales and the small scales, in an Einstein-de Sitter background. Since the local geometry of collapse at the time of initial shell crossing is planar in nature (Zeldovich, 1970), we modeled large scale perturbations in the form of a single plane wave. This allows us to study the interaction of well-separated scales without resorting to statistical estimators like the power spectrum and two point correlation function.

2.3.1 The initial power spectrum

For our numerical experiments we considered an initial power spectrum which has nonzero power only at two widely separated scales i.e., small scales and large scales. Perturbations at large scales (Δ_l) were considered in the form of a plane wave with $\mathbf{k} = \mathbf{k}_f$, where $\mathbf{k}_f$ is the fundamental wavenumber of the simulation box.

$$\Delta_l^2(k) = \begin{cases} A, & \text{for } \mathbf{k} = k_f \hat{z}; \\ 0, & \text{for all other } \mathbf{k} \end{cases}$$

Here $\Delta^2(k)$ is the power per logarithmic interval in k

Perturbations at small scales were considered to be constant across a narrow range of wavenumbers $k_0 \pm \delta k$ and zero outside of this window

$$\Delta_s^2(k) = \begin{cases} \alpha A, & \text{for } k_0 - \delta k < |\mathbf{k}| < k_0 + \delta k; \\ 0, & \text{for other values of } \mathbf{k} \end{cases}$$

For small scale perturbations we used a Gaussian random realization of the power spectrum Δ_s. We considered four values of α i.e., $0.5, 1.0, 2.0$ and 4.0 (see Table 2.1), and normalize the amplitude of large scale perturbations A such that shell crossing takes place at epoch $a = 1$.

2.3.2 Codes and models

We used a Particle-Mesh (PM) (Bagla & Padmanabhan, 1997a) code and a TreePM code (Bagla, 2002; Bagla & Ray, 2003) for our simulations. The TreePM code uses a spline softening with softening length equal to the length of a grid cell in order to ensure collisionless evolution. All the simulations were carried out with 128^3 particles (see Table 2.1). We considered two type of initial distributions of particles named *grid* and *perturbed grid*. In the *Grid* distribution case particles are located at the grid points before being displaced to set up the initial condition and in the *Perturbed grid* case particles are randomly displaced from the grid points (Bagla & Padmanabhan, 1997a); this displacement has a maximum amplitude of 0.05 grid lengths. Such an initial condition is needed to prevent particles from reaching the same position in the plane wave collapse case as such a situation is pathological for Tree codes. We checked that these small displacements do not affect the initial conditions to be realized by comparing the results of the simulation PM_00L and T_00L (see Table 2.1 for detail).

The simulations T_10P and T_40P are identical to the simulations T_10L and T_40L except that the small-scale fluctuations are restricted to the direction orthogonal to the direction of the plane wave. These simulations are useful for differentiating between competing explanations for the results outlined below.

We expect that bound substructure can be torn apart due to interaction with rapidly in-falling matter. On the other hand, a higher average density in the multistream region can lead to rapid

Name	Method	α	Plane wave	IC
PM_00L	PM	0.0	Yes	Grid
T_00L	TreePM	0.0	Yes	Perturbed grid
T_05L	TreePM	0.5	Yes	Grid
T_10L	TreePM	1.0	Yes	Grid
T_20L	TreePM	2.0	Yes	Grid
T_40L	TreePM	4.0	Yes	Grid
T_10P	TreePM	1.0	Yes	Perturbed grid
T_40P	TreePM	4.0	Yes	Perturbed grid
T_05	TreePM	0.5	No	Grid
T_10	TreePM	1.0	No	Grid
T_20	TreePM	2.0	No	Grid
T_40	TreePM	4.0	No	Grid

Table 2.1: This table lists parameters of N-Body simulations we have used. All the simulations used 128^3 particles. The first column lists name of the simulation, second column lists the code that was used for running the simulation, third column gives the relative amplitude of small scale power and the plane wave, the fourth column tells us whether the large scale plane wave was present in the simulation or not, and the last column lists the distribution of particles before these are displaced using a realization of the power spectrum. *Grid* distribution means that particles started from grid points. *Perturbed grid* refers to a distribution where particles are randomly displaced from the grid points, this displacement has a maximum amplitude of 0.05 grid points.

growth of perturbations. It is well known that pancakes are unstable to fragmentation due to growth of perturbations (Valinia et al., 1997). The velocity field is anisotropic due to infall along one direction. Hence the rate at which perturbations grow will also exhibit anisotropies. Velocity dispersion along the direction of plane wave collapse is larger than the transverse direction, hence the growth of fluctuations in the transverse plane is expected to be more rapid.

If the in-falling material contains collapsed substructure, then gravitational interaction between these can induce large transverse velocities. This takes away kinetic energy from the direction of infall, which in turn can lead to a more fragmented and thiner multistream region.

2.4 Results

Gravitational collapse of the plane wave occurs along the z-direction and a two dimensional sheet like structure or the pancake forms which contains multistream regions i.e., particles with different velocities at the same spatial positions. In Figure 2.1 we show the positions and velocities of particles along the z-direction for PM_00L model. This figures shows that the number of streams increase when we approach towards the center of the pancake.

In order to check that the results of our simulations are independent from the code being used, in Figure 2.2 we show the density profiles for simulations PM_00L (solid line) and T_00L (dashed line) in the left and right panels at two epochs $a = 1$ and $a = 2$ respectively. This figure shows that the curves for the model PM_00L and T_00L closely follow one another as the density profiles are almost identical when we use different codes. The small difference can be attributed to the different initial conditions. We checked this assertion by running PM_00L model with the perturbed grid initial conditions. The TreePM method has a slightly better resolution but it does not induce any new features. This is expected as the force softening length used in the TreePM simulations is one grid length, the same as the interparticle separation, and it has been shown that such force softening does not induce two-body collisions (Melott et al., 1997; Splinter et al., 1998). Apart from the pure plane wave case we simulated all other models with the TreePM code.

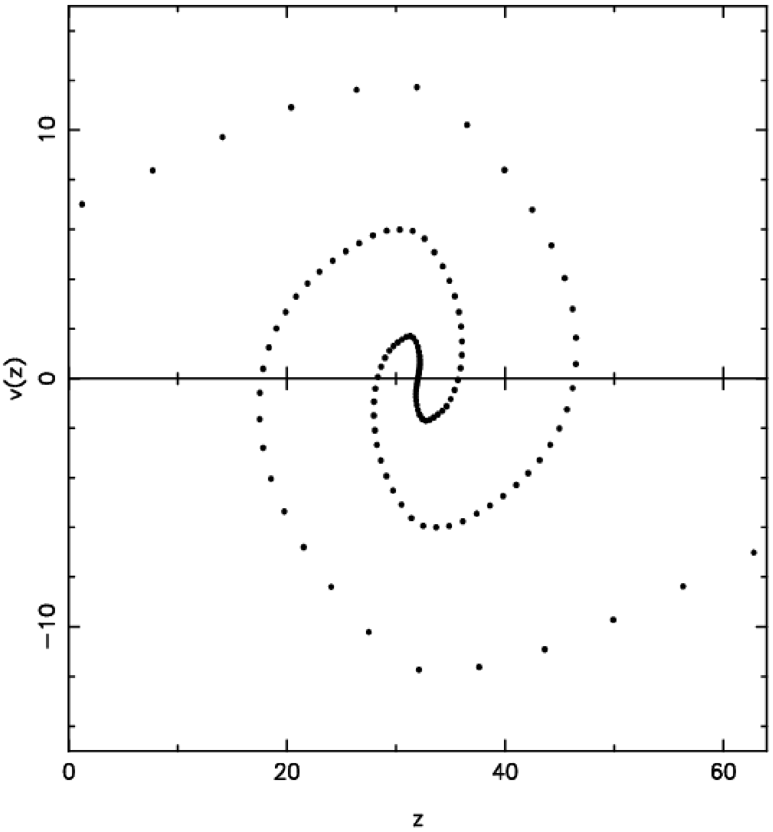

Figure 2.1: This figure shows velocities and positions of particles along the z-axis in the simulation of plane wave collapse i.e., model PM_00L. Collapse of the plane wave leads to formation of multistream regions where particles with different velocities can occupy the same spatial position. The number of streams in multistream regions increases when we approach towards the center of the collapse.

2.4.1 Thickness of the pancake

We study the effects of substructure on the thickness of the pancake which forms when the plane wave collapses. If the substructure does not play an important role in the evolution of large scale perturbations then the thickness of the pancake should be independent of the presence of substructure. On the other hand, if the substructure does indeed speed up the process of dynamical relaxation then we should see some signature in terms of the thickness of the pancake, velocity structure, or both. Any such effect will be apparent only at late times as infall of matter into the pancake dominates at early times.

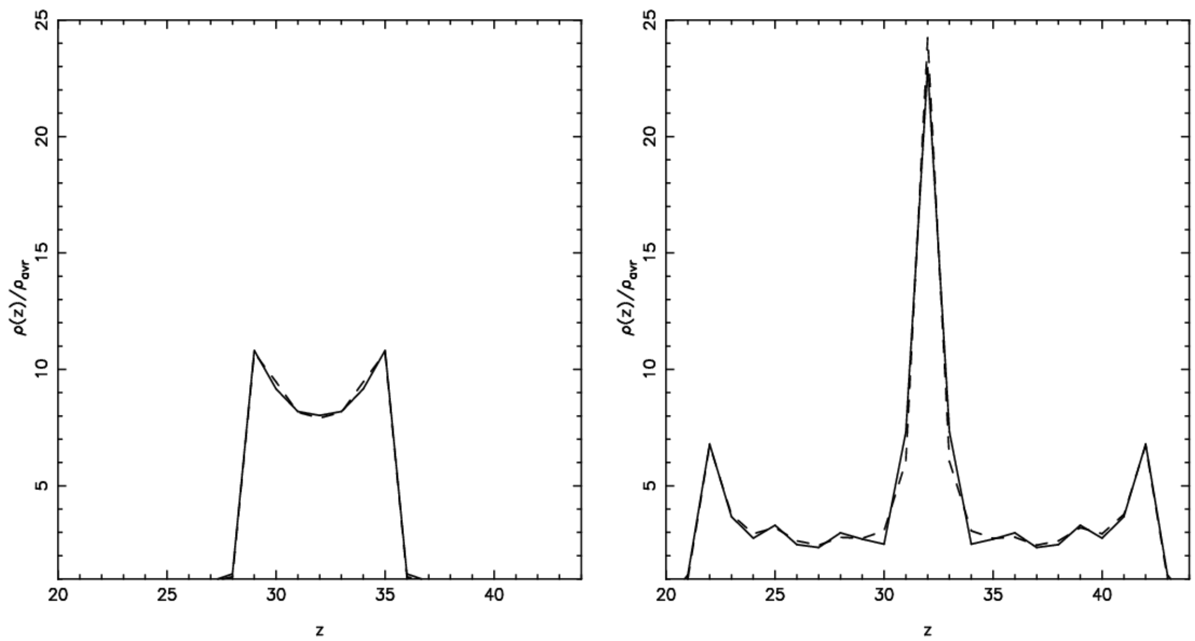

Figure 2.2: The left and right panels in this figure show the average density $\rho(z)$ as a function of z-coordinate for model PM_00L (solid-line) and T_00L (dashed-line) at two epochs $a = 1$ and $a = 2$ respectively. From this figure we can see that the density profile does not change much when we use different codes.

In Figure 2.3 we show the slices parallel to x-z plane at $a = 2$ for simulations T_00L, T_10L and T_40L. In this figure the amount of substructure increases from the left panel to the right and the plane wave collapses along the vertical direction (z-axis). The boundary of the multistream region is clearly visible in all the slices even though this region is fragmented in the last panel. From these slices it is clearly visible that the pancake is thinner when there is more substructure.

We show a detailed comparison with a different level of substructure in Figure 2.4. In the left panel of Figure 2.4 we show the averaged overdensity as a function of z-coordinate at $a = 2$ for models T_05L (dashed line), T_10L (dot-dashed line), T_20L (dotted line) and T_40L (dot-dot-dashed line). We compute average overdensity by averaging over all x and y coordinates for a given interval $(z \pm \Delta z)$. This figure shows that the peak density at the center of the pancake is smaller when there is more substructure. Apart from this, we also observe that the mass enclosed within a given distance from the center of the pancake (defined here as the trough of the potential well of the plane wave) is smaller for more substructure, even though the variation is very small at less than 10 per cent between

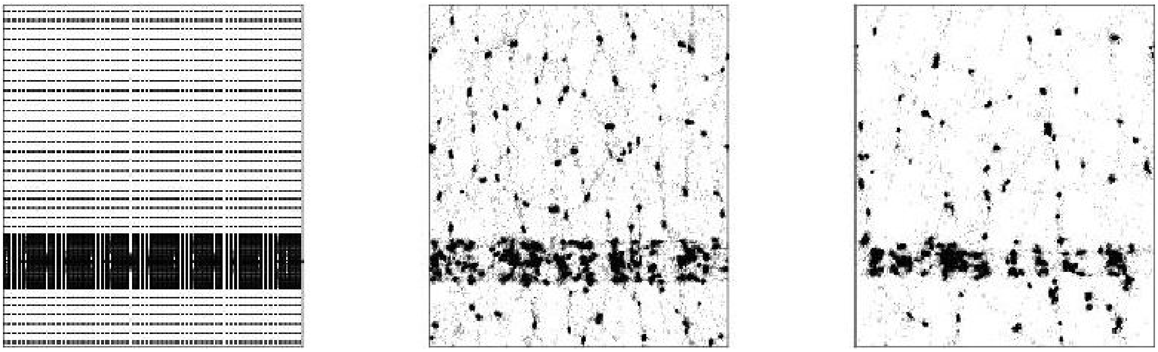

Figure 2.3: The left, middle and right panels in this figure show the slices parallel to the x-z plane at $a = 2$ for simulation T_00L, T_10L and T_40L respectively. Collapse of the plane wave along the vertical direction (z-axis) leads to formation of the pancake. From this figure we can see that the thickness of the pancake decreases when we increase the amount of substructure (when we go from left to right).

the extreme cases (see Figure 2.9).

In the middle and right panels of Figure 2.4 we show the rms transverse velocities of particles and haloes as a function of the z-coordinate for the same models and epoch as in the left panel. From the middle panel it is clear that the transverse motions are enhanced in the dense pancake region. The amplitude of transverse motions is larger in simulations with more substructure. The size of the region where these motions are significant varies with the amount of substructure as in the case of overdensity (left panel). The rms transverse velocities do not go zero outside the pancake region, instead these level off to a small residual value.

The transverse motions are due to motions of particles in clumps that constitute substructure, due to infall of particles in these clumps, and transverse motions of clumps as they move toward each other. In order to see these effects more clearly, we plot the rms velocities for haloes in the right panel of Figure 2.4. We have identified haloes with the friends-of-friends (FOF) algorithm using a linking length of $l = 0.2$ grid length and have considered only those haloes for our analysis which have at least 50 particles. Such a high cutoff for halo members is acceptable because typical haloes have several hundred members. For simulations with a small amount of substructure, the motion of clumps is subdominant and hence the transverse motions are contributed mostly by internal motion and infall. In simulations with more substructure, motions of clumps contribute significantly to the

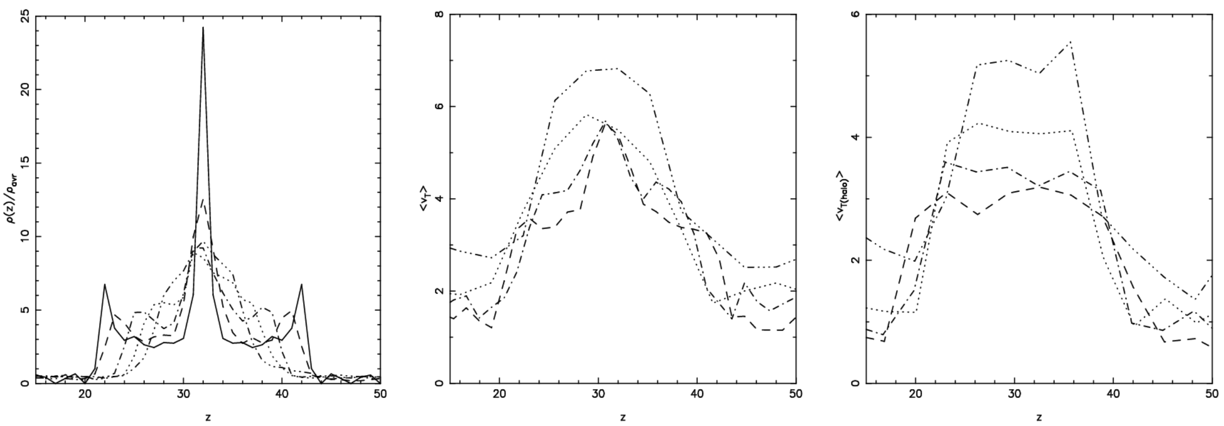

Figure 2.4: The left panel in this figure shows the average overdensity as a function of z-coordinate at $a = 2$ for models T_05L (dashed line), T_10L (dot-dashed line), T_20L (dotted line) and T_40L (dot-dot-dashed line). The middle and the right panels show the rms transverse velocities of particles and haloes for the same models at the same epoch as in the left panel.

rms transverse velocity. Gravitational attraction of clumps, particularly in close encounters in the pancake region, induces the transverse component. Collisions are enhanced in the pancake regions as the number density of clumps is higher.

In order to convince ourselves that transverse motions induced by scattering/collision of clumps are the most likely reason for the reduced thickness of pancakes, we compare simulations T_10L and T_40L with T_10P and T_40P. In simulations T_10P and T_40P, the small-scale fluctuations do not have any z-dependence or they are anisotropic. In this case, in place of clumps in the in-falling matter there are streams of particles so the scattering is suppressed in comparison to the case when there are clumps i.e., when small scale perturbations are isotropic. Most collisions take place head-on and grazing collisions are rare. Of course, in the simulation the presence of the plane wave leads to breaking of these streams into clumps as the streams are stretched inhomogeneously in the z-direction. These clumps are aligned parallel to the z-axis. In the pancake region scattering of these streams occasionally leads to complex patterns. If the presence of substructure and its growth in the pancake was the only cause for making the pancake thinner then the pancake in these simulations should be thinner as well. In Figure 2.5 we show slices from simulations T_40L and T_40P for $a = 2$. A slice from the simulation PM_00L is also plotted here for reference. The visual comparison shows

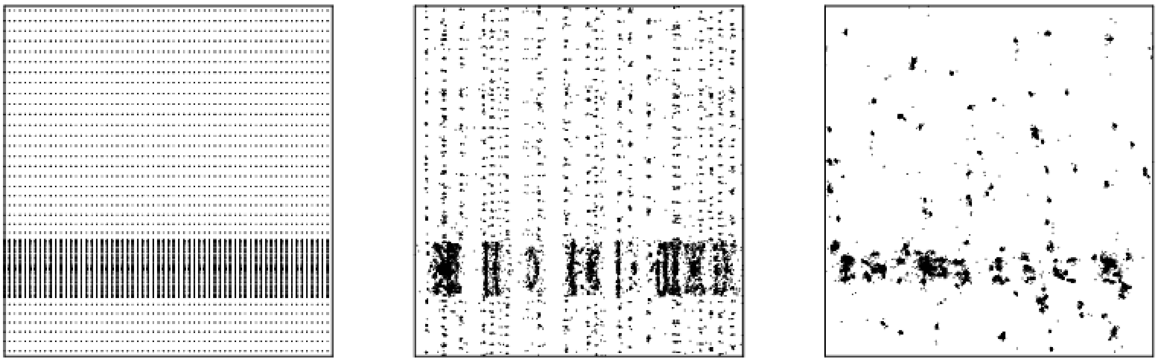

Figure 2.5: The left, middle and right panels in this figure show the slices parallel to the x-z plane at $a = 2$ for simulations PM_00L, T_40P and T_40L respectively. This visual comparison shows that the pancake is thinner in T_40L as compared to T_40P. Indeed, the thickness of pancake in T_40P and PM_00L is very similar.

that the pancake is thinner in simulation T_40L in comparison to simulation PM_00L and T_40P. This reinforces the point that scattering of clumps in the pancake region is the key reason for a thinner pancake.

Figure 2.6 shows the slices parallel to the x-z plane for models T_05L and T_05 at three epochs, $a = 0.5, 1.0$ and 2.0. Identical slices for models T_205L and T_20 are shown in Figure 2.7. These figures bring out the effect of the plane wave on the collapse of perturbations at small scales as well as the influence of small-scale fluctuations on the thickness of the pancake formed by the collapse of the plane wave.

2.4.2 Pancake and viscosity

In the present study we also use the Adhesion approximation (see §1.5.2) to model substructure in the form of some artificial viscosity. In this case the equation of motion for particles is given by the Burger equation (Gurbatov et al., 1989; Weinberg & Gunn, 1990; Shandarin & Zeldovich, 1989) which can be solved analytically. For one dimensional motion this equation can be written as

$$\frac{\partial u}{\partial b} + u\frac{\partial u}{\partial x} = \nu\frac{\partial^2 u}{\partial x^2}. \qquad (2.2)$$

Here $u = \partial x/\partial b$ is the velocity and b is the linear growth factor. This equation can be solved

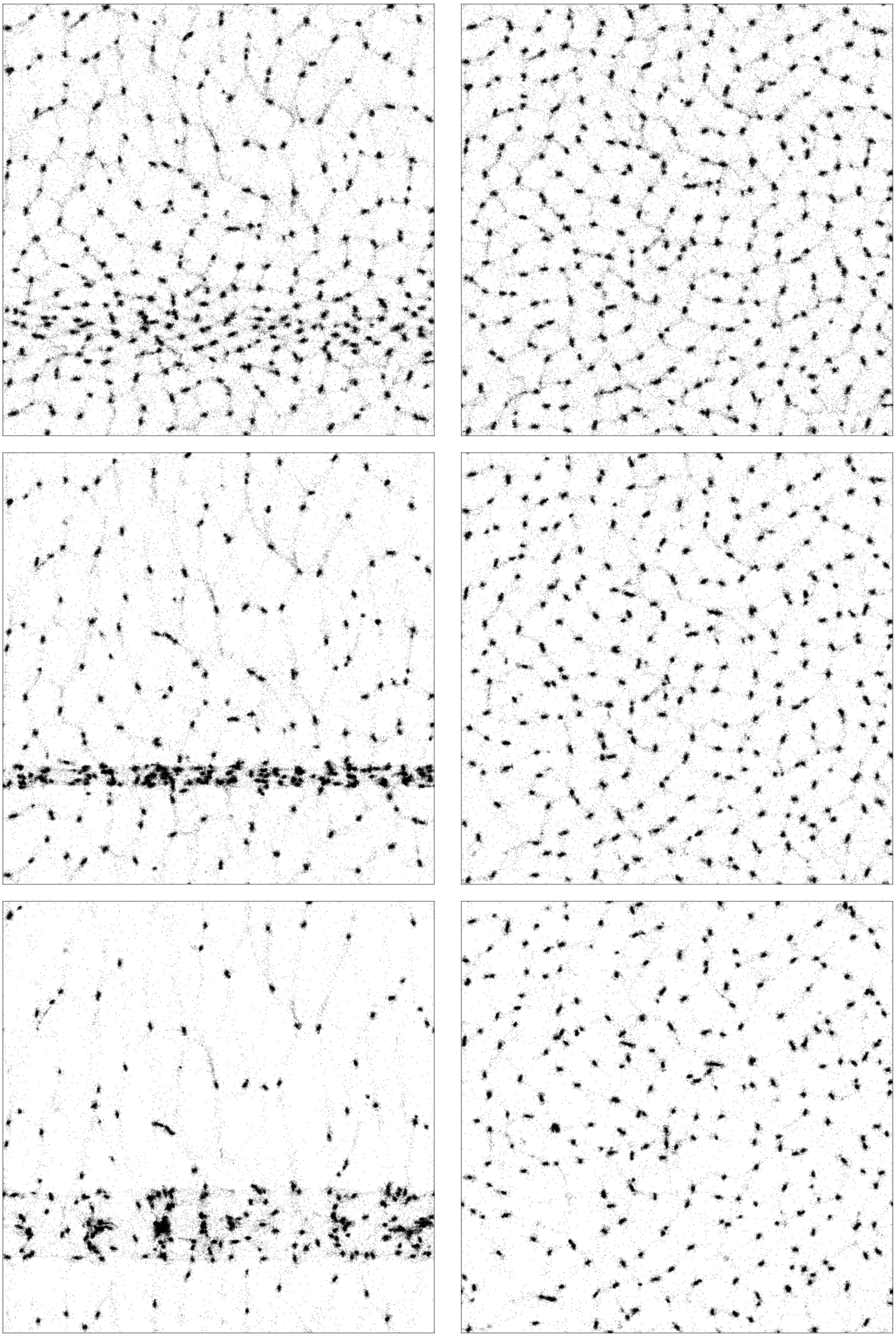

Figure 2.6: The first and second column in this figure show the slices parallel to the x-z plane for models T_05L and T_05 at $a = 0.5$ (first row), $a = 1.0$ (second row) and $a = 2.0$ (third row) respectively.

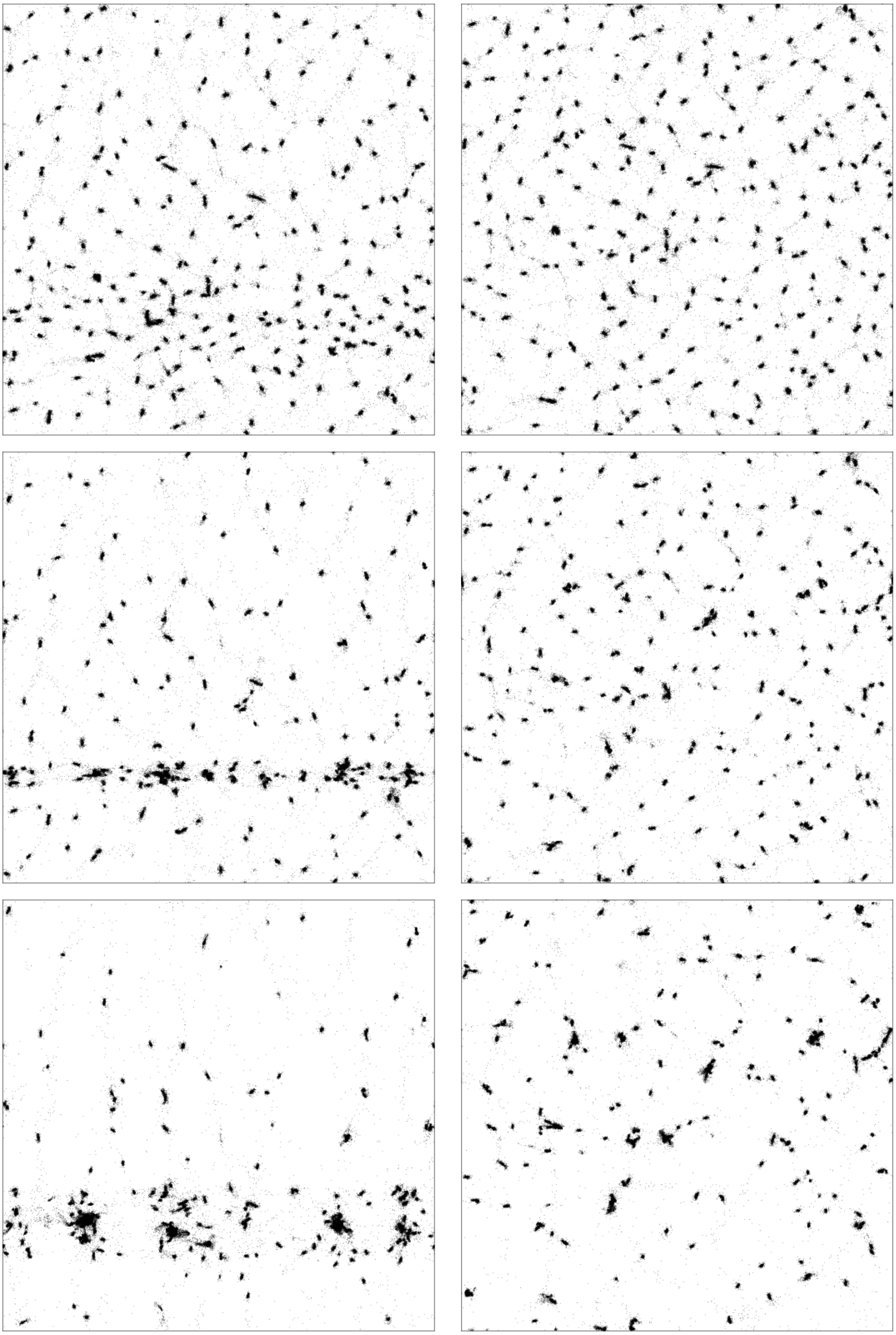

Figure 2.7: The first and second column in this figure show the slices parallel to the x-z plane for models T_20L and T_20 at $a = 0.5$ (first row), $a = 1.0$ (second row) and $a = 2.0$ (third row) respectively.

analytically by introducing a velocity potential $u = \partial\psi/\partial x$, where ψ coincides with the gravitational potential at the initial time. The solution has the following form.

$$u = \nabla\psi = -2\nu\nabla\ln U \tag{2.3}$$

and,

$$U(x,b) = \left(\frac{1}{4\pi\nu b}\right)^{1/2} \int_{-\infty}^{\infty} \exp\left[-\frac{\psi(q)}{2\nu} - \frac{(x-q)^2}{4\nu b}\right] dq. \tag{2.4}$$

Here q and x are the Lagrangian and Eulerian coordinates respectively. In this method we integrate the differential equation for particle trajectories. At each time step velocity is calculated by the above procedure at grid points and interpolated to particle positions.

We have found in previous section that when the level of substructure increases the pancake becomes thin since the substructure helps in the relaxation of the plane wave. This motivates us to represent the effects of substructure in the form of an artificial viscosity which also helps to keep the pancake thin.

We study the collapse of the plane wave in the framework of the Adhesion approximation (Gurbatov et al., 1989) and quantify the effect of substructure and viscosity in terms of the mass $M(z)$ enclosed within a distance z from the center of pancake.

$$M(z) = \int_{z_c}^{z_c+z} dz' \rho(z' + z_c) \tag{2.5}$$

Here $\rho(z)$ is the density at position z and z_c is the center of the pancake. There is no ambiguity for comparing the results with N-body simulations in case of no substructure as the density depends only on z. While comparing other simulations with the adhesion solution, we consider the density averaged over the x- and y-directions. The adhesion model is run only for the one-dimensional problem.

The solid lines in the left, middle and right panels in Figure 2.8 show the enclosed mass $M(z)$ for PM_00L model at $a = 2, 3$ and 4 respectively. From this figure we notice that the slope of the curve changes suddenly when the number of streams change i.e., when we move away from the center of the collapse. In all the panels the dashed, dotted and dot-dashed lines show the mass enclosed in the case of the adhesion model for $\nu = 400, 600$ and 900 respectively.

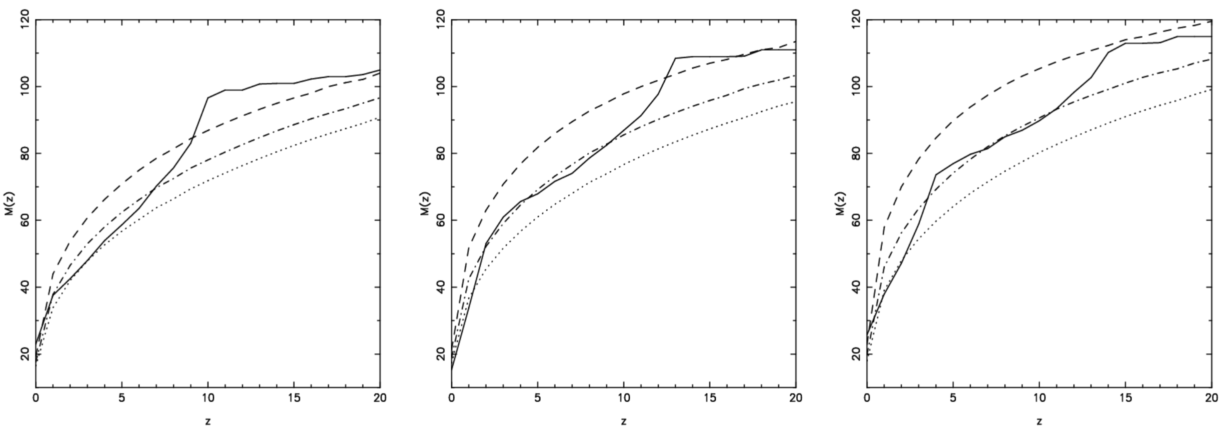

Figure 2.8: This figure shows the mass $M(z)$ enclosed within a distance z from the center of the collapse for PM_00L at three epochs $a = 2$ (left panel), $a = 3$ (middle panel) and $a = 4$ (right panel). The curves for the Adhesion approximation with viscosity $\nu = 400, 600$ and 900 are also shown by the dashed, dotted and dot-dashed lines. This figure shows that the value of viscosity changes when the number of streams are changed.

We compare the models with various level of substructure with one-dimensional adhesion model in Figure 2.9. We plot the mass enclosed $M(z)$ for models PM_00L, T_10L, T_40L and adhesion model with $\nu = 600$ at $a = 2, 3$ and 4 in the left, middle and the right panel respectively. Addition of substructure clearly changes the character of the problem and the collapse no longer remains one dimensional. However, the scale of the substructure is so small compared to the wavelength of the plane wave that the large scale collapse is still very close to planar. Here the motivation behind the comparison of models with various level of substructure with one-dimensional adhesion model is to see the effect of substructure on the favored value of effective viscosity. Substructure removes the sharp change in density at the boundaries of 3-stream, 5-stream and 7-stream regions and the curves for T_10L and T_40L are smoother in the pancake region. The finite viscosity curve matches simulations with substructure over a wider range of scales than with PM_00L. There are no other noteworthy differences.

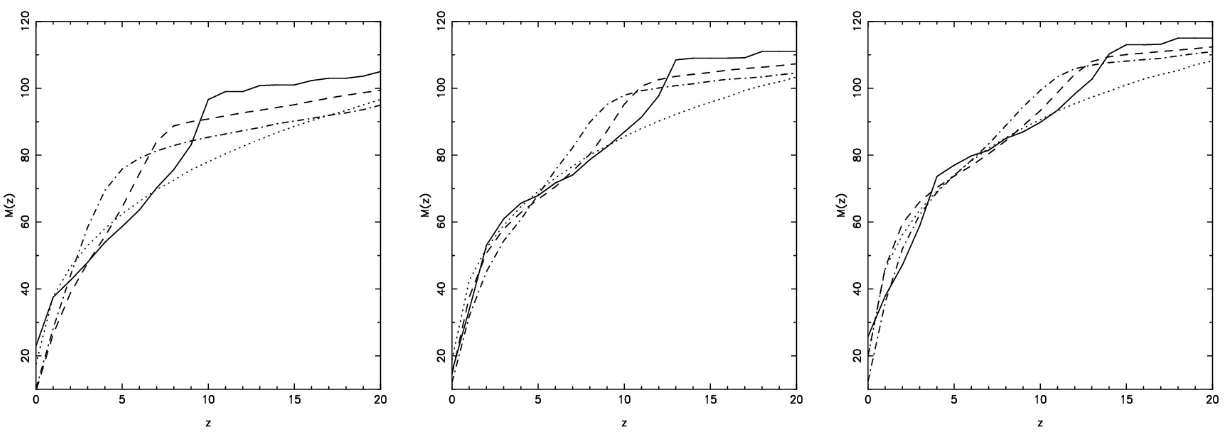

Figure 2.9: This figure shows the mass $M(z)$ enclosed within a distance z from the center of the multistream region for PM_00L (solid line), T_10L (dashed line), T_40L (dot-dashed line) and one-dimensional adhesion model with $\nu = 600$ at $a = 2$ (left panel), $a = 3$ (middle panel) and at $a = 5$ (right panel).

2.4.3 Mass function

The total mass in collapsed objects or mass function $F(M)$ is one of the important measures in gravitational clustering of matter. In Figure 2.10 we compare the mass function $F(M)$ for models with various level of substructure in the presence (thick lines) and absence (thin lines) of the plane wave. The curves for $\alpha = 0.5, 1.0, 2.0$ and 4.0 are represented by the solid, dashed, dotted and dot-dashed lines respectively. We use the FOF algorithm with linking length 0.2 for identifying the haloes and do not consider haloes with less than 50 particles for our analysis. The formation of collapsed objects mainly happens due to initial density fluctuations at small scales, with some modulation by the collapse of the plane wave.

We have observed that the plane wave pulls most of the matter toward the center of potential well (pancake) and a relatively small fraction of matter remains under-dense regions. The growth of small scale perturbations is greatly enhanced in the pancake region and suppressed in under-dense regions (see Figure 2.6 and Figure 2.7). At late epochs merging of haloes lead to more massive clumps. In under-dense regions smaller clumps have mass around the scale corresponding to the collapse of small scale perturbations. The two mass scales are clearly visible in Figure 2.10.

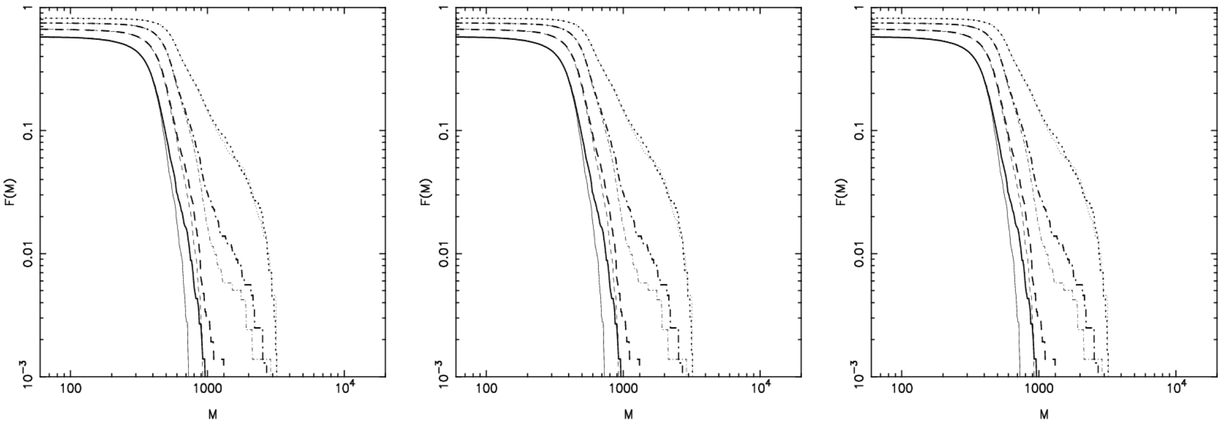

Figure 2.10: This figure shows the mass function $F(M)$ at three epochs $a = 0.5$ (left panel), $a = 1.0$ (middle panel) and $a = 1.0$ (right panel) for model with various levels of substructure i.e., $\alpha = 0.5$ (solid line), $\alpha = 1.0$ (dashed line), $\alpha = 2.0$ (dotted line) and $\alpha = 4.0$ (dot-dashed line). The models with and without the plane wave are represented by thick and thin lines respectively. This figure shows that in the presence of the plane wave the number density of massive haloes increases. However, the total mass in the collapsed objects remains almost the same.

2.5 Conclusions

In the present study we have addressed the issue of mode coupling in nonlinear gravitational clustering. In particular, we focused our attention on the effects of small scale perturbations or substructure on large scales. We tried to understand the effects of substructure on the collapse of large scale perturbations in cosmological N-body simulations. For our models we considered perturbations at two widely separated scales and have considered the large scale perturbations in the form of a plane wave. The simple form of the large scale perturbations allows us to use simple measures of clustering like the thickness of the pancake and the mass enclosed within a given distance for our analysis in place of statistical measures like correlation functions and moments of counts. Apart from the effects of substructure on the collapse of the plane wave, we also tried to understand the role of substructure in the framework of the Adhesion approximation.

The main conclusions of our present study are as follows:

- The thickness of the pancake which forms due to collapse of the plane wave is smaller when there is more substructure.

- The collisions between clumps lead to enhancement of the transverse velocities of particles and haloes.
- We have found that the thickness of the pancake is not small in the models in which collisions in substructure are suppressed by considering anisotropic small scale perturbations.
- We conclude that the collisions induce enhancement of transverse motions which takes away momentum from the direction of infall and leads to thinner pancakes.
- The presence of large scale perturbations or plane wave shifts the mass function towards larger masses. However, there is no significant change in the total mass in the collapsed haloes.
- In the adhesion model we found that for a given mass $M(z)$ enclosed within a given distance z we can find a single value of viscosity ν for a multistream region with given number of streams.

In the present study we found that there are significant effects of small scale perturbations on large scales i.e., substructure helps in the relaxation of the large scale perturbations when it is highly symmetric. In the next chapter we will discuss the effects of small scale perturbations on the collapse of large scale perturbations for generic models.

Chapter 3

Role of substructure- II: Hierarchical Models

3.1 Introduction

In Chapter 2 we showed that there are significant effects of perturbations at small scales or substructure on the collapse of perturbations at large scales when they are symmetric. We found that the thickness of the pancake which forms due to collapse of a plane wave is small when there is substructure in comparison with the case when substructure is absent. We concluded that in the presence of substructure, scattering of haloes in falling towards the pancake i.e., center of the potential well, transfers momentum along transverse directions and it leads to a thinner pancake.

In the present chapter we study the interplay of clumping at small scales with the collapse of perturbations at larger scales using cosmological N-body simulations. We quantify the effects of collapsed haloes on perturbations at larger scales using two point correlation function, moments of counts in cells and mass function. The purpose of this study is two fold and the primary aim is to quantify the role played by collapsed low mass haloes in the evolution of perturbations at large scales, this is in view of the visible effect we discussed in Chapter 2 when the large scale perturbations are highly symmetric. Another reason for this study is to ask whether features or a cutoff in the initial power spectrum can be detected using measures of clustering at scales that are already nonlinear. The final aim of this study is to understand the effects of ignoring perturbations at scales smaller than the resolution of cosmological N-body simulation.

It is well known that in nonlinear gravitational clustering in an expanding universe, perturbations at small scales do not influence collapse of large scale perturbations in a significant manner (Peebles, 1974; Little, Weinberg & Park, 1991; Bagla & Padmanabhan, 1997b; Couchman & Peebles, 1998) as far as the correlation function or power spectrum at large scales are concerned. This has led to a belief that ignoring perturbations at scales much smaller than the scales of interest does not affect results of cosmological N-body simulations. In one of our studies we found that if large scale collapse is highly symmetric then presence of perturbations at much smaller scales affect evolution of density perturbations at large scales (Bagla, Prasad & Ray, 2005).

The effect of substructure on the growth of perturbations at large scales depends on the significance of mode coupling between different scales. Key results about the mode coupling are as follows:

- If the initial conditions are modified by filtering out perturbations at small scales then mode coupling generates power at small scales. If the scale of filtration is smaller than the scale of nonlinearity at the final epoch then the nonlinear power spectrum as well as the appearance of large scale structure is similar to the original case (Peebles, 1985; Little, Weinberg & Park, 1991; Bagla & Padmanabhan, 1997b; Couchman & Peebles, 1998).

- Nonlinear evolution *drives* every model towards a weak attractor ($P(k) \approx k^{-1}$) in the mildly nonlinear regime ($1 \leq \bar{\xi} \leq 200$) (Klypin & Melott, 1992; Bagla & Padmanabhan, 1997b).

- In absence of initial perturbations at large scales, mode coupling generates power with ($P(k) \approx k^4$) that grows very rapidly at early times (Bagla & Padmanabhan, 1997b). There are a number of explanations for this feature, ranging from second order perturbation theory to momentum and mass conserving motion of a group of particles. The k^4 tail can also be derived from the full nonlinear equation for density (Peebles, 1974; Zeldovich, 1965).

- If we consider large scale perturbations to be highly symmetric i.e., planar, then small scale fluctuations play a very important role in the realaxation of nonlinear perturbations at large scales (Bagla, Prasad & Ray, 2005).

While the effect of large scales on small scales is known to be significant, particularly if the larger scales are comparable to the scale of nonlinearity, the effects of small scales on larger scales is known to be small in most situations, Even though this effect has not been studied in detail, many tools have been developed that exploit the presumed smallness of the influence of small scales on large scales (Bond & Mayers, 1996; Monaco et al., 2002a; Monaco et al., 2002b).

Gravitational clustering in N-body simulations start with a “quasi-uniform” distribution of particles and has perturbations at all scales starting from the mass scale of particles. It has been argued that such a system never reaches equilibrium. However, as the system evolves, larger and larger scales become nonlinear and the system shows scaling behaviour. This scaling behaviour is manifested only for a restricted class of initial conditions in an Einstein-de Sitter universe (Baertschiger et al., 2007a; Baertschiger et al., 2007b; Baertschiger et al., 2007c). Therefore it becomes an important issue to understand the effects of “pre-initial conditions” in nonlinear gravitational clustering. In general, pre-initial conditions are defined by the distribution of particles on which the initial density and velocity perturbations are imprinted. The pre-initial conditions are expected to have no density perturbations or symmetry, but it can be shown that at least one of these requirements must be relaxed in practice. This can lead to growth of some modes in a manner different from that expected in the cosmological perturbation theory. The present work allows us to understand the effects that may arise if the primordial power spectrum deviates strongly from a power law at small scales.

In order to understand the role played by substructure in the collapse of perturbations at large scales, in this chapter we study the evolution of three models in cosmological N-body simulations. The plan of this chapter is as follows. In §3.2 we discuss our models and various parameters we used. In §3.3 we present the results of our study and and in §3.4 we discuss these. In §3.5 we summarize our main results.

3.2 The models

In Chapter 2 we considered perturbation at large scales in the form of a plane wave in N-body simulations. In the present study we consider a more general form of the the initial power spectrum. We consider a power law spectrum with index -1 for our reference model (Model I). Apart from the reference model or Model I, we also consider two other models Model II and Model III in which we suppress and add power at small scales respectively. Some of the details of our cosmological simulations are as follows.

- All the cosmological simulations were carried out with the TreePM code (Bagla, 2002; Bagla & Ray, 2003).
- We used 200^3 particles in a volume of 200^3 cubic cells for each simulation.
- In order to avoid collisions we softened gravitational force at the scale of 0.5 grid length.
- For the reference model (Model I), we considered power spectrum $P(k) = AK^{-1}$ where A is normalized such that $\sigma^2(r = 12 \text{ grid lengths}, a = 1) = 1$.
- We studied these models in the Einstein-de Sitter universe
- Model II: In this model power at small scales is truncated using a Gaussian cutoff.
  $P(k) \;=\; A\,k^{-1}\;\exp\left[-k^2/k_c^2\right]$.
  We chose $k_c = k_{nyq}/4$, so that truncation is mainly at scales that are smaller than the scale of non-linearity at late times. A is chosen to be the same as for Model I.
- Model III: We add a Gaussian spike in this model.
  $P(k) \;=\; A\,k^{-1} + \alpha\,A\,k_c^{-1}\exp\left[-\left(k-k_c\right)^2/2\sigma_k^2\right]$.
  We chose same k_c as in Model II, $\sigma_k = 2\pi/L_{box}$ is same as the fundamental wave number and we took $\alpha = 4$. A is chosen to be the same as for Model I.

Clearly, the Model II and Model III have truncated and additional power respectively at small scales as compared to the reference model or Model I while the power at large scales is the same for all the three models. The left and right panels in Figure 3.1 show the linearly extrapolated power spectrum $\Delta^2(k)$ at the initial epoch in N-body simulations and the theoretical mass variance $\sigma^2(r)$ respectively for the three models being considered. From both the panels of Figure 3.1 we see that all the three models have identical power at the scales much larger than the scale at which we add or suppress the power i.e., $2\pi/k_c$.

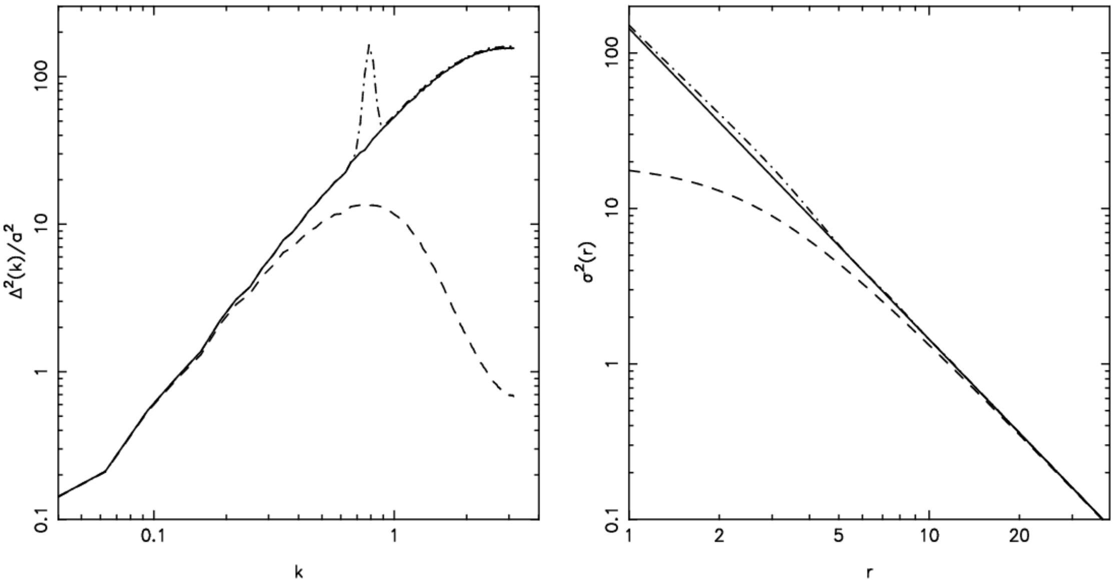

Figure 3.1: The left and right panels in this figure show the linearly extrapolated power spectrum $\Delta^2(k)$ and variance $\sigma^2(r)$ at the epoch $a = 1$. In both the panels models I, II and III are represented by the solid, dashed and dot-dashed lines respectively.

3.3 Results

In the present study our main goal is to understand the effects of variation in the initial power spectrum at small scales. For this we study the three models at two representative epochs: one where the scale of modification is linear, and the second epoch when the scale of nonlinearity is larger than the scales where the power spectra differ from each other. We refer to these epochs as an early epoch and a late epoch. The scale of nonlinearity in the reference model i.e., Model I at the early epoch is 4.8 grid lengths and the corresponding scale at the late epoch is 12 grid lengths. The wave number k_c corresponds to 8 grid lengths and become nonlinear at an intermediate epoch.

We compare the gravitational collapse of perturbations in the three models being considered visually and using the amplitude of clustering , Skewness and comoving number density of haloes. We expect that the features i.e., cutoff and peak, in the initial power spectrum will leave their signature in these statistical indicators at late epoch.

In Figure 3.2 we show the distribution of particles in a thin slice from simulations of the three models. The left column shows the distribution at an early epoch wheras the right column shows the same slice at late times. The top, middle and bottom row represent the Model II, I and III respectively. From this figure we see that the large scale distribution of particles is similar in all the three models for both epochs, although there are significant differences at small scales. Differences are more visible between Model II and other models, whereas the differences between Model I and Model III are less obvious. Also, differences between the models diminish as we go from the early epoch to the late epoch.

In Figure 3.3 we compare the clustering of matter in Model I, II and III in a more quantitative manner. In the first row of Figure 3.3 we plot the amplitude of clustering $\bar{\xi}(r)$ as a function of r for the three models at an early epoch (top-left frame) and at a late epoch (top-right frame). From these figures we see that the differences between the amplitude of clustering are more pronounced at the early epoch, though even here the differences are much smaller than those seen in Figure 3.1 where the linearly extrapolated $\sigma^2(r)$ has been plotted. At late times, models I and III have an indistinguishable $\bar{\xi}(r)$ whereas Model II has a slightly smaller amplitude of clustering at small scales when compared to other two models. It is also clear from this figure that at very large r compared to the scale of modification, all models have the same $\bar{\xi}$ even at the early epoch.

In the second row of Figure 3.3 Skewness S_3 as a function of scale r has been plotted for the three models at an early epoch (left column) and a later epoch (right column). From this we observe that at large scales, larger than the scale of modification (8 grid lengths), the three models agree well although there are significant differences at small scales, particularly at the early epoch. Model II has the highest Skewness, whereas Model III has the smallest Skewness at small scales: this is expected due to change in the local slope of σ^2 introduced by features in the initial power spectrum. This ranking does not change with time, though the differences between models decrease with further evolution of the system.

The bottom row in Figure 3.3 shows the number density of haloes $N(M)dM$ as a function of mass. Mass is in units of mass of each particle. Haloes were identified using the Friends-of-Friends algorithm (FOF) with a linking length of 0.1. We chose this linking length in order to avoid identifying smooth filaments in Model II as haloes. Haloes with a minimum of 20 particles were considered for

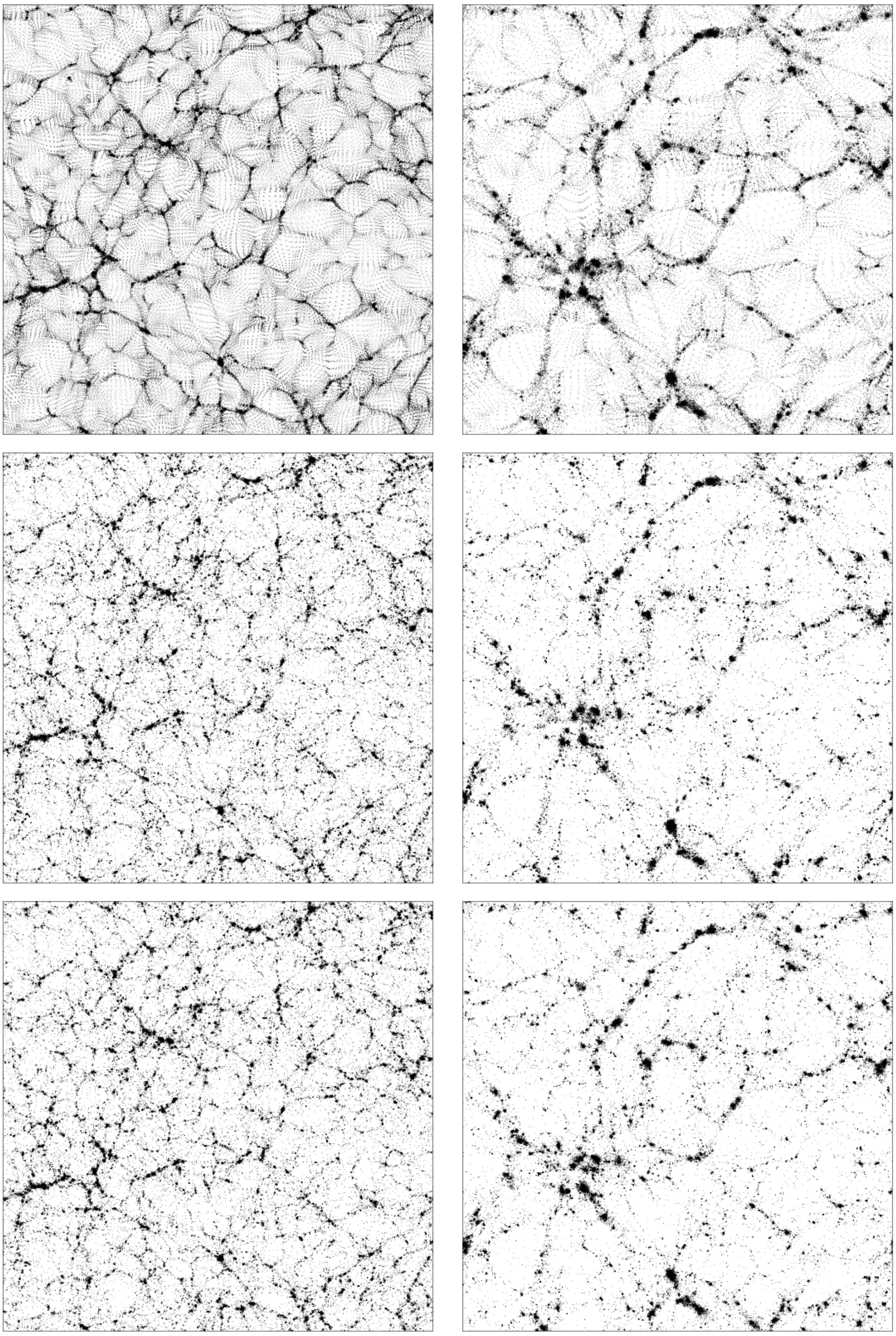

Figure 3.2: The first, second and third row in this figure show the slices for Model II, I and III respectively, at an early (first column) and a later epoch (second column). The early epoch is identified with an epoch when the scale at which we add or truncate power i.e., $2\pi/k_c$, is linear in the Model I and and the later epoch is identified with an epoch when the scale $2\pi/k_c$ is nonlinear in Model II.

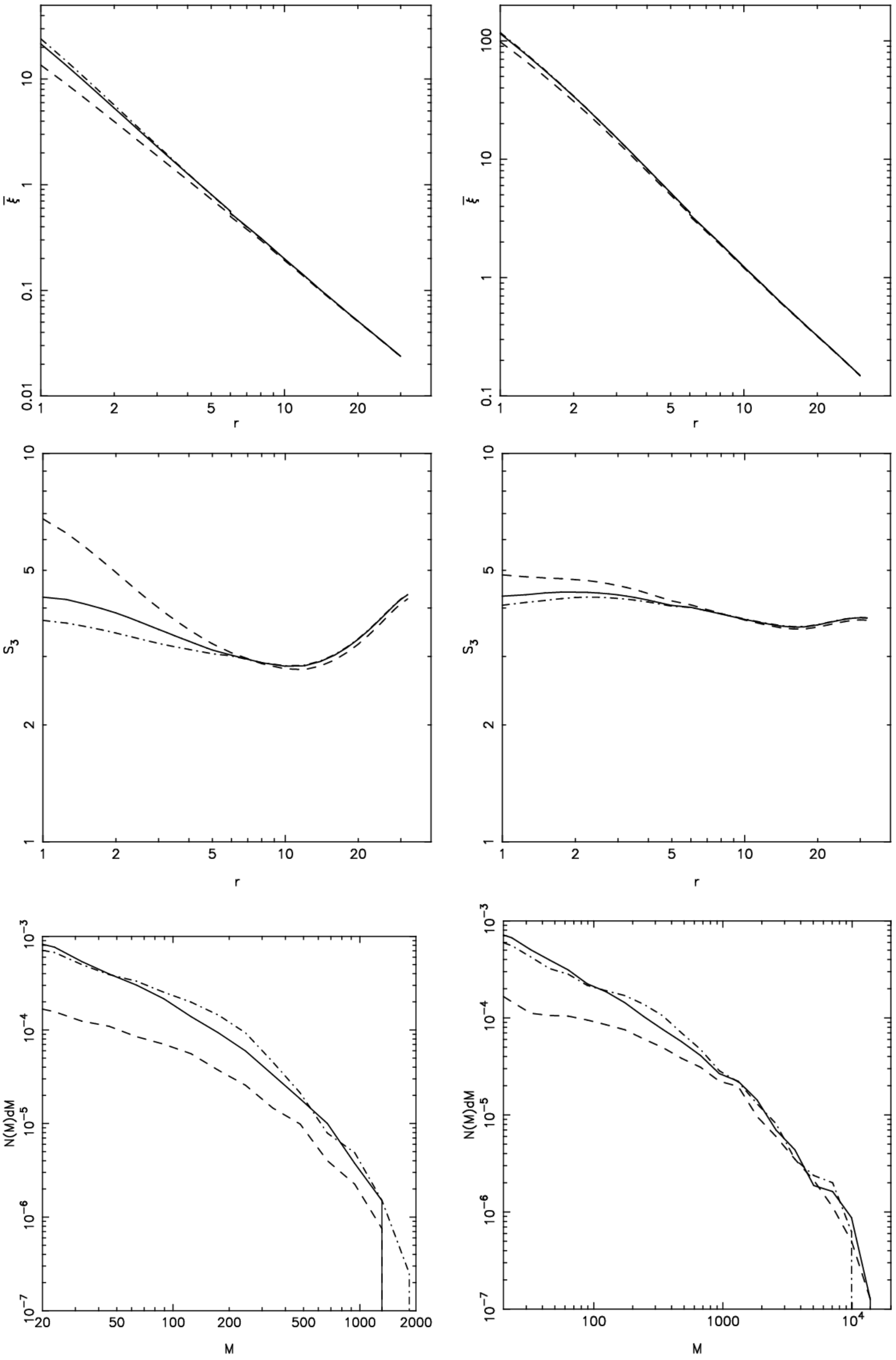

Figure 3.3: The first, second and third row in this figure show the average two point correlation function $\bar{\xi}$, Skewness S_3 and comoving number density of haloes $N(M)dM$ respectively, at an early (first column) and at a later epoch (second colum). Different models in all the panels are represented by the same line styles as in Figure 3.1.

this plot. We find that Model III has the largest number of haloes around the scale of modification, whereas Model II has the least number of haloes at this scale. Indeed, at the early epoch, Model II has a much smaller number of haloes at all mass scales when compared with Model I and Model III. At late times, Model II continues to have fewer small mass haloes though it almost matches the other two models at larger masses.

We find that the two point correlation function does not retain any information about differences in initial conditions after the scale where such differences are present becomes sufficiently nonlinear. This is in agreement with results of earlier studies (Peebles, 1985; Little, Weinberg & Park, 1991; Klypin & Melott, 1992; Bagla & Padmanabhan, 1997b; Couchman & Peebles, 1998).

Skewness S_3 is a slightly better indicator than the two point correlation function, in that it retains some information about the missing power at small scales in Model II even after the cutoff scale becomes nonlinear. It does not retain much information about the excess power that is added at small scales in Model III. One possible reason for this is that the cutoff affects the shape of the power spectrum at $k \ll k_c$ where the effects of adding extra power is more localized. We conclude that S_3 is able to retain information about the cutoff in the initial power spectrum if the cutoff scale is not strongly nonlinear. This may not have implications for observational signatures of a cutoff as observations of galaxy clustering are restricted to the redshift space and it has beens shown that redshift space distortions in the nonlinear regime erase differences between S_3 for different models (Bagla & Ray, 2006).

The number density of haloes in Model II at scales comparable to and smaller than the cutoff is smaller than that in Model I and III even after the cutoff scale becomes nonlinear. The mass function appears to be most sensitive indicator of a cutoff in the power spectrum in the mildly nonlinear regime.

3.4 Discussion

In the present study we have found that the memory of features in the initial conditions is erased in the quasi-linear regime. This erasure is almost complete in measures of the second moment like power spectrum and two point correlation function. This loss of information had been pointed out in earlier work also (Little, Weinberg & Park, 1991; Bagla & Padmanabhan, 1997b). The Skewness appears to be a better indicator of a cutoff in the initial power spectrum, at least in the quasi linear regime. We find that Skewness for Model II is distinctly higher for Model I or Model III, even when the scale of nonlinearity is much larger than the cutoff scale. Number densities of haloes is a very faithful indicator of the cutoff, even at late times. This is to be expected given that the number density of haloes can be predicted fairly accurately using the Press-Schechter mass function (Press & Schechter, 1974) that relies only on the initial power spectrum.

In order to interpret these results we would like to recall the key conclusions of our paper I in the present series (Bagla, Prasad & Ray, 2005) (see Chapter 2). In paper I, we studied the collapse of a plane wave with varying amount of collapsed haloes at much smaller scale (as compare to wavelength of the plane wave). We found that the thickness of pancake that forms due to the collapse of plane wave is smaller for models with larger amount of substructure. Our conclusion was that gravitational interaction of infalling clumps takes away some of the longitudinal momentum and leads to an increase of the transverse momentum. Thinner pancakes imply a higher density, and clumps are able to grow very rapidly in such environment. Our main motivation was to study collapse of plane wave as it is known from the Zeldovich approximation (Zeldovich, 1970) that locally, generic collapse is planar leading to formation of pancakes.

In case of generic initial conditions that we consider here, there is no fixed large scale that is collapsing as we have perturbations at all scales. However, we have ensured that perturbations at large scales are the same in all the three models. In this case the effect of power on large scales is to cause collapse around peaks of density, or equivalently empty the voids. The latter picture is more attractive as it also explains why collapse of perturbations at a scale leads to enhancement of power at smaller scales without any loss of power at the original scale: emptying under dense regions simply puts more and more matter in thin walls around the void that forms. We can say that power is transferred from the scale of perturbation, that is essentially the radius of voids that form, to the scale of thickness of pancake surrounding the void. As a given scale becomes nonlinear, we begin to see voids corresponding to this scale. Matter that collapsed at an earlier stage gets pushed into the pancake surrounding the void. The information about the shape of the initial power spectrum at scales smaller than the scale of nonlinearity is mostly restricted to the distribution of matter within pancakes. This explains the erasure of memory of initial conditions for the two point correlation function. The mass function and Skewness are more sensitive to the arrangement of matter within pancakes and hence these remain different for the model with a cutoff. Once the scale of cutoff becomes strongly nonlinear, most of the perturbations at this scale are expected to be part of highly over dense haloes. At this stage, we expect that all indicators of clustering will loose information about the details of the initial power spectrum at this stage.

In models I and III, there is significant amount of initial power at small scales. This leads to a fragmented appearance of pancakes and clearly pancakes cannot be thinner than the clumps. In Model II, there is no initial power at small scales. Power is generated at these scales by collapse of larger modes, power grows very rapidly at small scales and the nonlinear power spectrum in this case catches up with the power spectrum for the other two models.

Model III has significantly more power as compared with the reference model or Model I at small scales. This leads to a more rapid growth of perturbations at these scales, as is seen in the number density of collapsed haloes at the relevant scales at early times. At late times, these haloes are assimilated into bigger haloes and we rapidly loose any signature of the excess power. We expect the excess power to lead to thinner pancakes, motivated by conclusions of paper I. However, the scale of pancakes is such that this feature is not apparent.

3.5 Summary

In the present study we have shown that for a hierarchical model, there is little effect of features in the initial power spectrum on collapse of perturbations at large scales. We have also shown that the effects of features can be seen in several statistical indicators like Skewness and number density at the scales of features and also at smaller scales. The key conclusion which we can draw from the present study is that if we modify the power spectrum at small scales, there is no discernable effect of these modifications at larger scales. This can have implications in several situations:

- Cosmological N-Body simulations start with initial conditions that do not sample the power spectrum at large wave numbers i.e., scales smaller than the scale of resolution. In typical simulations of this type, a grid is used to generate initial conditions and only modes up to the Nyquist wave number are sampled. Indeed, if the number of particles is smaller than the number of grid cells used for generating initial conditions, the effective upper limit to wave numbers is even more restricted (Bagla & Padmanabhan, 1997a). The missing part of the power spectrum does not have any impact on the evolution of nonlinear structures at scales larger than the cutoff scale. We expect the effects of missing modes at large wave numbers to be less and less relevant as larger length scales (smaller wave numbers) become non-linear.

- It has been pointed out that the choice of pre-initial conditions, and the epoch at which the initial conditions are set up can lead to spurious growth of some modes (Baertschiger et al., 2007a; Baertschiger et al., 2007b; Baertschiger et al., 2007c). Clearly, these effects must be suppressed as the modes with spurious growth become nonlinear.

- Generation of perturbations in the early universe, and their evolution towards the end of the inflationary phase can lead to a scale dependent evolution of modes (Malquarti, Leach, & Liddle, 2004; di Marco et al., 2007). Our work clearly shows that such features will be impossible to detect if these are at scales that are strongly non-linear and difficult to detect if these are at scales that are mildly nonlinear. If scales where such variations occur are already nonlinear then these variations do no affect collapse of larger scales. Of course, if the scales where such variations occur are linear then these can be probed using galaxy clustering.

Chapter 4

Finite volume effects -I: Mass function

4.1 Introduction

Cosmological N-body simulations play an important role in modeling nonlinear gravitational clustering which leads to structure formation in the universe (for a brief introduction and references see §1.6). However, they have their limitations due to the finite number of particles, volume, mass and length resolutions. In cosmological N-body simulations matter is considered in the form of discrete particles which interact with each other by a smoothed gravitational force in an expanding background. The mass and length resolutions of cosmological N-body simulations depend on the number of particles used and the scale of force softening. In order to be realistic, the size of cosmological N-body simulations has to be large enough to be a representative sample of the real universe; a fact that allows us to use periodic boundary conditions.

In most cases the initial perturbations in cosmological N-body simulations are assumed to have a Gaussian distribution and are represented by their power spectrum which is sampled at discrete wavenumbers between the fundamental mode $k_f = 2\pi/L_{box}$, and the Nyquist wavenumber $k_{nyq} = \pi/L_{grid}$. This means that perturbations at scales smaller than two grid lengths and larger than the size of the simulation box are ignored. In nonlinear gravitational clustering, perturbations at large scales are expected to play an important role in the growth of perturbations at small scales and the limitation due to the size of the simulation volume can be crucial. In the present chapter we develop a formalism for understanding the limitations due to the finite box size in cosmological N-body simulation and use it to quantify corrections in the mass variance, two point correlation function, mass function and multiplicity function. We will also discuss applications of our formalism for some cosmological models. In the next chapter we will generalize our formalism and give analytical expressions for corrections in halo formation and destruction rate.

Colombi et. al (Colombi, Bouchet & Schaeffer, 1994) showed that the high density tail of the count probability distribution function (CPDF) is very sensitive to the size of the simulation box. As the higher order correlation functions and moments of counts in cells are sensitive to the tail of CPDF, they are significantly affected by the size of the simulation box. Moreover, the scaling relation i.e., $\xi_N \propto \xi^{N-1}$, no longer remains valid.

Gelb & Bertschinger (Gelb & Bertschinger, 1994a; Gelb & Bertschinger, 1994b) showed that the rms density fluctuations i.e., $\sigma(r)$, are suppressed at all scales when the size of the simulation box is reduced. They also showed that truncation of power spectrum at large scales due to the finite size of the simulation box affects nonlinear pair velocities at small scales. On the basis of high resolution two dimensional simulations,

Kauffmann and Melott (Kauffmann & Melott, 1992) found that the scaling relations (self similar evolution also) become more accurate when the index of power spectrum increases i.e., $n = 2$ model follows better scaling than $n = 0$. They argued that it is the absence of power at large scale due to the size of the simulation box which deforms the scaling relations. They also showed that void spectrum is affected by the size of the simulation box.

Bagla & Ray (Bagla & Ray, 2005) proposed that the convergence of cumulative mass function $F(M)$ can be used to estimate the effects of finite box size; the size of the simulation box can be considered large enough, if $F(M)$ does not change by a significant amount at the relevant scale when the size of the simulation box is increased. They found that there are significant effects of the size of the simulation box on mass function and two point correlation function i.e., these are underestimated when the size of the simulation box is reduced.

Power & Knebe (Power & Knebe, 2006) estimated the effects of the size of the simulation box on some integral properties of dark matter haloes i.e., concentration, spin parameter and triaxiality, and found that these properties significantly change for individual haloes but their statistical distribution remains unaffected.

In order to take into account the modes which are larger than the size of the simulation box an approach called the Mode Adding Procedure or MAP (Tormen & Bertschinger, 1996) has been proposed. In this approach firstly power at scales around the mode $k = 0$ is removed and then power at these scales is added after the simulation has been run by hand using Zeldovich approximation. This procedure works only when perturbations at the scales at which power is removed and added are linear and do not couple with perturbations at other scales. The main motivation behind the development of such a tool is to enhance the range of scales over which one can rely on cosmological simulations. Such an approach ignores the coupling of large-scale modes with small-scale modes and this again brings up the issue of what is a large enough scale for a given model such that the effects of mode coupling can be ignored.

In the present study we generalize the approach suggested by Bagla & Ray (2005) and propose a prescription for estimating corrections due to the size of the simulation box in cosmological N-body simulations. We give analytical expressions for corrections in linearly evolved mass variance, two point correlation function, mass function and multiplicity function. We apply our formalism to a few cosmological models. We find that correction in mass function is maximum near the scale of nonlinearity. As a corollary we also show that the correction to the number density of haloes of a given mass changes sign at this scale; the number density of low mass haloes is overestimated, whereas the number density of more massive haloes is underestimated. We conclude that the overestimation of density of low mass haloes is due to the lack of mergers that lead to formation of more massive haloes. We show that the corrections are typically small if the scale of nonlinearity is much smaller than the size of the simulation box. However, there are some cases in which the relative correction is significant even though a simulation volume much larger than the scale of nonlinearity is used. The main results of the present study have bee published in Bagla & Prasad (2006).

In §4.2 we give basic equations and describe our formalism to estimate corrections in physical quantities due to the size of the simulation box in cosmological N-body simulations. In particular, we give explicit expressions for corrections in rms density fluctuations (mass variance) σ and average two point correlations. The main results of the present study are given in §4.3 in the form of analytic expressions for corrections in the Press-Schechter mass function and multiplicity function. We compare some of results with cosmological N-body simulations in §4.4 and summarize the main results.

4.2 The formalism

The initial cosmological density perturbations are assumed to be Gaussian, which can be completely characterized by their power spectrum. In cosmological N-body simulations the initial power spectrum is sampled at discrete points in k space in the interval $k_f \leq k \leq k_{nyq}$. Here $k_f = 2\pi/L_{box}$, and $k_{nyq} = \pi/L_{grid}$, are the fundamental and Nyquist wavenumbers respectively. Modes larger than the size of simulation box i.e., $k < k_f$, are ignored and it is expected that they will not affect the evolution of modes which have been sampled. In what follows we will show that this is not the case and present a method for estimating the effects of modes $k < k_f$ on various physical quantities.

4.2.1 Clustering amplitude

We consider variance $\sigma^2(r)$ defined by equation (1.61) as the reference quantity and compute the correction in it due to the finite size of the simulation box. We use these to compute corrections in other physical quantities like the mass function and multiplicity function. Note that in place of $\sigma^2(r)$ any other second moment of density contrast can be considered but there is one advantage with $\sigma^2(r)$ that it is always positive.

In an ideal case i.e., when the size of the simulation box is taken to be infinity we get

$$\sigma^2(r) = \int_0^\infty \frac{dk}{k}\Delta^2(k)W^2(k,r) \quad \text{where} \quad \Delta^2(k) = \frac{k^3 P(k)}{2\pi^2} \tag{4.1}$$

Here we take $W^2(k,r)$ to be the spherical top-hat window function given by equation (1.59).

Since in cosmological N-body simulations $k_f \leq k \leq k_{nyq}$, in place of equation (4.1) we get

$$\sigma^2(r, L_{box}) = \int_{k_f}^{k_{nyq}} \frac{dk}{k}\Delta^2(k)W^2(k,r) \approx \int_{k_f}^{\infty} \frac{dk}{k}\Delta^2(k)W^2(k,r) = \sigma_0^2(r) - \sigma_1^2(r, L_{box}) \tag{4.2}$$

where

$$\sigma_0^2(r) = \int_0^\infty \frac{dk}{k}\Delta^2(k)W^2(k,r) \tag{4.3}$$

is the expected value σ^2 and

$$\sigma_1^2(r,L_{box}) = \int_0^{k_f=\frac{2\pi}{L_{box}}} \frac{dk}{k}\Delta^2(k)W^2(k,r) \tag{4.4}$$

is the correction term arising due to the finite size of the simulation box.

Note that in equation (4.3) we have used the fact that perturbations at scales smaller than the grid size do not influence the growth of perturbations at large scales. This approximation is valid as long as the scales of interest are larger than a few grid lengths.

In the approach which we have outlined above, $\sigma^2(r,L_{box})$ in cosmological N-body simulations is represented by a combination of $\sigma_0^2(r)$ i.e., when the size of the simulation box is infinity, and a correction term $\sigma_1^2(r,L_{box})$. From equation (4.4) we observe that the correction term σ_1^2 is always positive; σ^2 in cosmological N-body simulation is underestimated at all scales. For hierarchical models i.e., $d\sigma_1^2(r,L_{box})/dr \leq 0$, the correction term $\sigma_1^2(r,L_{box})$ increases or saturates to a constant value as we approach small scales.

The correction term $\sigma_1^2(r,L_{box})$ can be expanded in a power series, if we assume that the scale of interest is much smaller than the size of the simulation box i.e. $r << L_{box}$

$$\begin{aligned}
\sigma_1^2(r,L_{box}) &= \int_0^{\frac{2\pi}{L_{box}}} \frac{dk}{k}\Delta^2(k)W^2(k,r) \\
&= \int_0^{\frac{2\pi}{L_{box}}} \frac{dk}{k}\frac{k^3P(k)}{2\pi^2} 9\left(\frac{\sin(kr) - kr\cos(kr)}{k^3r^3}\right)^2 \\
&\approx \int_0^{\frac{2\pi}{L_{box}}} \frac{dk}{k}\frac{k^3P(k)}{2\pi^2} - \frac{r^2}{5}\int_0^{\frac{2\pi}{L_{box}}} \frac{dk}{k}\frac{k^5P(k)}{2\pi^2} + \frac{3r^4}{175}\int_0^{\frac{2\pi}{L_{box}}} \frac{dk}{k}\frac{k^7P(k)}{2\pi^2} \\
&= C_1 - C_2r^2 + C_3r^4 + O(r^6)
\end{aligned} \tag{4.5}$$

Note that the above expansion is useful only if $k^3P(k)$ goes to zero as we approach $k = 0$. Equation (4.5) shows that the leading correction C_1 is independent of scale. This means that due to finite size of the simulation box errors are introduced at all scales. We consider the numerical values of C_i for estimating the scale below which σ_1 can be approximated by a constant value. It can be noticed that the modes closer to $2\pi/L_{box}$, contribute more significantly to the integrals that give C_i for most models.

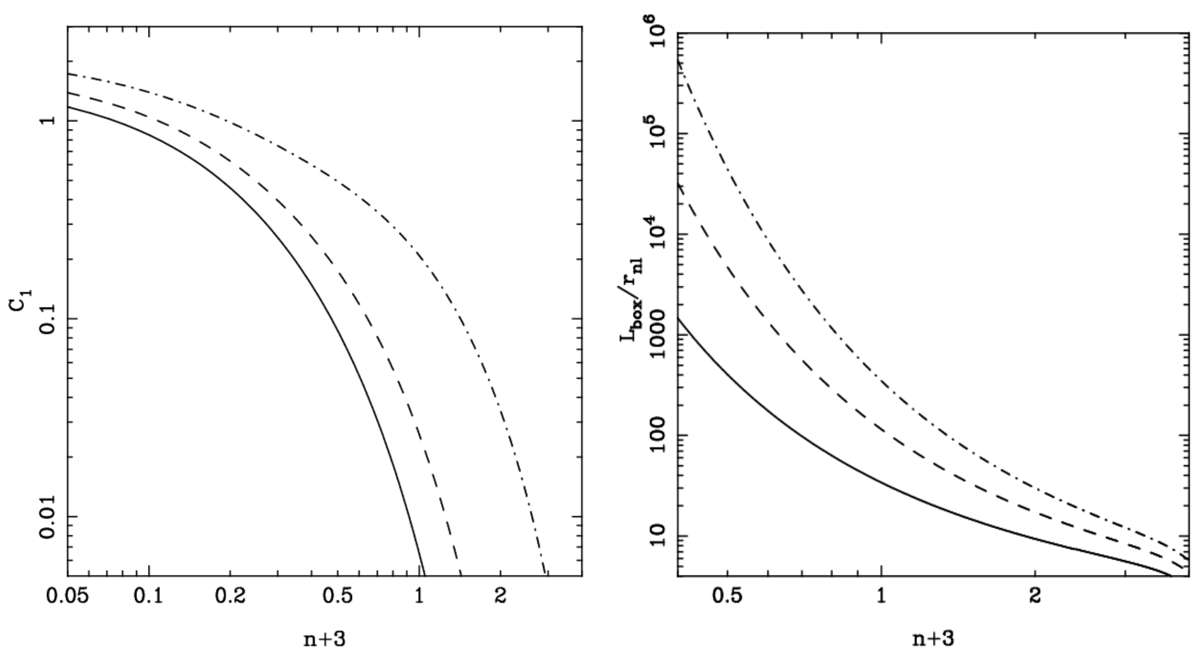

Figure 4.1: The left panel in this figure shows the variation of the leading order correction C_1 with the index of power spectrum n for different values of the size of the simulation box. The curves corresponding to $L_{box}/r_{nl} = 16, 128$ and 512 are represented by the dot-dashed, dashed and solid lines respectively. From this, we notice that the correction term becomes more and more important as n approaches towards -3. The right panel in this figure shows the variation of the size of the simulation box with the index of power spectrum for different values of C_1 $(0.01, 0.03, 0.1$ from top to bottom)

For hierarchical clustering models, $\sigma^2(r)$ at large scales is small and so the magnitudes of $\sigma_0^2(r)$ and $\sigma_1^2(r, L_{box})$ are very close to each other. However, when we approach small r, the correction $\sigma_1^2(r, L_{box})$ becomes constant and for most models it is insignificant in comparison with $\sigma_0^2(r)$. In models where $\sigma_0^2(r)$ increases very slowly at small scales or saturates to a constant value, the correction term σ_1^2 can be significant at all scales. This can be seen from the expression for C_1 for power law models i.e., $P(k) = Ak^n$.

$$C_1 = \frac{1}{n+3} \frac{A}{2\pi^2} \left(\frac{2\pi}{L_{box}} \right)^{n+3} \tag{4.6}$$

The above equation shows that the correction term C_1 becomes more and more important as $n \longrightarrow -3$ or when the the power at large scales increases.

The left panel in Figure 4.1 shows the variation of the leading order correction C_1 with the index

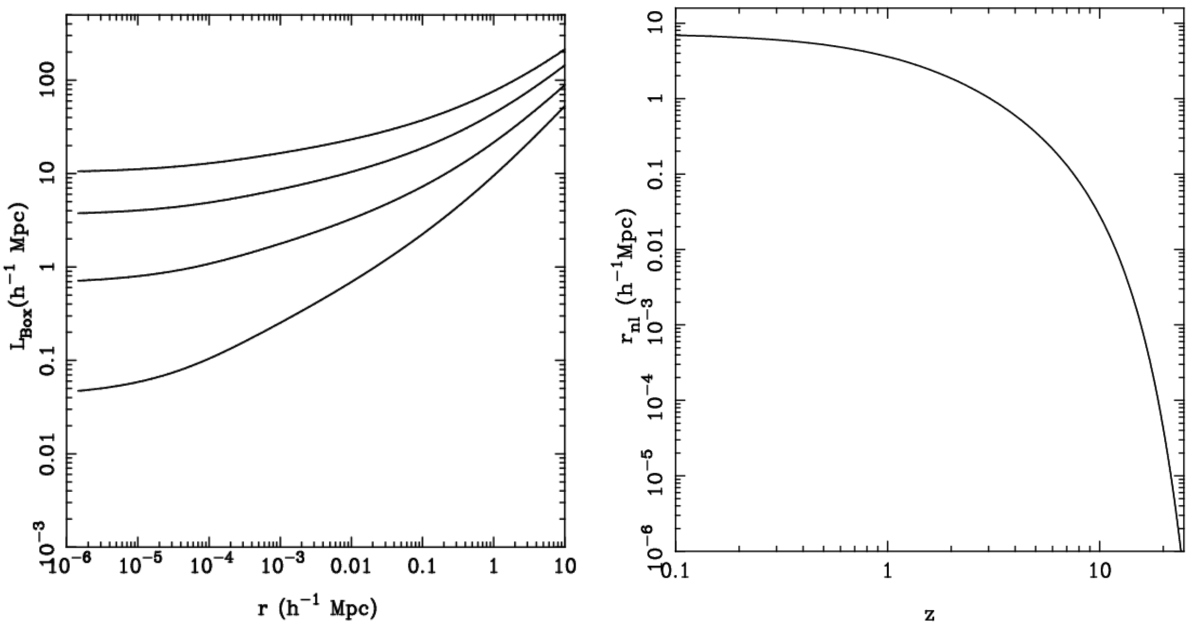

Figure 4.2: The left panel in this figure shows the contours of constant $C_1/\sigma_0^2 = 0.01, 0.03, 0.1$ and 0.3 (from top to bottom) and the right panel shows the variation of the scale of nonlinearity with redshift for the ΛCDM model.

of power spectrum n for cosmological simulations with various box sizes. The curves corresponding to $L_{box}/r_{nl} = 16, 128$ and 512 are represented by the dot-dashed, dashed and solid lines respectively. As σ_0 is unity at the scale of nonlinearity and C_1 is the first order correction, clearly we require $C_1 \ll 1$ in order to ignore the correction due to the finite size of the simulation box. For $n = -1$, if we fix $C_1 \leq 0.1$ then we can use $L_{box}/r_{nl} \geq 16$, but for a more negative value of n we require a larger separation between the box size and the scale of nonlinearity. If we keep the same accuracy then we need $L_{box}/r_{nl} = 128$, and 512, for $n = -2.3$ and -2.5 respectively. As N-body simulations are most useful for studying nonlinear evolution, even the largest simulations possible today are left with a small range of scales over which $\sigma_0 \geq 1$, for $n \leq -2.0$. This shows the pitfalls of simulating models with $n \approx -3$ over the entire range of scales.

We use C_1/σ_0^2 as a measure of correction due to finite box size. The left panel of Figure 4.2 shows the lines of constant C_1/σ_0^2 in the $L_{box} - r$ plane for the ΛCDM model. Here we have chosen $n = 1, h = 0.7, \Omega_\Lambda = 0.7, \Omega_{nr} = 0.3$ and $\sigma_8 = 0.9$ and ignored the effects of Baryons on the power

Indicator	Correction
$\xi(r)$	$C_1 - \frac{5}{6}C_2 r^2 + \frac{35}{72}C_3 r^4 + O(r^6)$
$\bar{\xi}(r)$	$C_1 - \frac{1}{2}C_2 r^2 + \frac{5}{24}C_3 r^4 + O(r^6)$

Table 4.1: This table lists corrections due to a finite box-size to indicators of clustering in the limit $r \ll L_{box}$. These expressions are equivalent to equation (4.6) and constants C_i are the same as in that equation.

spectrum. The lines from top to bottom are for various values of C_1/σ_0^2 in increasing order i.e., $0.01, 0.03, 0.1$ and 0.3. From this figure we can observe that a box of size smaller than 0.5 Mpc is precluded if we insist on $C_1/\sigma_0^2 \leq 0.1$, irrespective of the scale of interest. This implies that we cannot expect to simulate scales smaller than about 0.5kpc in the ΛCDM model without considerable improvement in the dynamic range of cosmological N-body simulations. As we are using linearly evolved quantities for our argument, the comments on size are valid irrespective of the redshift up to which the simulation is run. The contours do not change if we use σ_1^2 instead of C_1. The right panel of Figure 4.2 shows the variation of the scale of nonlinearity with redshift for the ΛCDM model.

In the right panel of Figure 4.2 we show the variation of the size of the simulation box with the index of power spectrum for a given correction i.e., C_1, in the mass variance. From this figure we observe that the size of the simulation box increseas very rapidly when we approach towards $n = -3$ for a constant correction.

The formalism which we have given can be used to estimate corrections for other estimators of clustering also. For reference, we give expressions equivalent to equation (4.6) for the correction in the two point correlation function and ξ and the average two point correlation function $\bar{\xi}$ in table 4.1. Note that for all the cases the first term is C_1.

4.3 Mass function

The mass function of collapsed objects in N-body simulation can be given by the Press-Schechter formalism (Press & Schechter, 1974; Bond et al., 1991). Since the collapsed mass function $F(M)$ depends on the mass variance $\sigma^2(M)$, we can use the correction in $\sigma^2(M)$ to compute the correction in $F(M)$. In what follows we give expressions for corrections in the Press-Schechter mass function and multiplicity function. In order to see that the key features of the corrections are generic, we also give an expression for the Sheth-Tormen mass function (Sheth & Tormen, 1999; Sheth, Mo & Tormen, 2001)

In the Press-Schechter formalism (see §1.5.4) the fraction of mass in the collapsed objects which have mass greater than M is given by

$$\begin{aligned} F(M) &= 2\int_{\delta_c}^{\infty} \frac{1}{\sqrt{2\pi}\sigma(M)} \exp\left(-\frac{\delta^2}{2\sigma^2(M)}\right) d\delta \\ &= \frac{2}{\sqrt{\pi}} \int_{\delta_c/\sigma(M)\sqrt{2}}^{\infty} \exp\left(-x^2\right) dx = \mathrm{Erfc}\left(\frac{\delta_c}{\sigma(M)\sqrt{2}}\right) \end{aligned} \tag{4.7}$$

4.3.1 Correction in mass function

The mass function $F(M, L_{box})$ which we expect in N-body simulations is given by

$$F(M, L_{box}) = \frac{2}{\sqrt{\pi}} \int_{\delta_c/\sigma(M,L_{box})\sqrt{2}}^{\infty} \exp\left(-x^2\right) dx = F_0(M) - F_1(M, L_{box}) \tag{4.8}$$

where

$$F_0(M) = \frac{2}{\sqrt{\pi}} \int_{\delta_c/\sigma_0(M)\sqrt{2}}^{\infty} \exp\left(-x^2\right) \tag{4.9}$$

is the mass function in the case when the size of the simulation box is infinity and

$$F_1(M, L_{box}) = \frac{2}{\sqrt{\pi}} \int_{\delta_c/\sigma_0(M)\sqrt{2}}^{\delta_c/\sigma(M,L_{box})\sqrt{2}} \exp\left(-x^2\right) \tag{4.10}$$

is the correction due to finite size of the simulation box. In this case also the corrections due to finite box size always lead to an underestimate of the mass function i.e., $F_1(M, L_{box})$ is always positive. This has been pointed out in earlier studies (Bagla & Ray, 2005). $F_1(M, L_{box})$ is not a monotonic function of M; it goes to zero at small as well as large M. At small scales i.e., $M < M_{nl}$, the limits of the integral in equation (4.10) differ by a very small amount and the difference $(\delta_c\sigma_1^2/2\sqrt{2}\sigma_0^3)$ keeps on decreasing as we go to smaller M while the integrand remains finite. Therefore we expect F_1 to decrease at small M. At these scales, we can write an approximate expression for $F_1(M)$:

$$F_1(M) \simeq \frac{\delta_c}{\sqrt{2\pi}} \frac{\sigma_1^2}{\sigma_0^3} \exp\left[-\frac{\delta_c^2}{2\sigma_0^2}\right] \quad . \tag{4.11}$$

This expression clearly shows that F_1 decreases as we go to small M; σ_1 goes over to the constant C_1 and σ_0 keeps increasing.

At large M ($M \gg M_{nl}$), both $\sigma(M, L_{box})$ and $\sigma_0(M)$ are small and the limits of the integral cover the region where the integrand is very small. Thus we expect $F_1(M, L_{box})$ to become smaller as we go to larger M in this regime. At these scales, we also expect F_0 and F_1 to become almost equal while $F(M, L_{box})$ goes to zero faster than either term. As $F_1(M, L_{box})$ decreases at small as well as larger scales, it must have a maxima at an intermediate scale. The scale at which the maxima occurs can be solving equation

$$\frac{dF_1}{dM} = 0 \tag{4.12}$$

substituting the value of $F_1(M, L_{box})$ from equation (4.10)

$$\frac{dF_1(M, L_{box})}{dM} = \frac{2}{\sqrt{\pi}}\left[\left(-\frac{\delta_c^2}{\sqrt{2}\sigma^2}\frac{d\sigma}{dM}\right)\exp\left[-\frac{\delta_c^2}{2\sigma^2}\right] - \left(-\frac{\delta_c^2}{\sqrt{2}\sigma_0^2}\frac{d\sigma_0}{dM}\right)\exp\left[-\frac{\delta_c^2}{2\sigma_0^2}\right]\right] = 0$$

after substituting $\sigma^2 = \sigma_0^2 - \sigma_1^2$ and some simplification we get

$$\frac{d\log\sigma_1^2}{d\log\sigma_0^2} = -\frac{\sigma_0^2}{\sigma_1^2}\left[\frac{\sigma}{\sigma_0}\left(1 - \frac{\sigma_1^2}{\sigma_0^2}\right)\exp\left[\frac{\delta_c^2\sigma_1^2}{2\sigma^2\sigma_0^2}\right] - 1\right] \simeq \frac{3}{2} - \frac{\delta_c^2}{2\sigma_0^2} \tag{4.13}$$

For $L_{box} \gg r_{nl}$, σ_1 is very well approximated by the Taylor series equation (4.5) and around this scale σ_1 is a very slowly varying function of scale. Thus $F_1(M, L_{box})$ has a maxima at $\sigma_0^2 = \delta_c^2/3 \sim 1$, if the first term in equation (4.5) is a good approximation for σ_1 (see Figure 4.3). If scale dependent terms in equation (4.5) are not ignorable then the maxima of $F_1(M, L_{box})$ shifts to smaller scales (larger σ_0) in a manner that depends on the power spectrum $P(k)$ and the size of the simulation box L_{box}.

Figure 4.3 shows the Press-Schechter mass function $F(M, L_{box})$ (solid line) for a power law model with $n = -2$ and $L_{box}/r_{nl} = 16$. The curve for the mass function $F_0(M)$ i.e., when the size of the simulation box is infinity is also shown by the solid line for reference. Curves for the exact and approximate corrections in mass function i.e., equation (4.10) and (4.11), are shown by the dot-dashed and dotted lines respectively. The scale at which $\sigma_0 = \delta_c/\sqrt{3}$ is marked with a vertical dotted line which is close to the maximum of $F_1(M, L_{box})$. The correction term $F_1(M, L_{box})$ is more than 10% of $F_0(M)$ at this scale. This figure illustrates all the generic features of the corrections to mass function that we have discussed above.

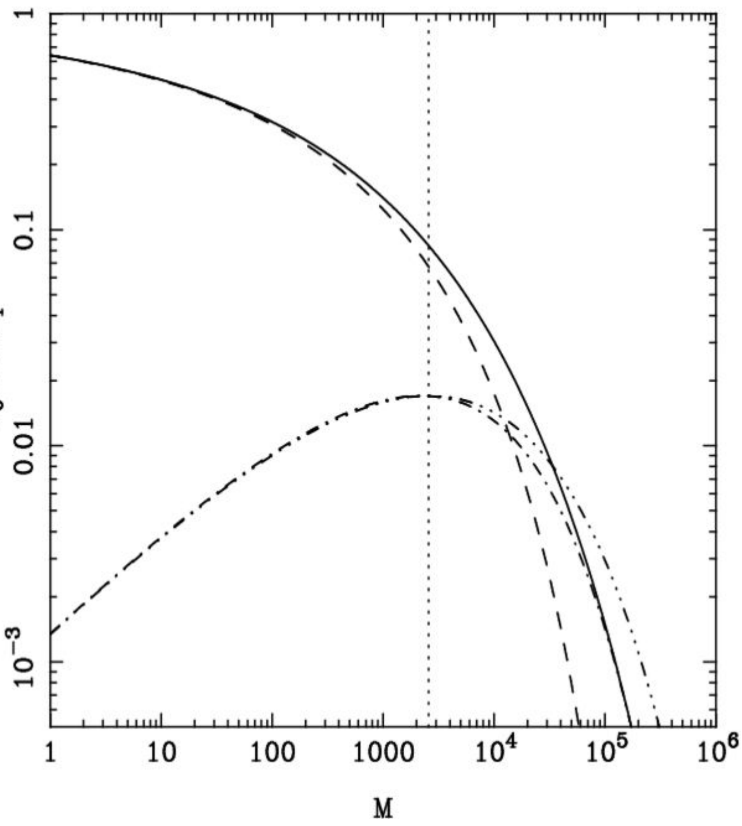

Figure 4.3: This figures shows the exact mass function $F_0(M)$ (solid line) and the mass function $F(M, L_{box})$ (dashed line) which we expect in N-body simulation (dashed line) for a power law model ($n = -2$). The exact and approximate corrections $F_1(M, L_{box})$ in mass function i.e., equation (4.10) and (4.11), are also shown by the dot-dashed and dotted lines respectively. The scale where $\sigma_0 = \delta_c/\sqrt{3}$ is marked with a vertical dotted line which coincides with the maximum of $F_1(M, L_{box})$.

4.3.2 Correction in multiplicity function

The multiplicity function f is often defined as the fraction of mass in collapsed haloes with mass in a logarithmic interval in mass:

$$\begin{aligned} f(M,L_{box}) d\log M &= -\frac{\partial F(M,L_{box})}{\partial \log M} d\log M \\ \Rightarrow f(M,L_{box}) &= -\frac{dF_0(M)}{d\log M} + \frac{\partial F_1(M,L_{box})}{\partial \log M} \\ &= f_0(M) - f_1(M,L_{box}). \end{aligned} \tag{4.14}$$

It is not possible to reduce this expression further while writing the correction term due to the finite box size separately. We can, however, ascertain generic properties of the correction term $f_1(M,L_{box})$ from our understanding of $F_1(M,L_{box})$. At large M, f_1 is positive as $F_1(M,L_{box})$ decreases with increasing M. Thus the mass fraction of haloes in this mass range is underestimated in simulations. For typical models and simulations, this is the most significant effect of a finite box size.

At the scale of nonlinearity $F_1(M,L_{box})$ has a maxima, so $f_1(M,L_{box})$ is zero and there is a scale where corrections for the multiplicity function due to finite box size vanish. At smaller scales, the slope of F_1 and hence f_1 changes sign and the correction to the mass fraction in haloes is positive. A finite box size leads to an overestimate of number of low-mass haloes. The overestimate is caused by the absence of long wave modes, as the low-mass haloes do not merge to form high mass haloes.

The magnitude of overestimate depends on σ_1, and hence on the slope of the power spectrum and L_{box}. In the limit $M \ll M_{nl}$, we can use equation (4.11) to compute the magnitude of overestimate:

$$f(M,L_{box}) \simeq f_0(M) + \frac{3\delta_c}{\sqrt{2\pi}} \frac{C_1}{\sigma_0^4} \left| \frac{d\sigma_0}{d\log M} \right| . \tag{4.15}$$

Here we have ignored the contribution of the exponential term in Eqn.(4.11). The correction term scales as $M^{(n+3)/2}$ for power law models and is thus significant even at small mass scales if $n \simeq -3$. Clearly, the term is also large for CDM like power spectra if the slope of the power spectrum is close to -3 at all scales in the simulation volume.

In Figure 4.4 we show the multiplicity functions $f_0(M)$ and $f(M,L_{box})$ by solid and dashed lines respectively for a power law model with $n = -2$ and $L_{box}/r_{nl} = 16$. The scale at which $\sigma_0 = \delta_c/\sqrt{3}$ is marked with a vertical dotted line; this scale almost coincides with the scale at which $f_1(M,L_{box})$

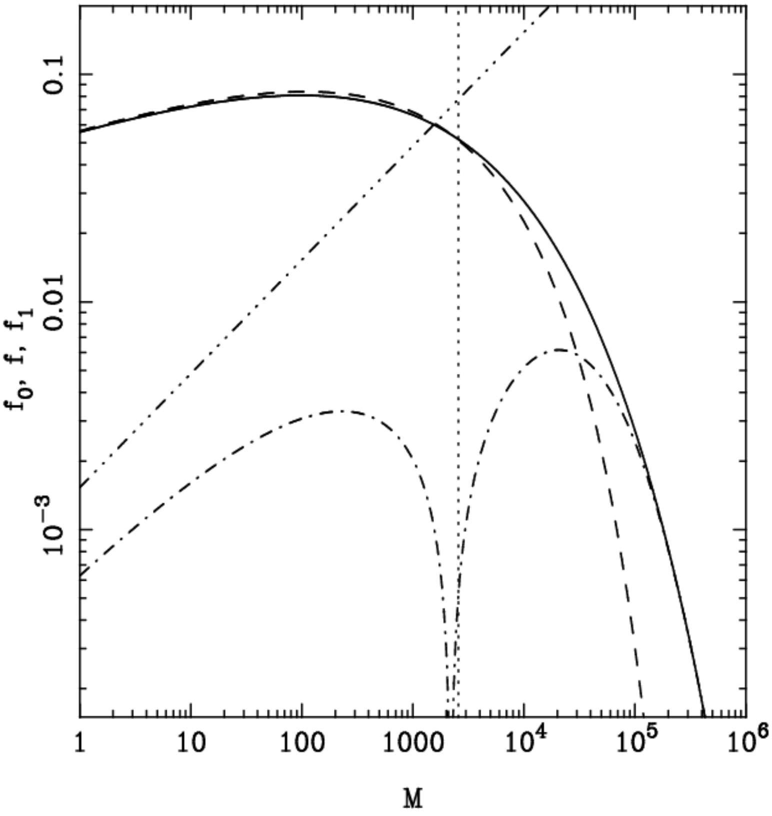

Figure 4.4: This figure shows the exact multiplicity function $f_0(M)$ (solid line) and the multiplicity function $f(M,L_{box})$ which is expected in cosmological N-body simulations. All the parameters for this figures are the same as for Figure 4.3. The exact and approximate corrections in multiplicity function $f_1(M,L_{box})$ are also shown by the dot-dashed and dot-dot-dashed lines. The scale at which $\sigma_0 = \delta_c/\sqrt{3}$ is marked with a vertical dotted line. Below this scale the correction term $f_1(M,L_{box})$ is positive and hence there are more haloes in simulation than expected in the model.

changes sign[1]. At scales below this, the correction term $f_1(M, L_{box})$ is positive and hence there are more haloes in the simulation than expected in the model. The relative magnitude of the correction term is large for $M > M_{nl}$ and this is the most significant effect of a finite box-size on the mass function. The overestimate of the multiplicity function is typically a sub-dominant effect, as it is for the model shown here. However, as we shall see below, this effect can be very significant in some situations.

Also shown in Figure 4.4 is the approximate expression for $f_1(M, L_{box})$ (dot-dot-dot-dashed curve) in the limit $M \ll M_{nl}$. Unlike the approximation for $F_1(M, L_{box})$ which is accurate over a large range of scales, this is expected to be valid only in the limit of $M \ll M_{nl}$ and indeed, is off by about a factor of two at the smallest scales shown here. However, it is a good approximation if we go to even smaller masses. We note that for this model, the overestimate of multiplicity function due to the finite box is small and therefore is difficult to detect. For this model, $C_1/\sigma_0^2 \simeq 0.2$ at the scale of nonlinearity and is smaller than 0.1 at scales where the over estimate in $f(M)$ is maximum. At small scales, f_1/f_0 is typically of the same order of magnitude as C_1/σ_0^2.

4.3.3 Correction is the Sheth-Tormen Mass Function

In order to show that the results of our analysis are generic, we compute corrections for the Sheth-Tormen mass function (Sheth & Tormen, 1999; Sheth, Mo & Tormen, 2001) also. In this case the mass function is given by:

$$F(M, L_{box}) = \frac{2}{\sqrt{\pi}} \int\limits_{\delta_c/\sigma(M,L_{box})\sqrt{2}}^{\infty} A(1 + x^{-2q}) \exp\left[-x^2\right] dx \qquad (4.16)$$

In the limit of $A = 0.5$ and $q = 0$ this is identical to the usual Press-Schechter mass function (equation (4.7)). The maxima of the correction term $F_1(M, L_{box})$ occurs when the following equation is

---

[1] The change of sign happens at $\sigma_0 = 1$ instead of $\sigma_0 = 0.97$ drawn here with $\delta_c = 1.68$.

satisfied:

$$\begin{aligned}\frac{d\log\sigma_1^2}{d\log\sigma_0^2} &= -\frac{\sigma_0^2}{\sigma_1^2}\left[\frac{\sigma}{\sigma_0}\left(1-\frac{\sigma_1^2}{\sigma_0^2}\right)\exp\left(\frac{\delta_c^2\sigma_1^2}{2\sigma^2\sigma_0^2}\right)\frac{1+\left(\frac{\delta_c}{\sqrt{2}\sigma_0}\right)^{-2q}}{1+\left(\frac{\delta_c}{\sqrt{2}\sigma}\right)^{-2q}}-1\right] \\ &\simeq \frac{3}{2}-\frac{\delta_c^2}{2\sigma_0^2}-q\left(\frac{\delta_c}{\sqrt{2}\sigma_0}\right)^{-2q} \qquad (4.17)\end{aligned}$$

As before, this reduces to the expression in the Press-Schechter case (equation (4.7)) in the limit $q = 0$. The qualitative features of the finite box correction to mass function are the same for the two prescriptions and may be considered to be generic. For reference, we write approximate expressions for correction to the mass function $F(M)$:

$$F_1 \simeq \frac{\delta_c}{\sqrt{2\pi}}\frac{\sigma_1^2}{\sigma_0^3}\exp\left[-\frac{\delta_c^2}{2\sigma_0^2}\right]A\left[1+\left(\frac{\delta_c}{\sqrt{2}\sigma_0}\right)^{-2q}\right] \qquad (4.18)$$

and the multiplicity function $f(M)$:

$$f_1 = \frac{3\delta_c}{\sqrt{2\pi}}\frac{C_1}{\sigma_0^4}\left(\frac{d\sigma_0}{d\log M}\right)A\left[1+\left(1-\frac{2q}{3}\right)\left(\frac{\delta_c}{\sqrt{2}\sigma_0}\right)^{-2q}\right] \qquad (4.19)$$

for the Sheth-Tormen mass function.

4.3.4 N-Body Simulations

In order to check the predictions of our formalism we have also carried out a set of cosmological N-body simulations. Here we do not try to fit for either the Press-Schechter or Sheth-Tormen mass function to simulations. Instead we use a simulation with a larger L_{box} as reference and compare the number density of haloes as a function of mass with another simulation with a smaller L_{box}.

For N-body simulations we have considered a power law model with index $n = -2$ and normalized it such that the scale of nonlinearity at the final epoch was 8 grid lengths. We consider the size of the simulation box for the smaller and larger simulations to be 64 and 256 grid lengths respectively. The smaller simulation was carried out with the TreePM code (Bagla, 2002; Bagla & Ray, 2003) and the larger simulation was carried out with a parallel version of the TreePM code (Ray & Bagla, 2004).

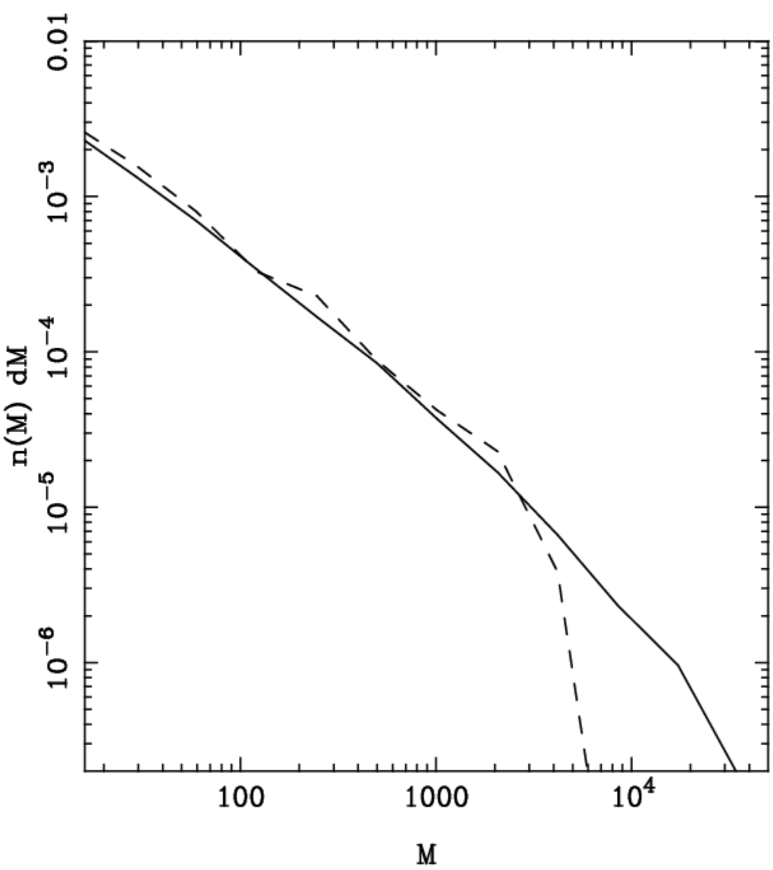

Figure 4.5: This figure shows the comoving number density of haloes $n(M)dM$ in the mass range $M - M + dM$ for the large (solid line) and small (dashed line) simulations (see text). From this figure we observe that the number density of low mass haloes is overestimated in the case of smaller simulations as is expected in this formalism.

Figure 4.5 shows the number density of haloes $n(M)dM$ in cosmological N-body simulation for a power law model ($n = -2$) with $L_{box} = 64$ (dashed line) and $L_{box} = 256$ (solid line). Note that according to our definitions $n(M) = f(M)/M^2$, where $f(M)$ is the multiplicity function. One can see that the number density varies approximately as a power law at small M and rapidly falls at large M. As expected from our analysis the deviation from power law starts at smaller masses as the number density of very massive haloes is underestimated in smaller simulations as compared to the the bigger one i.e, the reference simulation. At smaller M, we find about 10% more haloes in smaller simulation as compared to the reference one. It is noteworthy that the number density of low mass haloes remains above that in the reference simulation at all masses below the rapid drop around 10^3. Both of the above features follow the predictions of our formalism. Indeed we have shown that these features are independent of the specific analytical form for the mass function. Here we have also shown that the same behavior is reproduced in N-Body simulations. A more detailed comparison with N-body simulations is presented in Chapter 6.

4.4 Summary & Conclusions

In the present study we have given an analytic prescription for computing corrections due to the finite box size in cosmological N-body simulations for mass variance, Press-Schechter mass function and multiplicity function. We have shown that the corrections are typically small if the scale of interest and the scale of nonlinearity are sufficiently small compared to the size of the simulation box. In particular, if the scale of nonlinearity is not much smaller than the size of the simulation box, we not only ignore power in modes larger than the simulation box but also the significant effects of mode coupling from scales in the mildly nonlinear regime. This means that cosmological N-body simulations are reliable only when $r, r_{nl} << L_{box}$.

In our formalism we have proposed σ_1^2/σ_0^2 as an indicator of the significance of finite box size; any descriptor of the second moment of density can be used for this purpose but σ has the virtue of being positive definite at all scales. Our proposal is that $\sigma_1^2(r)/\sigma_0^2(r)$ and $\sigma_1^2(r_{nl}(z))/\sigma_0^2(r_{nl}(z))$ have to be much smaller than unity in order to ignore the corrections due to finite box size. Conversely, the ratio σ_1/σ_0 at the scale of interest is indicative of the magnitude of correction due to the finite box-size. For a given relative magnitude of correction term (σ_1/σ_0), L_{box}/r_{nl} is required to be larger for a power spectrum with more large scale power. Indeed, the required L_{box}/r_{nl} approaches infinity as the slope of the power spectrum approaches -3.

In the present study we have shown that the clustering amplitude $\sigma^2(M)$, mass functions $F(M)$ and multiplicity functions $f(M)$ are significantly affected by the size of simulation box if the scale of nonlinearity is not much smaller than the size of the simulation box. Apart from quantitative effects, the size of the simulation box can also lead to quantitative effects. For example, due to finite box corrections, the amplitude of the density perturbations no longer remains a power law and the range of scales over which it can be approximated by one becomes smaller as $n+3 \longrightarrow 0$. Since in the linear regime, the radial pair velocity is related directly to the average two point correlation function $\bar{\xi}$ (Peebles, 1980; Nityananda & Padmanabhan, 1994) and $\bar{\xi}$ is not a pure power law in simulations due to box-size corrections, we expect that the pair velocities must also deviate from expected values. This in turn leads to deviations from the self similar growth of density perturbations. This explains the difficulty in getting scale invariant evolution for models like $n = -2$ in N-Body simulations (Jain & Bertschinger, 1996; Jain & Bertschinger, 1998) For realistic models like the ΛCDM, the correction term is significant only if the scales of interest are below a few kpc and becomes larger as we move to smaller scales (see Figure 4.2). Indeed, at these small scales we may require $L_{box}/r \sim 10^4$ or even greater in order to manage $C_1/\sigma_0^2 = 0.1$. Of course, a bigger simulation volume is required if we demand better accuracy. On the other hand, if we are interested in scales larger than 10^2kpc, present day simulations are sufficient for keeping $C_1/\sigma_0^2 \leq 0.01$.

We have shown that at sufficiently small scales the correction due to finite box size can be written as a series of progressively smaller terms. The first correction term (C_1) is shown to be positive definite. We have also shown that the first correction term is the same for two point correlation function and σ^2; indeed it is the same for all descriptors of the second moment for which the effective window function goes to unity at small k.

As an application of our method, we have discussed corrections to mass function and multiplicity function using the Press-Schechter as well as the Sheth-Tormen approach for a power law model with $n = -2$. We have also given approximate expressions for the correction term and have shown that the approximation is very good in case of the mass function. The mass function is always under estimated in simulations due to finite box-size corrections. The multiplicity function, and hence also the number density of haloes of a given mass are underestimated at $M > M_{nl}$. At smaller mass scales, however, the multiplicity function is overestimated and we find a greater number of haloes in simulations than expected in the model. The mass scale at which the crossover from underestimate to overestimate occurs is given by equation (4.14).

The overestimate at small scales is related to the underestimate of mass in haloes at large scales. If the full power spectrum had been taken into account, the smaller haloes would have merged to form more massive haloes. In the absence of large scale modes, the formation of massive haloes is slowed down and a larger number of low mass haloes survive. A detailed analysis of the effect of finite box size correction on the formation and destruction rate of haloes will be presented in the next chapter. Of significant interest is the impact on rates of major mergers (Cohn, Bagla & White, 2001) as these have implications for observations.

We have found that the overestimate in multiplicity function is large whenever the ratio $\sigma_1^2(r,L_{box})/\sigma_0^2(r) \sim C_1(L_{box})/\sigma_0^2(r)$ is large. To illustrate this correlation, we have plotted the multiplicity function $f_0(M)$ for the ΛCDM model in Figure 4.6. This has been plotted for redshift $z = 20$ and $z = 15$ and the mass range has been chosen such that a very large box size is required to keep $\sigma_1^2(r,L_{box})/\sigma_0^2(r)$ smaller than 0.1. We have also plotted $f(M,L_{box})$ here, with $L_{box} = 5\mathrm{h}^{-1}$kpc (dotted curve), $L_{box} = 20\mathrm{h}^{-1}$kpc (dot-dashed curve) and $L_{box} = 100\mathrm{h}^{-1}$kpc (dashed curve). These correspond to $C_1/\sigma_0^2 \simeq 0.6$, 0.3 and 0.19, respectively.

In the top and bottom rows of Figure 4.6 we show the Press-Schechter and Sheth-Tormen mass function for the LCDM model at two epochs, $z = 20$ (left column) and $z = 15$ (right column). In each panel the curve for the theoretical model i.e., when the size of the simulation box is infinitely large, is shown by the solid line and curves for the cases $L_{box} = 5h^{-1}$kpc, $20h^{-1}$kpc and $100h^{-1}$kpc are shown by the solid, dot-dashed and dashed lines respectively. It is noteworthy that the relative error is similar for both the cases, even though the multiplicity function itself is different. At $z = 20$, the multiplicity function is underestimated by a large amount for $L_{box} = 5\mathrm{h}^{-1}$kpc, even though $L_{box}/r_{nl} \simeq 120$, and if we are interested in scales around 1pc then $L_{box}/r \simeq 5000$. The situation

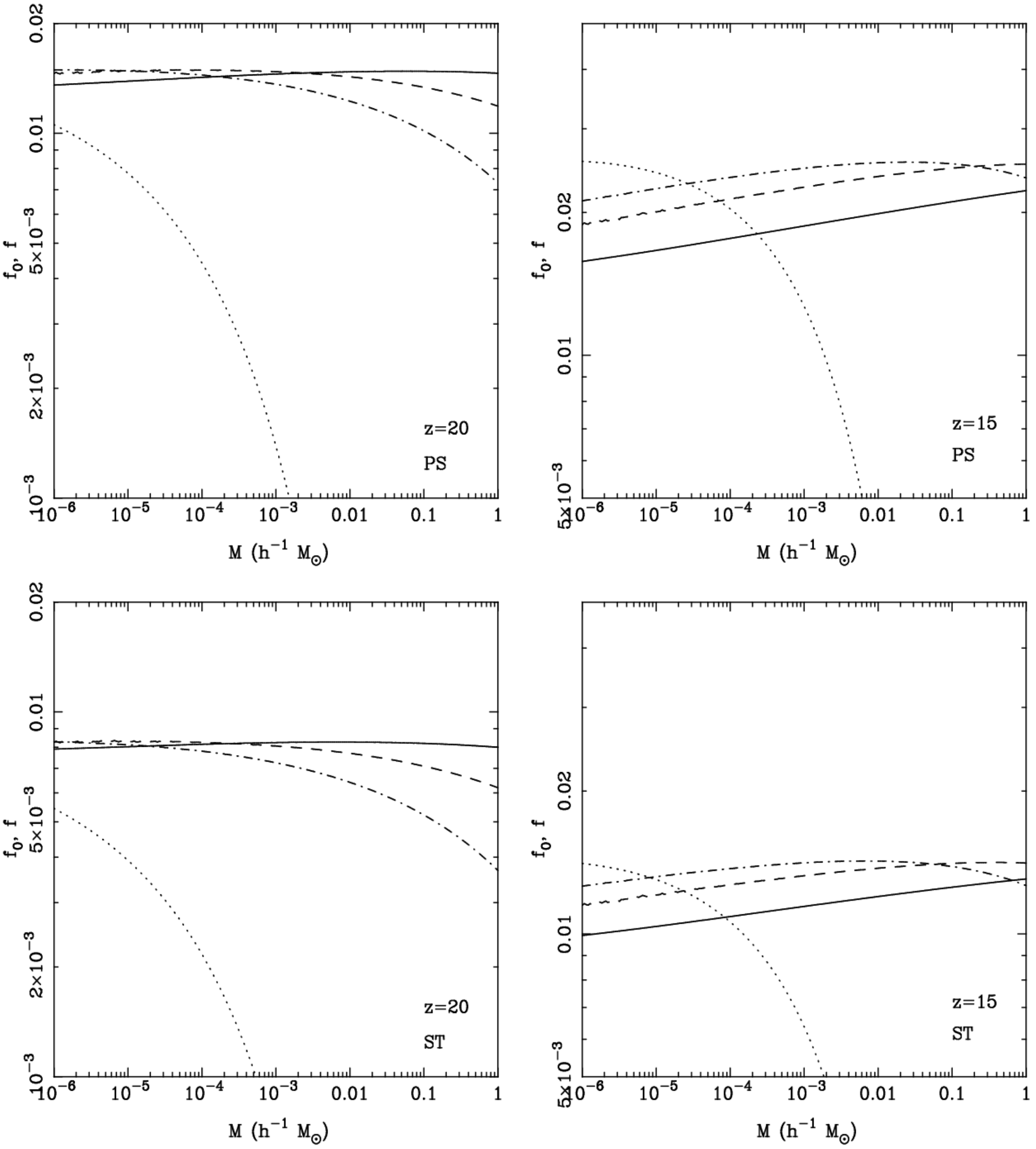

Figure 4.6: The multiplicity function expected in the ΛCDM model (see text for details). The top row is for Press-Schechter mass function and the lower row is for Sheth-Tormen mass function. The left column is for $z = 20$ and the right column is for $z = 15$. The expected multiplicity function is plotted as a function of mass, shown in each panel by a solid curve. Other curves correspond to multiplicity for a finite simulation box: $L_{box} = 5\mathrm{h}^{-1}$kpc (dotted curve), $L_{box} = 20\mathrm{h}^{-1}$kpc (dot-dashed curve) and $L_{box} = 100\mathrm{h}^{-1}$kpc (dashed curve). These correspond to $C_1/\sigma_0^2 \simeq 0.6$, 0.3 and 0.19, respectively.

at small masses is better for the other two simulation volumes considered here. For $z = 15$, the scale of non-linearity is $r_{nl} = 1.4\text{h}^{-1}$kpc, very close to $L_{box} = 5\text{h}^{-1}$kpc, and hence we do not expect believable results for this box-size. Indeed, the two panels on the right demonstrate the large errors and the absurdly incorrect shape of the multiplicity function. The difference in $f(M, L_{box})$ and $f_0(M)$ at $10^{-6} M_\odot$ is about 25% for $C_1(L_{box})/\sigma_0^2 = 0.3$. In this case $L_{box} = 20\text{h}^{-1}$kpc and $L_{box}/r \simeq 2 \times 10^4$. The error in the multiplicity function is slightly larger than 10% for $L_{box} = 100\text{h}^{-1}$kpc even though $L_{box}/r \simeq 10^5$ and $L_{box}/r_{nl} \simeq 67$. The multiplicity function plotted here is the global function, and the conditional mass functions should be used in order to estimate errors in simulations where a high peak is studied at better resolution. Similar results are obtained for other mass functions that have been suggested as a better fit to simulation data (Jenkins et al., 2001; Warren et al., 2006)

From the above discussion it is clear that the results of cosmological N-body simulations cannot be reliable if $C_1(L_{box})/\sigma_0^2(r)$ is close to unity. One may argue that models for mass function have not been tested in this regime where the local slope of the power spectrum is very close to -3, but the fact that error in amplitude of density perturbations itself is large should be reason enough to worry about reliability of results. Further, the agreement in the magnitude of errors for the several approaches to the mass function also gives us some confidence in our results.

We conclude that most of the cosmological N-body simulations are not affected by the errors introduced by the finite size of the simulation box, as the slope of the initial power spectrum approaches -3 only at very small scales (large wave numbers). However, high resolution simulations of earliest structure formation in the ΛCDM model need to have a very large dynamic range before the results can be believed within 10% of the quoted value. Indeed, our study may have some relevance to the ongoing discussion about the Earth mass haloes (Diemand, Moore & Stadel, 2005; Zhao et al., 2007)

We note that it is extremely important to understand the sources of errors in N-Body simulations and the magnitude of errors in quantities of physical interest. N-Body simulations are used to make predictions for a number of observational projects and also serve as a test bed for methods. In this era of "precision cosmology", it will be tragic if simulations prove to be a weak link. We would like to note that our results apply equally to all methods of doing cosmological N-Body simulations, save those where techniques like MAP are used to include the effects of scales larger than the simulation volume.

The method for estimating errors due to a finite box-size described in this chapter can be used for several physical quantities. In the present study we have used the method to study errors in clustering properties and mass functions i.e., rms fluctuations in mass, mass functions and multiplicity functions. In the next chapter we will study the effects of finite box size on the formation and destruction rate of haloes.

Chapter 5

Finite volume effects -II: Formation rate

5.1 Introduction

The mass function of collapsed objects in nonlinear gravitational clustering is an important measure which can be used to compare theoretical models with observations. In particular, the Press-Schechter (Press & Schechter, 1974) mass function has been used in many semianalytic studies which bridge the gap between the linear perturbation theory and cosmological N-body simulations. However, the mass function does not contain all the information which is needed for various physical processes. For example, if we want to know the comoving number density of ionizing sources at any redshift then the mass function contains insufficient information since not all bound objects become the source of ionizing radiation; only those objects become sources which form during a particular period of time (Chiu & Ostriker, 2000). In this situation we need to know the formation and destruction rate of collapsed objects as a function of the cosmological redshift. The rate at which quasars form in the early universe depends in an important way on the merger rate which is another manifestation of the formation rate (Carlberg, 1990). From the above discussion it is clear that the formation and destruction rates are important measures in nonlinear gravitational clustering. In the present chapter we will use the formalism which we have proposed in Chapter 4 and give the expressions for corrections in the formation and destruction rate due to the finite size of the simulation box.

On the basis of an excursion set approach, Bond et al (Bond et al., 1991) gave expressions for the fraction of mass that is incorporated in objects of a given mass at a given redshift. These expressions can also be used to compute the conditional probabilities and merger rates. Bower (Bower, 1991) studied the infall rate of galaxies using the conditional probabilities obtained from the Press-Schechter formalism and compared these with cosmological N-body simulations. In this study it was also shown that the conditional multiplicity function can be used to compute the rate at which clusters of galaxies accumulate mass due to merging i.e., infall rate. Lacey and Cole (Lacey & Cole, 1993; Lacey & Cole, 1994) did a very detailed analysis of merging of haloes in gravitational clustering using the Press-Schechter formalism and derived an expression for the merger rate in terms of the halo mass, epoch and the initial power spectrum. They argued that merger is a common process in hierarchical clustering models and plays an important role in the formation of the present day galaxy population. In order to derive the relations for the merger rate, accretion rate and other physical quantities, Lacey and Cole followed the excursion set approach of Bond et al. (Bond et al., 1991).

Cohn, Bagla & White (Cohn, Bagla & White, 2001) used the extended-Press-Schechter formalism and obtained analytic expressions for the major merger counts and compared these with high resolution N-body simulations. One of the main aims of their study was to address the question of how many major mergers a halo has gone through in a given period of time. This question is important not only for simulation studies, but also has observational applications. In most of the above mentioned studies conditional probabilities, multiplicities, merger rate etc., are computed on the basis of the Press-Schechter formalism or using N-body simulations. This means that the formalism which we have introduced in the last chapter for finding corrections in the mass function due to the finite size of the simulation box can be used for the merger rate and other physical quantities. In the present chapter we consider the formation and destruction rates as defined in (Sasaki, 1994; Kitayama & Suto, 1996) for our analysis.

The plan of the chapter is as follows. Following the approach given by of Sasaki (Sasaki, 1994) and Kitayama & Suto (Kitayama & Suto, 1996) we give expressions for formation rate, destruction rate, rate of change of number density in §5.2. We give our main results in the form of analytic expressions for corrections in formation and destruction rate in §5.3 and use these for power law

($n = -2$) and the LCDM models. We summarize the main results of study in §5.4 and conclude. The main results of the present study have been published in Prasad (2007).

5.2 Basic Equations

5.2.1 Formation and destruction rate

In the Press-Schechter formalism (see §1.5.4) the comoving number density $N_{PS}(M,t)dM$ of objects which have mass in the range $[M, M+dM]$ at time t is given by

$$\begin{aligned} N_{PS}(M,t)dM &= \frac{\rho_0}{M} \times \left| \frac{dF(M)}{dM} \right| dM \\ &= \sqrt{\frac{2}{\pi}} \frac{\rho_0}{M} \left(-\frac{\delta_c(t)}{\sigma^2(M)} \frac{d\sigma(M)}{dM} \right) \exp\left(-\frac{\delta_c^2(t)}{2\sigma^2(M)} \right) dM \end{aligned} \tag{5.1}$$

Here $\delta_c(t) = \delta_c/D(t)$ and $D(t)$ is the linear growth factor which depends on the cosmological model being considered and $\delta_c(t)$ is taken to be 1.68 at the present epoch.

From equation (5.1) we can write an expression for the rate of change of comoving number number density per unit time for objects which have mass in the range $[M, M+dM]$

$$\begin{aligned} \left(\frac{dN_{PS}(M,t)}{dt} \right) dM = & \sqrt{\frac{2}{\pi}} \frac{\rho_0}{M} \left(\frac{1}{D^2(t)} \frac{dD(t)}{dt} \right) \left(\frac{\delta_c}{\sigma^2(M)} \frac{d\sigma(M)}{dt} \right) \\ & \times \left[1 - \frac{\delta_c^2}{\sigma^2(M) D^2(t)} \right] \exp\left(-\frac{\delta_c^2}{2\sigma^2(M) D^2(t)} \right) dM \end{aligned} \tag{5.2}$$

The first and second term in the right hand side of the above equation can be identified with the formation rate and destruction rate respectively (Sasaki, 1994; Kitayama & Suto, 1996).

$$\begin{aligned} \left(\frac{dN_{PS}(M,t)}{dt} \right) dM &= -\frac{1}{D(t)} \frac{dD(t)}{dt} \left[1 - \frac{\delta_c^2}{\sigma^2(M) D^2(t)} \right] N_{PS}(M,t) dM \\ &= -\left(\frac{dN_{Dest}(M,t)}{dt} \right) dM + \left(\frac{dN_{Form}(M,t)}{dt} \right) dM \end{aligned} \tag{5.3}$$

The formation rate $(dN_{Form}(M,t)/dt)dM$ quantifies the change in the comoving number density of objects around mass M, per unit time, due to the formation of objects in that mass range when objects of mass smaller than M merge together.

$$\begin{aligned}\left(\frac{dN_{Form}(M,t)}{dt}\right)dM &= \frac{1}{D(t)}\frac{dD(t)}{dt}\left[\frac{\delta_c^2}{\sigma^2(M)D^2(t)}\right]N_{PS}(M,t)dM \\ &= \sqrt{\frac{2}{\pi}}\frac{\rho_0}{M}\left(\frac{1}{D^4(t)}\frac{dD(t)}{dt}\right)\left(-\frac{\delta_c^3}{\sigma^4(M)}\frac{d\sigma(M)}{dt}\right) \\ &\times\exp\left(-\frac{\delta_c^2}{2\sigma^2(M)D^2(t)}\right)dM \qquad (5.4)\end{aligned}$$

The destruction rate $(dN_{Dest}(M,t)/dt)dM$ quantifies the rate of change of comoving number density of haloes in the mass range $[M, M+dM]$ when the haloes in that mass range merge together and form bigger haloes.

$$\begin{aligned}\left(\frac{dN_{Dest}(M,t)}{dt}\right)dM &= \frac{1}{D(t)}\frac{dD(t)}{dt}N_{PS}(M,t)dM \\ &= \sqrt{\frac{2}{\pi}}\frac{\rho_0}{M}\left(\frac{1}{D^2(t)}\frac{dD(t)}{dt}\right)\left(-\frac{\delta_c}{\sigma^2(M)}\frac{d\sigma(M)}{dt}\right)dM \\ &\times\exp\left(-\frac{\delta_c^2}{2\sigma^2(M)D^2(t)}\right)dM \qquad (5.5)\end{aligned}$$

5.3 Correction in formation and destruction rate

From equation (5.1), (5.2), (5.4) and (5.5), we see that the comoving number density of haloes, formation rate, destruction rate and the rate of change of comoving number density of haloes in the mass range $[M, M+dM]$ is related to the mass variance $\sigma^2(M)$. This means that on the basis of the correction in the mass variance $\sigma^2(M)$ due to finite size of the simulation box (see equation (4.2)) we can find the corrections in these physical quantities also.

5.3.1 Corrections in comoving number density

The comoving number density of haloes $N_{PS}(M,t)dM$ in the mass range $[M, M+dM]$ which we expect in cosmological N-body simulations is given by

$$\begin{aligned}N_{PS}(M,t)dM &= \sqrt{\frac{2}{\pi}}\frac{\rho_0}{M}\frac{\delta_c}{D(t)}\left(-\frac{1}{\sigma^2(M)}\frac{d\sigma(M)}{dM}\right)\exp\left(-\frac{\delta_c^2}{2\sigma^2(M)D^2(t)}\right)dM \\ &= N_{PS_0}(M,t)dM - N_{PS_1}(M,t)dM \qquad (5.6)\end{aligned}$$

Here $N_{PS_0}(M,t)$ and $N_{PS}(M,t)$ are the theoretical (box size infinite) and the actual (box size finite) comoving number densities respectively where

$$N_{PS_0}(M,t)dM = \sqrt{\frac{2}{\pi}}\frac{\rho_0}{M}\frac{\delta_c}{D(t)}\left(\frac{-1}{\sigma_0^2(M)}\frac{d\sigma_0(M)}{dM}\right)\exp\left(\frac{-\delta_c^2}{2\sigma_0^2(M)D^2(t)}\right)dM \tag{5.7}$$

and

$$\begin{aligned} N_{PS_1}(M,t)dM = \frac{1}{2}\Bigg[1-&\left(1-\frac{\sigma_1^2}{\sigma_0^2}\right)^{-3/2}\left(1-\frac{d\sigma_1^2}{d\sigma_0^2}\right) \\ &\times\exp\left\{-\frac{\delta_c^2}{2D^2(t)}\left(\frac{1}{\sigma^2}-\frac{1}{\sigma_0^2}\right)\right\}\Bigg]N_{PS_0}(M,t)dM \end{aligned} \tag{5.8}$$

or

$$N_{PS_1}(M,t)dM \approx \frac{1}{2}\left[\frac{d\sigma_1^2}{d\sigma_0^2}-\frac{3\sigma_1^2}{2\sigma_0^2}+\frac{\delta_c^2\sigma_1^2}{2D^2(t)\sigma_0^4}\right]N_{PS_0}(M,t)dM \;\text{ if } \sigma_1^2/\sigma_0^2 < 1 \tag{5.9}$$

In equation (5.9) the coefficient of $N_{PS_0}(M,t)$ changes sign at the scale for which $\sigma_0 \approx \delta_c/D(t)\sqrt{3} = \delta_c(t)/\sqrt{3}$ so the number density of objects below this scale is overestimated and the number density above this is scale underestimated. This is in accordance with our earlier results (BP06). The left and right panels of Figure 5.1 show the theoretical comoving number density $N_{PS_0}dM$ (solid lines) and the comoving number density $N_{PS}dM$ (dashed line) as is expected in cosmological N-body simulations for the power law model ($n = -2$) and the LCDM model respectively. For the power law model we consider the size of the simulation box to be 128 grid lengths and compute $N(M)$ at $z = 0$. We normalize the power spectrum such that the scale of nonlinearity at $z = 0$ is 8 grid lengths. For the LCDM model the size of the simulation box is 10 h^{-1} Mpc and calculation is shown for $z = 6$. In this case the scale of nonlinearity at $z = 0$ is $8h^{-1}$Mpc. In both the panels the actual and approximate corrections in the comoving number density are shown by the dot-dashed and dotted lines. This figure clearly shows that for both case i.e., power law and LCDM, cosmological N-body simulations underpredict the comoving number density of large mass haloes and overpredict that of the small mass haloes.

5.3.2 Formation rate

The formation rate of haloes $(dN_{Form}(M,t)/dt)dM$ in the mass range $[M, M+dM]$ in an N-body simulation is given by equation (5.4)

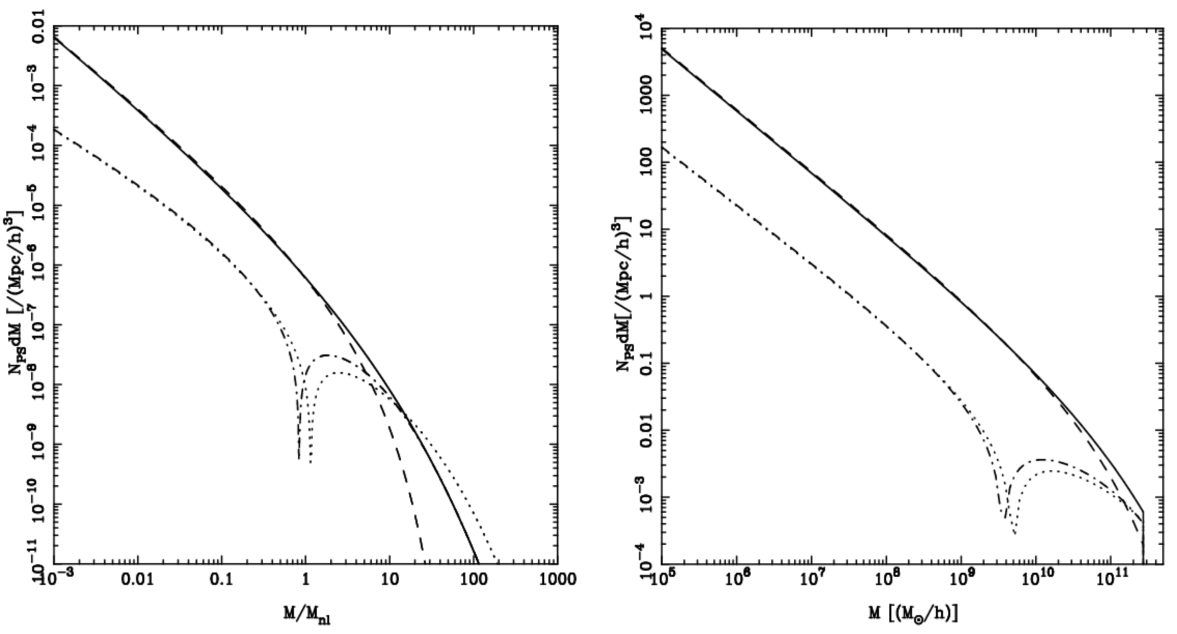

Figure 5.1: The left and right panels of this figure show the theoretical value of the comoving number density i.e., $N_{PS_0}dM$ (solid line), and the number density as is expected in N-body simulation i.e., $N_{PS}dM$ (dashed line) for a power law ($n = -2$) and LCDM model respectively. In the case of the power law model we consider the size of the simulation box to be 128 grid lengths at $z = 0$. The scale of nonlinearity is taken to be 8 grid lengths. For the LCDM case we take the size of the simulation box 10 h^{-1}Mpc and plot values at $z = 6$. In this case the scale of nonlinearity is $8h^{-1}$Mpc at $z = 0$. We also show the magnitude of exact and approximate corrections in the comoving number density $N_{PS_1}dM$ by the dot-dashed and dotted lines (see text for details).

$$\begin{aligned}\left(\frac{dN_{Form}(M,t)}{dt}\right)dM &= \sqrt{\frac{2}{\pi}}\frac{\rho_0}{M}\left(\frac{1}{D^4(t)}\frac{dD(t)}{dt}\right)\left(-\frac{\delta_c^3}{\sigma^4(M)}\frac{d\sigma(M)}{dt}\right)\\ &\quad\times\exp\left(-\frac{\delta_c^2}{2\sigma^2(M)D^2(t)}\right)dM\\ &= \left(\frac{dN_{Form_0}(M,t)}{dt}\right)dM - \left(\frac{dN_{Form_1}(M,t)}{dt}\right)dM \qquad (5.10)\end{aligned}$$

Here $(dN_{Form_0}(M,t)/dt)dM$ and $(dN_{Form_1}(M,t)/dt)dM$ are the theoretical formation rate and the correction term respectively where

$$\begin{aligned}\left(\frac{dN_{Form_0}(M,t)}{dt}\right)dM &= \sqrt{\frac{2}{\pi}}\frac{\rho_0}{M}\left(\frac{1}{D^4(t)}\frac{dD(t)}{dt}\right)dM \\ &\times\left(-\frac{\delta_c^3}{\sigma_0^4(M)}\frac{d\sigma_0(M)}{dt}\right)\exp\left(-\frac{\delta_c^2}{2\sigma_0^2(M)D^2(t)}\right)\end{aligned} \tag{5.11}$$

and

$$\begin{aligned}\left(\frac{dN_{Form_1}(M,t)}{dt}\right)dM &= \frac{1}{2}\left[1-\left(1-\frac{\sigma_1^2}{\sigma_0^2}\right)^{-5/2}\left(1-\frac{d\sigma_1^2}{d\sigma_0^2}\right)\right. \\ &\left.\times\exp\left\{-\frac{\delta_c^2}{2D^2(t)}\left(\frac{1}{\sigma^2}-\frac{1}{\sigma_0^2}\right)\right\}\right]\left(\frac{dN_{Form_0}(M,t)}{dt}\right)dM\end{aligned} \tag{5.12}$$

or

$$\left(\frac{dN_{Form_1}(M,t)}{dt}\right)dM \approx \frac{1}{2}\left[\frac{d\sigma_1^2}{d\sigma_0^2}-\frac{5\sigma_1^2}{2\sigma_0^2}+\frac{\delta_c^2\sigma_1^2}{2D^2(t)\sigma_0^4}\right]\left(\frac{dN_{Form_0}(M,t)}{dt}\right)dM \tag{5.13}$$

if $\sigma_1^2/\sigma_0^2 < 1$ The left and right panels of Figure 5.4 show the theoretical formation rate $(dN_{Form_0}/dt)dM$ and the formation rate $(dN_{Form}/dt)dM$ which we expect in cosmological N-body simulations for the power law and LCDM models respectively. In this figure the parameters for the power law and LCDM model are the same as in Figure 5.1. Since the formation rate is directly proportional to the comoving number density, it follows the same trend as the comoving number density. However, in this case the scale at which the correction term changes sign is different from the scale at which the correction term for the comoving number density changes sign i.e., here it is the scale for which $\sigma_0 = \delta_c/D(t)\sqrt{5} = \delta_c(t)/\sqrt{5}$. This figure shows that the formation rate of massive haloes is suppressed and that of low mass haloes is enhanced in cosmological N-body simulations due to the finite size of the simulation box. The main reason behind the suppression of the formation of large mass haloes is the absence of fluctuations in the initial density field at large scales due to truncation of power.

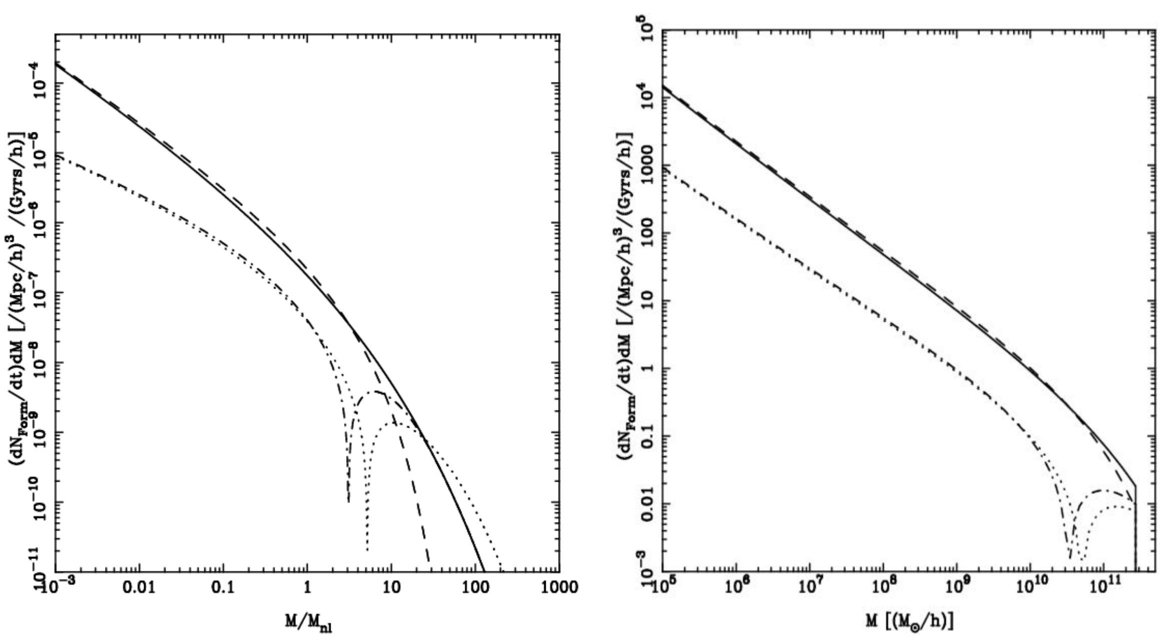

Figure 5.2: The left and right panels in this figure show the theoretical formation rate i.e., $(dN_{Form_0}/dt)dM$ (solid line) and the formation rate $(dN_{Form}/dt)dM$ (dashed-line) which we expect in cosmological N-body simulation for the power law ($n = -2$) and LCDM model respectively. The magnitude of exact and approximate corrections are also shown by the dot-dashed and dotted lines (see text for details). All the parameters for both the models are the same as in Figure 5.1.

5.3.3 Destruction rate

Following the same approach as we have applied for the formation rate, we can find the corrections due to finite box size for destruction rate i.e., equation (5.5) also.

$$\left(\frac{dN_{Dest}(M,t)}{dt}\right) dM = \left(\frac{dN_{Dest_0}(M,t)}{dt}\right) dM - \left(\frac{dN_{Dest_1}(M,t)}{dt}\right) dM \tag{5.14}$$

where

$$\left(\frac{dN_{Dest_0}(M,t)}{dt}\right) dM = \sqrt{\frac{2}{\pi}}\frac{\rho_0}{M}\left(\frac{1}{D^2(t)}\frac{dD(t)}{dt}\right)\left(-\frac{\delta_c}{\sigma_0^2(M)}\frac{d\sigma_0(M)}{dt}\right) dM \times \exp\left(-\frac{\delta_c^2}{2\sigma_0^2(M)D^2(t)}\right) \tag{5.15}$$

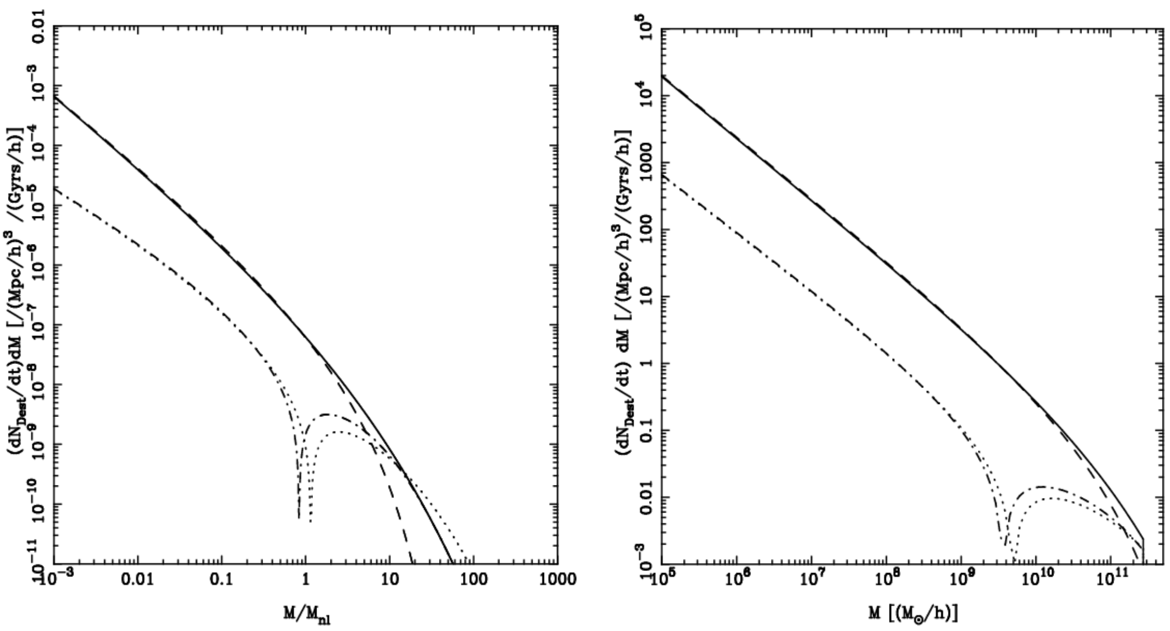

Figure 5.3: The left and right panels of this figure show the theoretical destruction rate i.e., $(dN_{Dest_0}/dt)dM$ (solid line) and the destruction rate $(dN_{Dest}/dt)dM$ (dashed-line) which we expect in cosmological N-body simulation for the power law ($n = -2$) and LCDM model respectively. The magnitude of exact and approximate corrections are also shown by the dot-dashed and dotted line (see text for details). All the parameters for the power law and LCDM models are the same as in Figure 5.1.

and

$$\left(\frac{dN_{Dest_1}(M,t)}{dt}\right)dM = \frac{1}{2}\left[1-\left(1-\frac{\sigma_1^2}{\sigma_0^2}\right)^{-3/2}\left(1-\frac{d\sigma_1^2}{d\sigma_0^2}\right)\right.$$
$$\left.\times\exp\left\{-\frac{\delta_c^2}{2D^2(t)}\left(\frac{1}{\sigma^2}-\frac{1}{\sigma_0^2}\right)\right\}\right]\left(\frac{dN_{Dest_0}(M,t)}{dt}\right) \tag{5.16}$$

or

$$\left(\frac{dN_{Dest_1}(M,t)}{dt}\right)dM \approx \frac{1}{2}\left[\frac{d\sigma_1^2}{d\sigma_0^2}-\frac{3\sigma_1^2}{2\sigma_0^2}+\frac{\delta_c^2\sigma_1^2}{2D^2(t)\sigma_0^4}\right]\left(\frac{dN_{Dest_0}(M,t)}{dt}\right) \tag{5.17}$$

if $\sigma_1^2/\sigma_0^2 < 1$ Figure 5.3 shows the destruction rate of haloes for the power law model (left panel) and the LCDM model. All the parameters and line styles in this figure are the same as in Figure 5.1. In this case the correction term changes sign at the same scale at which the correction term for the comoving number density changes. This is because N_{PS_1}/N_{PS_0} and N_{Dest_1}/N_{Dest_0} are equal and so

$N_{PS,1}$ and N_{Dest_1} have the same scale of zero crossing. Here also we find that the destruction rate for the massive haloes is suppressed. However, it is enhanced for the low mass haloes when we reduce the size of the simulation box.

5.3.4 Rate of change on number density

The number density of haloes in the mass range $[M, M+dM]$ changes mainly due to the formation of haloes of mass M when smaller haloes i.e., haloes with mass $< M$, merge together, and due to destruction of haloes of mass M when larger haloes i.e., haloes with mass $> M$, form. The rate of change of the number density of haloes $(dN_{PS}/dt)dM$ is given by equation (5.2)

$$\begin{aligned}\left(\frac{N_{PS}(M,t)}{dt}\right)dM &= \frac{-1}{D(t)}\frac{dD(t)}{dt}\left[1-\frac{\delta_c^2}{\sigma^2(M)D^2(t)}\right]N_{PS}(M,t)dM \\ &= -\left(\frac{dN_{Dest}(M,t)}{dt}\right)dM+\left(\frac{dN_{Form}(M,t)}{dt}\right)dM \qquad (5.18)\end{aligned}$$

From equation (5.18) it is clear that the rate of change of number density $\dot{N}_{PS}$ is dominated for $\sigma(M) < \delta_c/D(t)$ by the formation rate, and for $\sigma(M) > \delta_c/D(t)$ by the destruction rate. For any time t, we can find a mass scale M_c for which $\sigma(M_c) = \delta_c/D(t)$ i.e., the formation and the destruction rate are equal and so there is no net change in the comoving number density of objects at that scale. In hierarchical clustering models i.e., models in which $\sigma(M)$ is a decreasing function of mass, the comoving number density at large scales mainly changes due to the formation of massive haloes and at small scales due to the destruction of smaller haloes.

The rate of change in the number density is underestimated at large and small scales, but overestimated at intermediate scales. This feature is clear from Figure 5.4 in which the actual and approximate error terms are positive at large and small scales but they are negative at intermediate scales and we have two zeroes crossing.

5.3.5 Merger rate

The formalism which we have developed can be used to find correction in merger rate of haloes also which is generally expressed in the form of conditional probabilities (Lacey & Cole, 1993; Lacey &

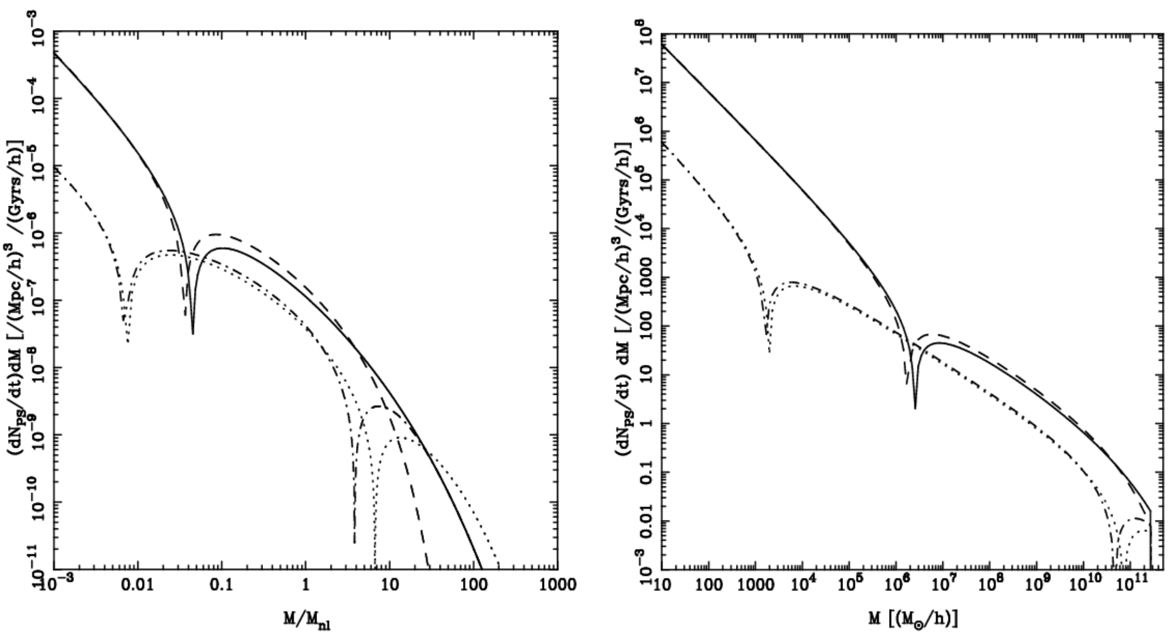

Figure 5.4: The left and right panels of this figure show the theoretical rate of change of comoving number density $(dN_{PS_0}/dt)dM$ (solid line) and the rate of change of comoving number density $(dN_{PS}/dt)dM$ (dashed-line) which we expect in cosmological N-body simulation for the power law ($n = -2$) and LCDM model respectively. The magnitude of exact and approximate corrections are also shown by the dot-dashed and dotted line (see text for details). All the parameters for the power law and LCDM models are the same as in Figure 5.1.

Cole, 1994; Cohn, Bagla & White, 2001).

The conditional probability of a halo which has mass in the range $[M_A, M_A + dM_A]$ at time t_A to become a part of a halo having mass in the range $[M_B, M_B + dM_B]$ at time t_B is given by the following expression

$$\frac{df_A(M_A,\delta_{c_A}|M_B,\delta_{c_B})}{dM_A}dM_A = \frac{1}{\sqrt{2\pi}}\frac{\delta_{c_A}-\delta_{c_B}}{(\sigma_A^2-\sigma_B^2)^{3/2}}\left|\frac{d\sigma_A^2}{dM_A}\right|\exp\left[-\frac{(\delta_{c_A}^2-\delta_{c_B}^2)}{2(\sigma_A^2-\sigma_B^2)}\right]dM_A \qquad (5.19)$$

Note that here haloes with mass M_A and M_B are identified with the regions in the initial density field which have linearly extrapolated density contrasts greater than δ_{c_A} and δ_{c_B} respectively. Here σ_A^2 and σ_B^2 represent the mass variance in the regions which lead to collapse of haloes of mass M_A and M_B at time t_A and t_B respectively.

On the basis of equation (5.19) we can also write an expression for the conditional probability of haloes of mass M_A at time t_A being incorporated in haloes of mass M_B at time t_B.

$$\frac{df_B(M_B,\delta_{c_B}|M_A,\delta_{c_A})}{dM_B}dM_B = \frac{1}{\sqrt{2\pi}}\frac{\delta_{c_B}(\delta_{c_B}-\delta_{c_A})}{\delta_{c_A}}\left[\frac{\sigma_A^2}{\sigma_B^2(\sigma_A^2-\sigma_B^2)}\right]^{3/2}\left|\frac{d\sigma_B^2}{dM_2}\right|$$
$$\times\exp\left[-\frac{(\delta_{c_B}\sigma_1^2-\delta_{c_A}\sigma_B^2)^2}{2\sigma_A^2\sigma_B^2(\sigma_A^2-\sigma_B^2)}\right]dM_B \qquad (5.20)$$

In equation (5.19) and equation (5.20) the only time dependent functions are the linearly extrapolated critical density contrasts δ_{c_A} and δ_{c_B} i.e., $\delta_{c_A}=\delta_c/D(t_A)$ and $\delta_{c_B}=\delta_c/D(t_B)$ where $D(t)$ is the linear growth factor and δ_c is a constant.

In order to find merger the rates, we take the limits $\delta_A \longrightarrow \delta_B$ and $M_A \longrightarrow M_B$. This gives us the following expression for the rate at which haloes of mass M_A are incorporated into haloes of mass M_B at time t_B

$$\frac{df_A(M_A\longrightarrow M_B;t)}{dt}dM_A = \lim_{\Delta t\to 0}\frac{f_A(M_A,t-\Delta t|M_B,t)}{\Delta t}dM_A$$
$$= \sqrt{\frac{1}{2\pi}}\frac{1}{(\sigma_A^2-\sigma_B^2)^{3/2}}\left[-\frac{d\delta_c(t)}{dt}\right]\left|\frac{d\sigma_A^2}{dM_A}\right|dM_A \qquad (5.21)$$

In the same way we can find the rate at which haloes of mass M_B are formed from growth of haloes of mass M_B at time t_B

$$\frac{df_B(M_A\longrightarrow M_B;t)}{dt} = \sqrt{\frac{1}{2\pi}}\left[\frac{\sigma_A^2}{\sigma_B^2(\sigma_A^2-\sigma_B^2)}\right]^{3/2}\left[-\frac{d\delta_c(t)}{dt}\right]\left|\frac{d\sigma_B^2}{dM_B}\right|$$
$$\times\exp\left[-\delta_c^2(t)\left(\frac{1}{2\sigma_B^2}-\frac{1}{2\sigma_A^2}\right)\right] \qquad (5.22)$$

Equation (5.21) and equation (5.22) show that df_A/dt and df_B/dt are related to mass variance σ_A^2 and σ_B^2. With the help of these equations we compute corrections in df_A/dt i.e., df_{A_1}/dt, and df_B/dt i.e., df_{B_1}/dt, in terms of corrections in σ_A^2 i.e., $\sigma_{A_1}^2$, and correction in σ_B^2 i.e., $\sigma_{B_1}^2$, in the following way

$$\frac{df_{A_1}}{dt} = \frac{df_{A_0}}{dt}-\frac{df_A}{dt} = \left[1-\left(1-\frac{\sigma_{A_1}^2-\sigma_{B_1}^2}{\sigma_{A_0}^2-\sigma_{B_0}^2}\right)^{-3/2}\left|\left(1-\frac{d\sigma_{A_1}^2}{d\sigma_{A_0}^2}\right)\right|\right]\frac{df_{A_0}}{dt} \qquad (5.23)$$

where

$$\frac{df_{A_0}}{dt} = \sqrt{\frac{1}{2\pi}}\frac{1}{(\sigma_{A_0}^2-\sigma_{B_0}^2)^{3/2}}\left[-\frac{d\delta_c(t)}{dt}\right]\left|\frac{d\sigma_{A_0}^2}{dM_A}\right|dM_A$$

and

$$\begin{aligned}\frac{df_{B_1}}{dt} &= \frac{df_{B_0}}{dt}-\frac{df_B}{dt}=\left[1-\left(1-\frac{\sigma^2_{A_1}}{\sigma^2_{A_0}}\right)^{3/2}\left(1-\frac{\sigma^2_{B_1}}{\sigma^2_{B_0}}\right)^{-3/2}\left(1-\frac{\sigma^2_{A_1}-\sigma^2_{B_1}}{\sigma^2_{A_0}-\sigma^2_{B_0}}\right)^{-3/2}\left|\left(1-\frac{d\sigma^2_{B_1}}{d\sigma^2_{B_0}}\right)\right|\right.\\ &\quad\left.\times\exp\left\{-\frac{\delta_c^2(t)}{2}\left(\frac{\sigma^2_{B_1}}{\sigma^2_{B_0}(\sigma^2_{B_0}-\sigma^2_{B_1})}-\frac{\sigma^2_{A_1}}{\sigma^2_{A_0}(\sigma^2_{A_0}-\sigma^2_{A_1})}\right)\right\}\right]\frac{df_{B_0}}{dt} \qquad (5.24)\end{aligned}$$

where

$$\frac{df_{B_0}}{dt} = \sqrt{\frac{1}{2\pi}}\left[\frac{\sigma^2_{A_0}}{\sigma^2_{B_0}(\sigma^2_{A_0}-\sigma^2_{B_0})}\right]^{3/2}\left[-\frac{d\delta_c(t)}{dt}\right]\left|\frac{d\sigma^2_{B_0}}{dM_B}\right|\exp\left[-\delta_c^2(t)\left(\frac{1}{2\sigma^2_{B_0}}-\frac{1}{2\sigma^2_{A_0}}\right)\right]$$

These expressions can be used to quantify the effects of a finite simulation box on merger rate.

5.4 Discussion

In the hierarchical clustering models of structure formation, formation and destruction of haloes is a common process. In the present study we have shown that the formation and destruction rate of haloes due to gravitational clustering are affected significantly if the size of the simulation box is not sufficiently large. On the basis of the Press-Schechter formalism we have given the analytic expressions for the corrections in the comoving number density, formation rate, destruction rate and the rate of change in the number density of haloes at a given mass scale. We have considered the implications of our analysis for the power law ($n = -2$) and LCDM models. Since the box corrections are more important for models which have significant power at large scales, most of the models in which there is none or very less power at large scales are not affected by the size of the simulation box. However, for models in which there is a lot of power at large scales (n is large and negative) the box effects can be quite large. In both the cases i.e., power law and LCDM models, the scales at which we have shown the corrections are far below the size of the simulation box.

The main conclusions of the present study are as follows:

- If the size of the simulation box in N-body simulations is not large enough then the clustering amplitude is underestimated at all scales.
- At any given time, there is a scale above which merging is dominated by the formation rate and below which it is dominated by the destruction rate.

- The comoving number density of haloes is underestimated at large scales and overestimated at small scales when we reduce the size of the simulation box.
- The formation and destruction rate also get modified by reducing the size of the simulation box. Particularly, they are underestimated at large scales and overestimated at small scales.
- The suppression of the formation rate as well as destruction rate at large scales is mainly due to the absence of fluctuations in the initial density field at large scales due to limitation of box size.
- In N-body simulations which have small power at large scales the corrections due to box size can be ignored.

Chapter 6

Finite volume effects -III: Skewness

6.1 Introduction

In Chapter 4 we presented a prescription for taking into account the corrections in physical quantities due to finite box size in cosmological N-body simulations. We gave explicit expressions for corrections in mass variance, two point correlation function, mass function and multiplicities. In Chapter 5 we generalized our formalism and gave expressions for corrections in the formation and destruction rate of haloes as well as for merger rates. In the present chapter we extend our formalism and study the effect of a finite box size on Skewness and higher moments in the weakly nonlinear regime. We also test our theoretical predictions with a set of cosmological N-body simulations. In most cases we find good agreement between our theoretical estimates and N-body simulations. The main results of the present study have been published in (Bagla, Prasad & Khandai, 2008).

In §6.2 we review our prescription for estimating the corrections in physical quantities due to finite box size and give expressions for corrections in Skewness S_3 and Kurtosis S_4 due to finite box size in cosmological N-body simulations. In §6.3 we present the results of our N-body simulations. We compare the theoretical estimates of two point correlation function, Skewness and number density of haloes with N-body simulations. We find that in most cases there is a good agreement between the theoretical estimates and N-body simulations. We also study the effects of finite box size on relative pair velocity statistics and nonlinear scaling relations. We summarize the main results of our study in §6.4 and conclude.

6.2 Reduced Moments

In Chapter 4 we showed that the amplitude of clustering i.e., mass variance, is underestimated at all scales when the size of the simulation box is finite. We showed that the mass variance $\sigma^2(r, L_{box})$ in simulations is related to the theoretical mass variance $\sigma_0^2(r)$ in the following way (see §4.2 for detail):

$$\sigma^2(r, L_{\rm box}) = \sigma_0^2(r) - \sigma_1^2(r, L_{\rm box}) \tag{6.1}$$

here $\sigma_1^2(r, L_{box})$ is the correction due to a finite box size. At large scales $\sigma_0^2(r)$ and $\sigma_1^2(r, L_{box})$ have a similar magnitude and the rms fluctuations in simulations become negligible compared to the expected values in the model. As we approach small r the correction term $\sigma_1^2(r, L_{box})$ is constant and for most models it becomes insignificant in comparison to $\sigma_0^2(r)$. In models where $\sigma_0^2(r)$ increases very slowly at small scales or saturates to a constant value, the correction term σ_1^2 can be significant at all scales.

In a weakly nonlinear regime, reduced moments like Skewness S_3 and Kurtosis S_4 can be computed analytically using perturbative methods (Bernardeau, 1994). The expected values of reduced moments are directly related to the slope of the initial or linearly extrapolated $\sigma^2(r)$. We can use the corrections in clustering amplitude $\sigma^2(r)$ for estimating corrections in reduced moments S_3 and S_4 in the weakly nonlinear regime.

$$S_3 = \frac{34}{7} + \frac{\partial \ln \sigma^2}{\partial \ln r} \tag{6.2}$$

from equation (6.1) and equation (6.2)

$$\begin{aligned} S_3 &= \frac{34}{7} + \frac{\partial \ln\left(\sigma_0^2 - \sigma_1^2\right)}{\partial \ln r} \\ &= \frac{34}{7} + \frac{\partial \ln \sigma_0^2}{\partial \ln r} + \frac{\partial \ln\left(1 - \sigma_1^2/\sigma_0^2\right)}{\partial \ln r} \\ &= S_{3_0} - S_{3_1} \end{aligned} \tag{6.3}$$

Here S_{3_0} is the expected value of S_3 for the given mode, i.e., when there are no box corrections and S_{3_1} is the correction term in S_3 due to a finite box size.

In general we expect that σ_1^2/σ_0^2 increases as we go to larger scales. Thus the Skewness is underestimated in N-Body simulations and the level of underestimation depends on the slope of σ_1^2/σ_0^2 as compared to the slope of σ_0^2. In the limit of small scales where σ_1^2 is almost independent of scale, we find that the correction is:

$$\begin{aligned} S_3 &= \frac{34}{7} + \frac{\partial \ln \sigma_0^2}{\partial \ln r} + \frac{\partial \ln \left(1 - \sigma_1^2/\sigma_0^2\right)}{\partial \ln r} \\ &\simeq \frac{34}{7} - (n+3) - \frac{\partial \left(\sigma_1^2/\sigma_0^2\right)}{\partial \ln r} + O\left(\frac{\partial}{\partial \ln r}\left(\frac{\sigma_1^2}{\sigma_0^2}\right)^2\right) \\ &\simeq \frac{34}{7} - (n+3)\left[1 + \frac{\sigma_1^2}{\sigma_0^2}\right] + O\left(\frac{\partial}{\partial \ln r}\left(\frac{\sigma_1^2}{\sigma_0^2}\right)^2\right) + O\left(\frac{1}{\sigma_0^2}\frac{\partial \sigma_1^2}{\partial \ln r}\right) \end{aligned} \tag{6.4}$$

Here n is the index of the initial power spectrum we are simulating. For non-power law models this will also be a function of scale. The correction becomes more significant at larger scales and the net effect, as noted above, is to underestimate S_3.

Box size effects lead to a change in slope of σ^2, and hence the effective value of n changes. The last term in equation (6.3) is the leading order offset in Skewness in N-Body simulations as compared with the expected values in the model being simulated. We would like to emphasize that this expression is valid only in the weakly nonlinear regime.

Similar expressions can be written down for Kurtosis and other reduced moments using the approach outlined above. We give the expression for Kurtosis below, but do not compute further moments as the same general principle can be used to compute these as well.

$$\begin{aligned} S_4 &= \frac{6071}{1323} + \frac{62}{3}\frac{\partial \ln \sigma^2}{\partial \ln r} + \frac{7}{3}\left[\frac{\partial \ln \sigma^2}{\partial \ln r}\right]^2 + 2\frac{\partial^2 \ln \sigma^2}{\partial \ln^2 r} \\ &\simeq \frac{6071}{1323} - \frac{62}{3}(n+3)\left[1 + \frac{\sigma_1^2}{\sigma_0^2}\right] + \frac{7}{3}(n+3)^2\left[1 - \frac{8}{7}\frac{\sigma_1^2}{\sigma_0^2}\right] + O\left(\frac{\partial}{\partial \ln r}\left(\frac{\sigma_1^2}{\sigma_0^2}\right)^2\right) + O\left(\frac{1}{\sigma_0^2}\frac{\partial \sigma_1^2}{\partial \ln r}\right) \end{aligned}$$

6.3 N- body simulations

In order to study the effects of the size of the simulation box on physical quantiles we have carried out a set of N-body simulations. Details of simulations are given in Table 6.1.

We compare the analytical estimates for finite box size effects for various quantities with N-Body simulations. Such a comparison is relevant in order to test the effectiveness of approximations made

Model	Spectral Index	Cut Off (k_c)
A1	-2.0	k_f
A2	-2.0	$2k_f$
A3	-2.0	$4k_f$
B1	-2.5	k_f
B2	-2.5	$2k_f$
B3	-2.5	$4k_f$

Table 6.1: This table lists characteristics of N-Body simulations used in our study. Here the spectral index gives the slope of the initial power spectrum and the cutoff refers to the wave number below which all perturbations are set to zero: $k_f = 2\pi/L_{box}$ is the fundamental wave mode for the simulation box. All models were simulated using the TreePM code. 8×10^6 particles were used in each simulation, and the PM calculations were done on a 200^3 grid. Power spectra for both the A and the B series of simulations were normalized to ensure $\sigma = 1$ at the scale of 8 grid lengths at the final epoch if there is no box-size cutoff. A softening length of 0.5 grid lengths was used as the evolution of small scale features is not of interest in the present study.

in computing the effects of a finite box size. We have made the approximation that the effects of mode coupling between the scales that are taken into account in a simulation and the modes corresponding to scales larger than the simulation box are ignored. We believe that this should not be important unless the initial power spectrum has a sharp feature at scales comparable with the simulation size.

In order to simulate the effects of a finite box size, we used the method employed by (Bagla & Ray, 2005) where initial perturbations are set to zero for all modes with wave number smaller than a given cutoff. For a finite simulation box, there is a natural cutoff at the fundamental wave number $k_f = 2\pi/L_{box}$ and simulations A1 and B1 impose no other cutoff. Simulations A2 and B2 sample perturbations at wave numbers larger than $2k_f$ whereas simulations A3 and B3 are more restrictive with non-zero perturbations up to $4k_f$. The cutoff of $2k_f$ and $4k_f$ in this case corresponds to scales of 100 and 50 grid lengths, respectively.

We have chosen to work with models where box size effects are likely to be significant, particularly with the larger cutoff in wave number. This has been done to test our analytical model in a severe situation, and to illustrate the difficulties in simulating models with large negative indices.

We begin with a visual representation of the simulations. Figure 6.1 shows slices from simulations A1, A2 and A3 respectively at the earlier (left column) and later epoch. Corresponding plots for model B1, B2 and B3 are shown in Figure 6.2. We identify the early and later epochs with the epochs when the scale of nonlinearity in the model without a cutoff is 2 and 8 grid lengths respectively. The relevance of box size effects is apparent as the large scale structure in the three simulations is very different even at the early epoch when $r_{nl} = 2$, much smaller than the effective box size for these simulations. Disagreement between different simulations becomes even more severe as we go to the later epoch with $r_{nl} = 8$ grid lengths.

Visual appearance for simulations B1, B2 and B3, shown in Figure 6.2 follows the same pattern as of simulations A1, A2 and A3 (Figure 6.1) . In this case the spectral index is closer to -3 than for simulations of the A series shown in Figure 6.1, hence the larger scale modes are more important for evolution of perturbations even at small scales. It is interesting to note that the largest under-dense region in simulation B1 at early times is already comparable to the box size and hence we require $L_{\rm box}/r_{nl} \gg 100$ for the effects of a finite box-size to be small enough to be ignored for simulations

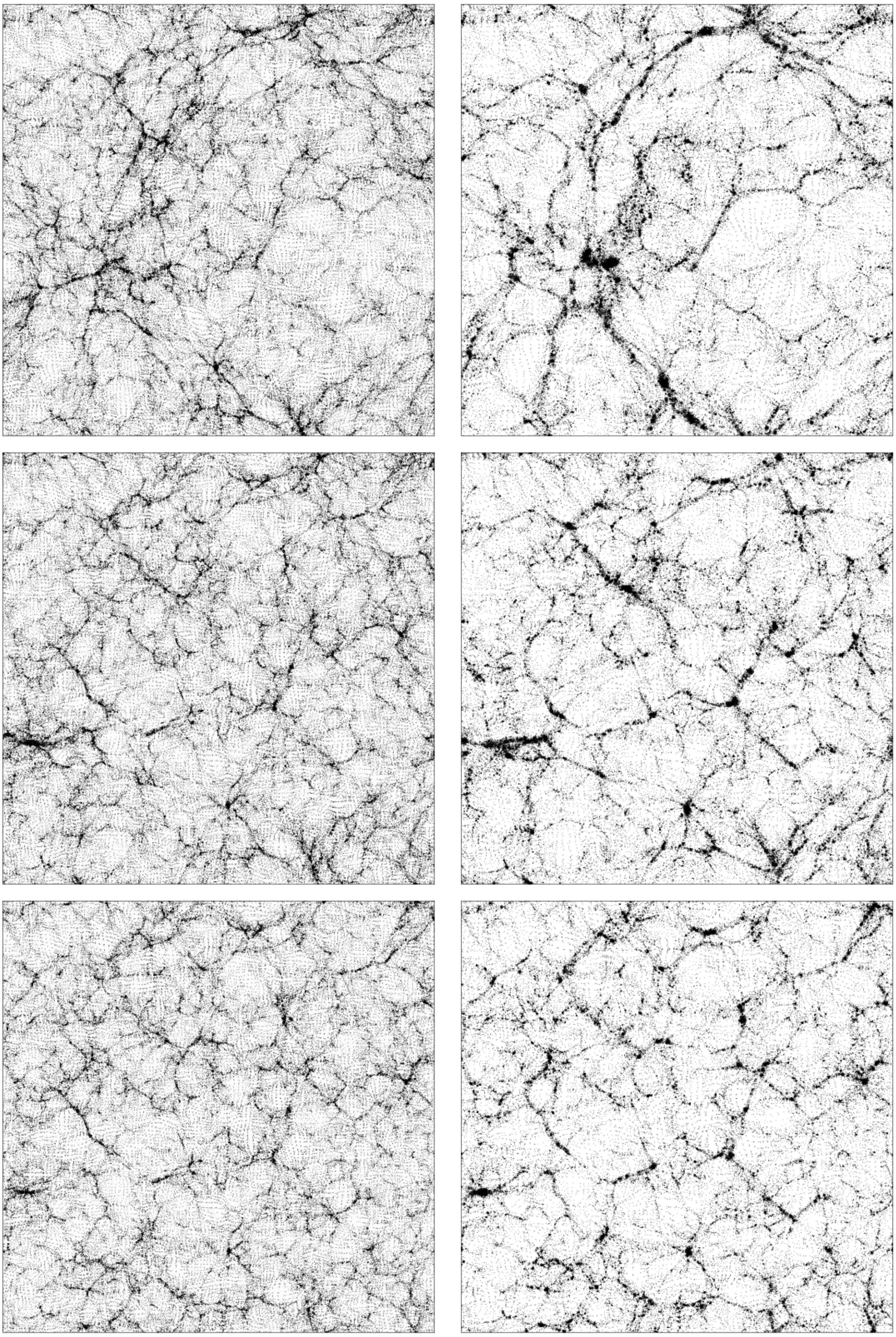

Figure 6.1: The first, second and the third row in this figure show the slices for models A1, A2 and A3 (see table for details) respectively at an early epoch when the scale of nonlinearity is 2 grid lengths (left column) and a later epoch when the scale of nonlinearity is 8 grid lengths (right column).

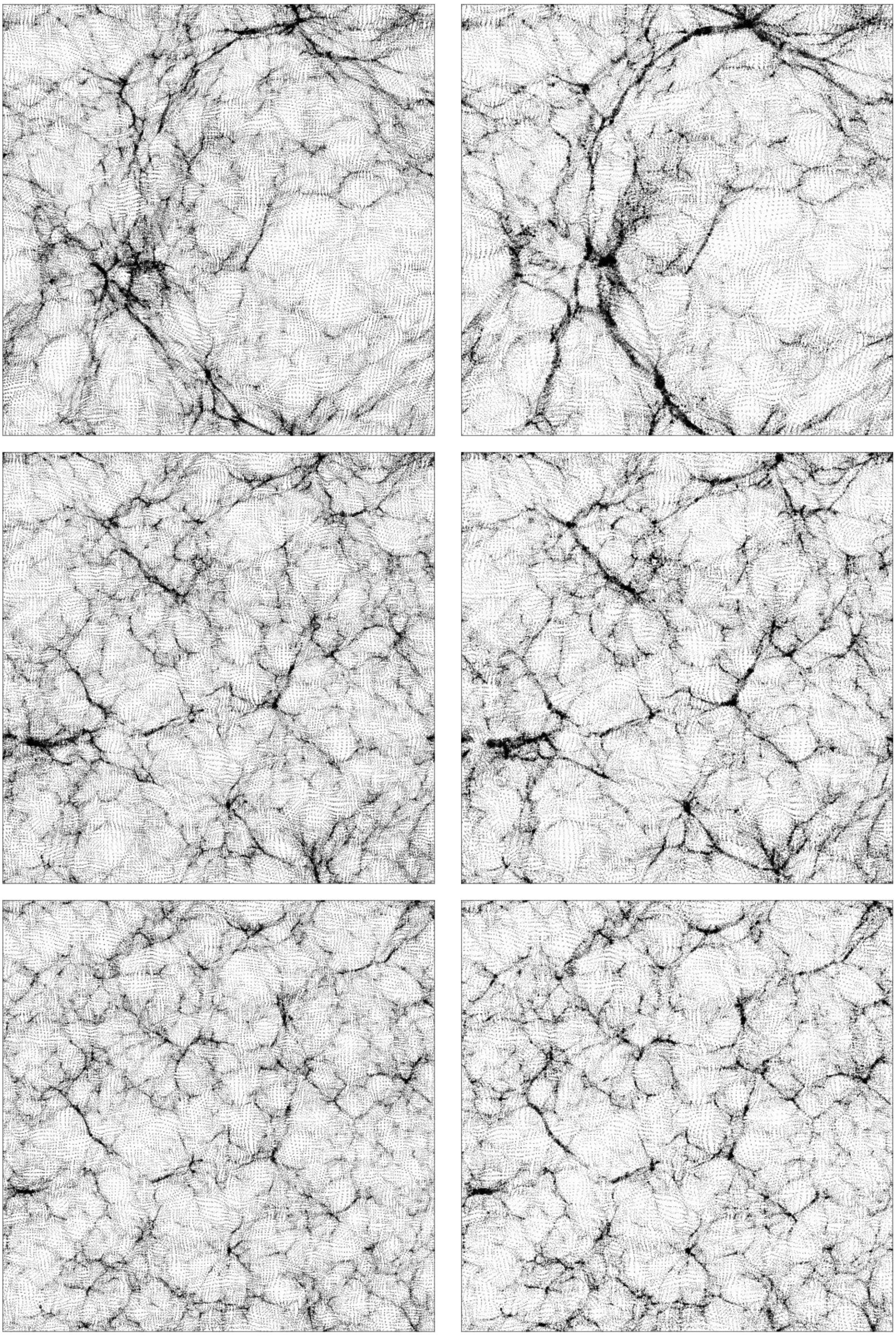

Figure 6.2: The first, second and the third row in this figure show the slices for models B1, B2 and B3 (see table for details) respectively at an early epoch when the scale of nonlinearity is 2 grid lengths (left column) and a later epoch when the scale of nonlinearity is 8 grid lengths (right column).

of the power law model with $n = -2.5$. This constraint is even stronger for models with the slope of the power spectrum closer to $n = -3$.

6.3.1 Clustering amplitude

The top and bottom panels in Figure 6.3 show the averaged correlation function $\bar{\xi}$ for the A and B series models respectively at the early (left column) and later epoch (right column). We have shown $\bar{\xi}$ as a function of scale in these panels. Also shown are the linearly extrapolated values of $\bar{\xi}$ computed using our formalism for estimating the effects of a finite box-size. Data from N-Body simulations is shown as thick curves whereas the theoretical estimates are shown as thin curves with the corresponding line style. It is clear that the analytical estimate for $\bar{\xi}$ in a finite box captures the qualitative nature of the change from the expected values, even though the analytical estimate is linearly extrapolated whereas we are comparing it with results from an N-Body simulation. This is the main reason for disagreement between two curves at small scales where we expect departures from linear theory. Our analysis works better for the $n = -2$ model used in the A series of simulations as compared to the B series of simulations for the $n = -2.5$ model where it systematically underestimates the suppression of $\bar{\xi}$.

6.3.2 Skewness

The top and bottom panels in Figure 6.4 show Skewness S_3 for the A and B series models respectively at the early (left column) and later epoch (right column). Apart from the curves that show S_3 from simulations (thick curves) and our analytical estimate for the weakly nonlinear regime (thin curves), we also show the value of S_3 expected in the weakly nonlinear regime in absence of any finite box size effects by the dotted horizontal line. The analytical estimate of S_3, computed using equation (6.2) matches well with the values in N-Body simulation at the relevant scales. It is noteworthy that the match between the two is better for a larger cutoff in wave numbers. We believe that this is due to sparse sampling of the initial power spectrum at scales comparable to the box size and due to this our approximation of the sum over wave modes by an integral is not very good. This becomes particularly severe if some of these modes take on exceptional values, far away from the typical

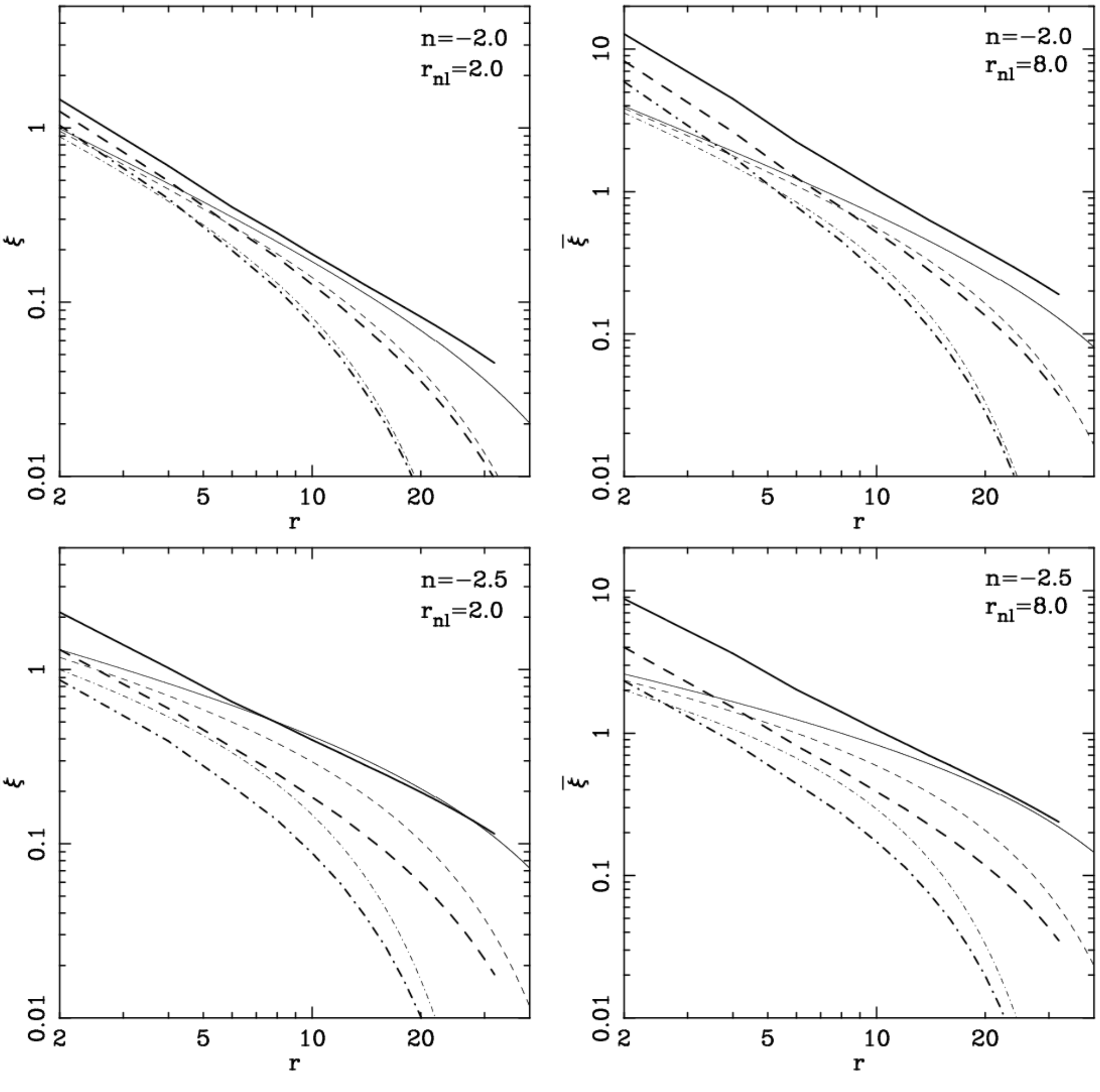

Figure 6.3: The first and second row in this figure show the average two point correlation function for models A1, A2, A3 and B1, B2, B3 respectively at the early epoch (left column) and later epoch epoch (right column). In all the panels models with $k_c = k_f$ (A1 and B1), $k_c = 2k_f$ (A2 and B2) and $k_c = 4k_f$ (A3 and B3) are represented by the solid, dashed and dot-dashed lines. The thick and thin lines represent the physical quantities in simulations and their linearly extrapolated values.

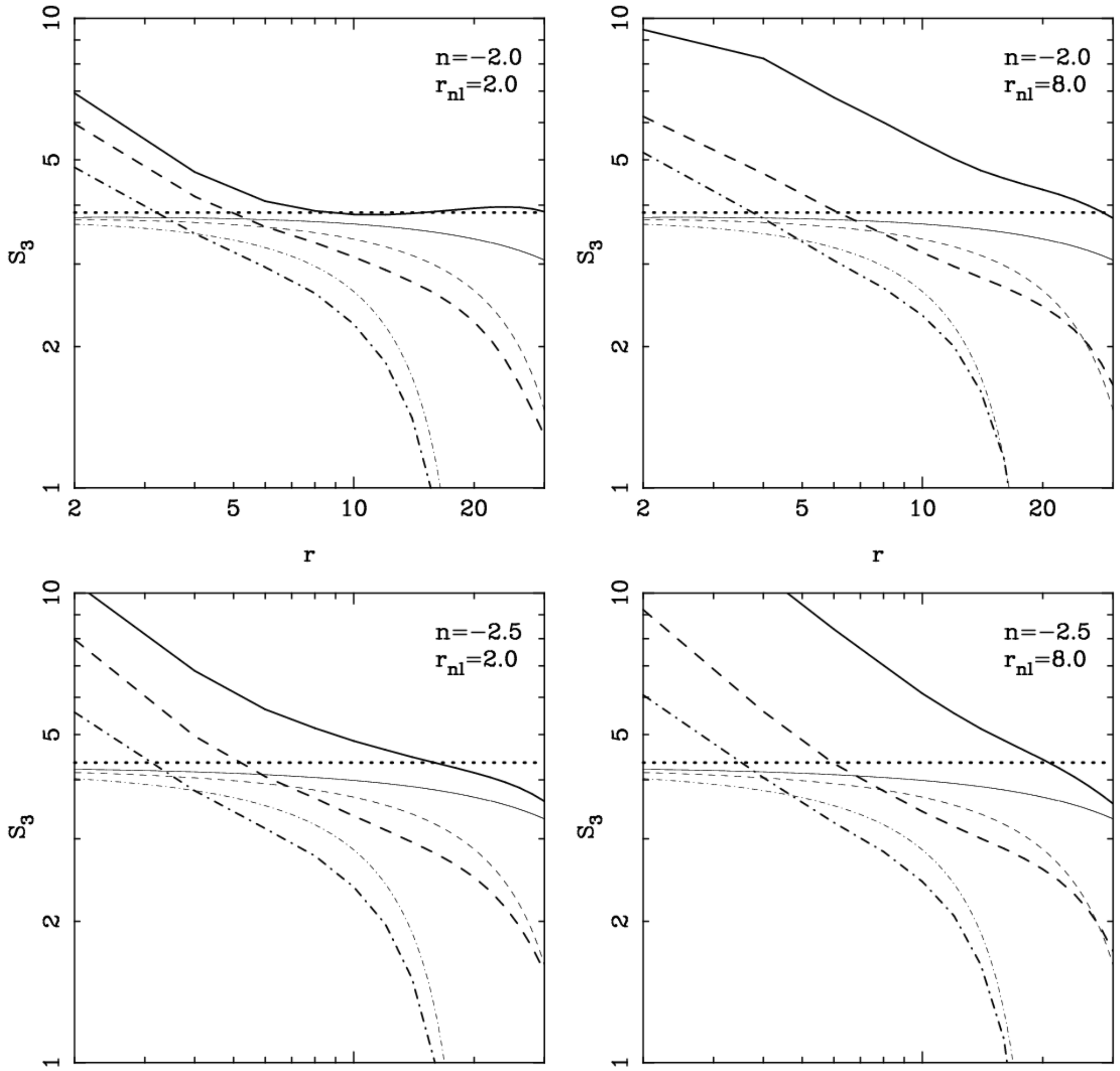

Figure 6.4: The first and second row in this figure show Skewness S_3 for models A1, A2, A3 and B1, B2, B3 respectively at the early (left column) and later epoch (right column). In all the panels models with $k_c = k_f$ (A1 and B1), $k_c = 2k_f$ (A2 and B2) and $k_c = 4k_f$ (A3 and B3) are represented by the solid, dashed and dot-dashed line styles. The thick and thin curves in all the panels represent the physical quantities in simulations and their linearly extrapolated values. We also show the values of S_3 when there are no box size effects by the dotted line.

value.

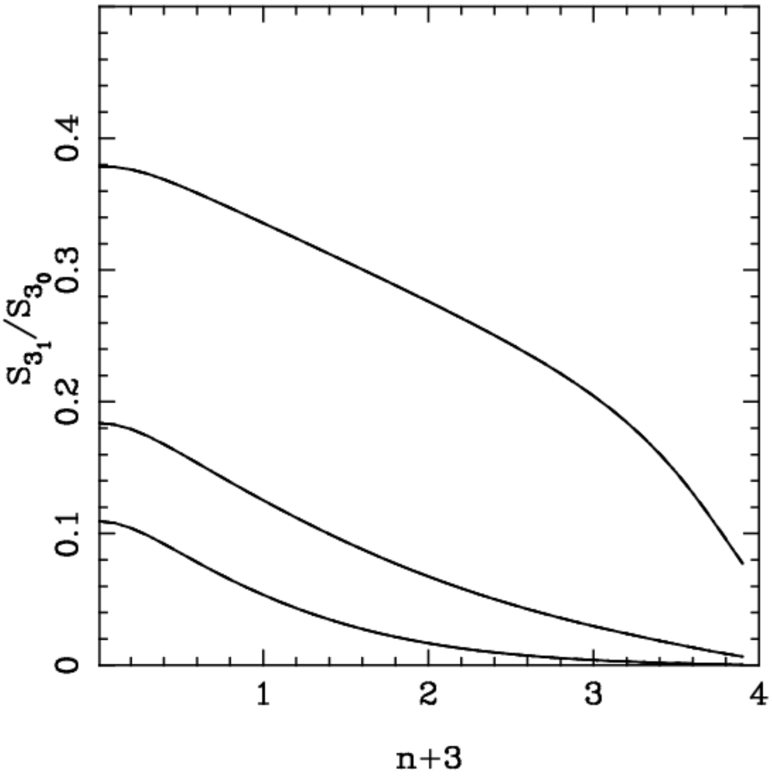

Figure 6.5: This figure shows the theoretical estimates of corrections in S_3 as a function of the index of power spectrum at scales $L_{box}/5$ (top line), $L_{box}/10$ (middle line) and $L_{box}/20$ (bottom line). For a given tolerance of the error in S_3 due to finite box effects, this gives us the largest scale at which the simulation may be expected to give reliable results.

We argue that it is desirable that in N-Body simulations the intended model is reproduced at all scales between the resolution of the simulation and a fairly large fraction of the simulation box. The outer scale up to which the model can be reproduced fixes the effective dynamical range of simulations. It is desirable that S_3 be within a stated tolerance of the expected value at this scale. In Figure 6.5 we plot S_{3_1}/S_{3_0} for power law models at the scale $L_{\rm box}/20$, $L_{\rm box}/10$ and $L_{\rm box}/5$. These are plotted as a function of the spectral index n. It can be shown that this ratio, as also σ_1/σ_0 are functions of scale only through the ratio $r/L_{\rm box}$. We find that S_{3_1}/S_{3_0} is large for large negative n and decreases monotonically as n increases. This ratio is smaller than 10% only for $n \geq 0.8$ at

$r = L_{\rm box}/5$. The corresponding number for $r = L_{\rm box}/10$ is $n \geq -1.6$. Clearly, the effective dynamic range decreases rapidly as $n+3 \longrightarrow 0$. This highlights the difficulties associated with simulating such models.

6.3.3 Mass function

The top and bottom panels in Figure 6.6 show the number density of haloes $N(M)dM$ for the A and B series models respectively at the early (left column) and later epoch (right column). In order to compute the number density haloes have been identified using the Friends of Friends (FOF) method with a linking length of 0.2 in units of the grid length. Plotted in the same panels are the expected values computed using the Press-Schechter mass function with a correction for the finite box size. Here the threshold density contrast δ_c was chosen to ensure a good match between the theoretical prediction and the curves from the A1 simulation at the early epoch. We used $\delta_c = 1.15$ from these considerations.

We find that the qualitative features of the mass function are reproduced correctly by the analytical approximation, namely:

- The number density of the most massive haloes declines rapidly as the *effective* box size is reduced.
- The number density of low mass haloes increases as the *effective* box size is reduced.

However, at a quantitative level there are two discrepancies.

- The mass scale where the number density of haloes begins to fall off is not computed correctly in our formalism.
- The magnitude of over estimation of the number density of low mass haloes is much larger in the analytical calculation as compared to the variation seen in simulations. The softening length used here is more than twice the linking length and this may be partially responsible for this mismatch.

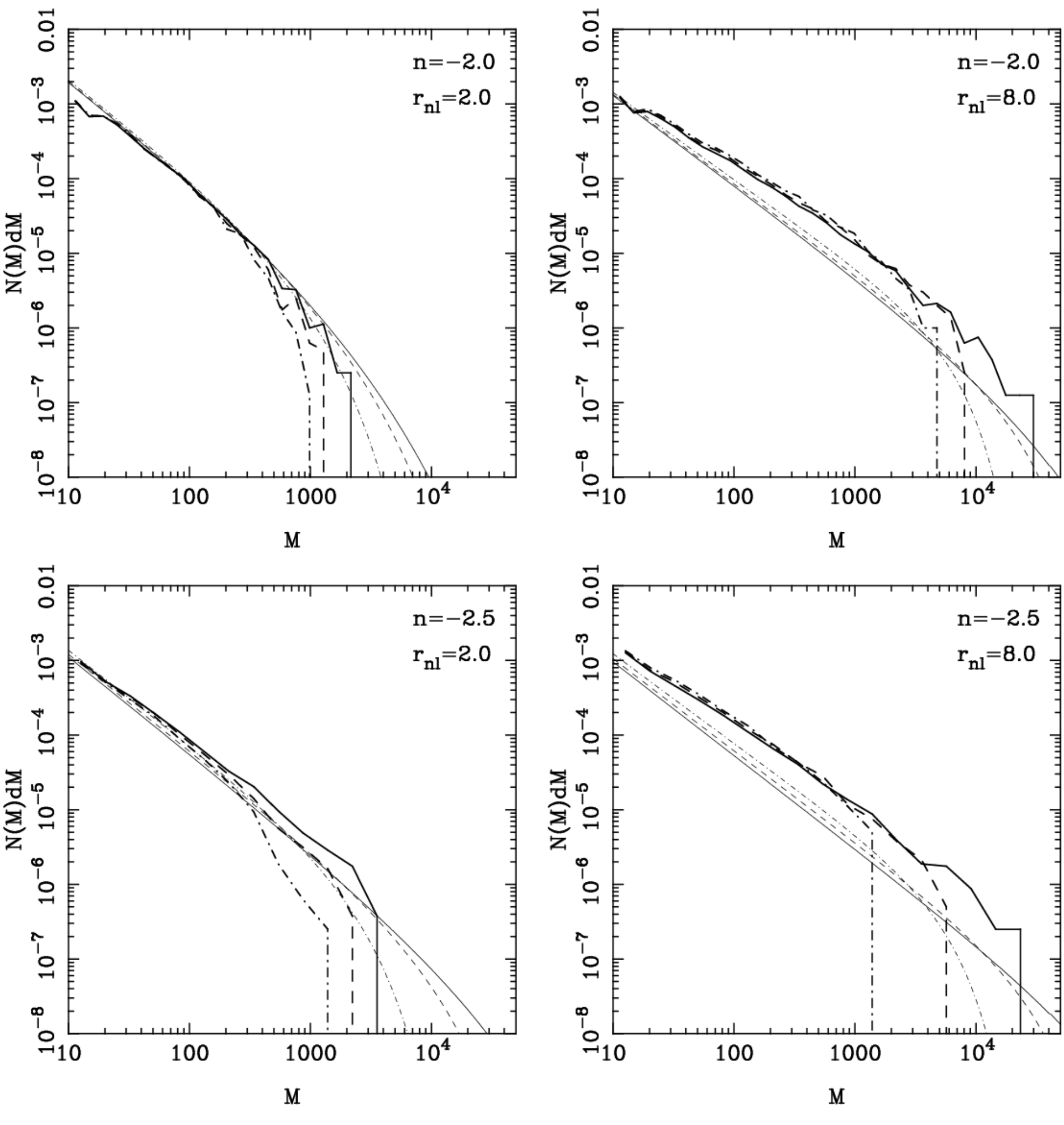

Figure 6.6: The first and second row in this figure show the number density of haloes $N(M)dM$ for models A1, A2, A3 and B1, B2, B3 respectively the early (left column) and later epoch (right column). In all the panels models with $k_c = k_f$ (A1 and B1), $k_c = 2k_f$ (A2 and B2) and $k_c = 4k_f$ (A3 and B3) are represented by the solid, dashed and dot-dashed lines. The thick and thin lines in all the panels represent the physical quantities in simulations and their linearly extrapolated values.

6.3.4 Pair velocity

In our discussion of analytical estimates of the effects of a finite box size on observable quantities, we have so far omitted any discussion of velocity statistics. The main reason for this is that the power spectrum for velocity is different as compared to the power spectrum for density and one can get divergences for quantities analogous to the second order estimators analogous to σ^2 for models with $-3 < n \leq -1$. This is due to a more significant contribution of long wave modes to the velocity field than is the case for density. It is, however, worthwhile to test whether relative velocity statistics are affected by this or not. It is also important to check whether considerations related to velocity statistics put a stronger constraint on the box size required for simulations of a given model.

We measure the radial pair velocity and also the pair velocity dispersion in the simulations used in this work. These quantities are defined as follows:

$$h(r) = -\frac{\langle (\mathbf{v}_j - \mathbf{v}_i) \,.\, (\mathbf{r}_j - \mathbf{r}_i) \rangle}{aHr_{ij}^2} \tag{6.5}$$

where the averaging is done over all pairs of particles with separation $r_{ij} = \left| (\mathbf{r}_j - \mathbf{r}_i) \right| = r$. In practice this is done in a narrow bin in r. Here a is the scale factor, H is the Hubble parameter and $\mathbf{v}_i$ is the velocity of the ith particle. Similarly, the relative pair velocity dispersion is defined as:

$$\sigma_v^2(r) = \frac{\langle |\mathbf{v}_{ij}|^2 \rangle}{a^2H^2r_{ij}^2} \tag{6.6}$$

where $\mathbf{v}_{ij}$ is the relative velocity for a pair of particles, and averaging is done over pairs with separation r.

In the top panels of Figure 6.7 we plot the pair velocity as function of distance at the early (left panel) and later epoch (right panel) for models A1, A2 and A3. Identical quantities for B series models are being plotted in top panels of Figure 6.8. In each panel, we find that the dependence of pair velocity on r is very sensitive to the small k cutoff used in generating the initial conditions for the simulation. It has been known for some time (Hamilton et al., 1991; Nityananda & Padmanabhan, 1994) that the pair velocity is an almost universal function of $\bar{\xi}$. This is certainly true in the linear regime where $h = 2\bar{\xi}/3$ for clustering in an Einstein-de Sitter universe (Peebles, 1980). In order to exploit this aspect, and also to check whether the relation between h and $\bar{\xi}$ in the weakly nonlinear

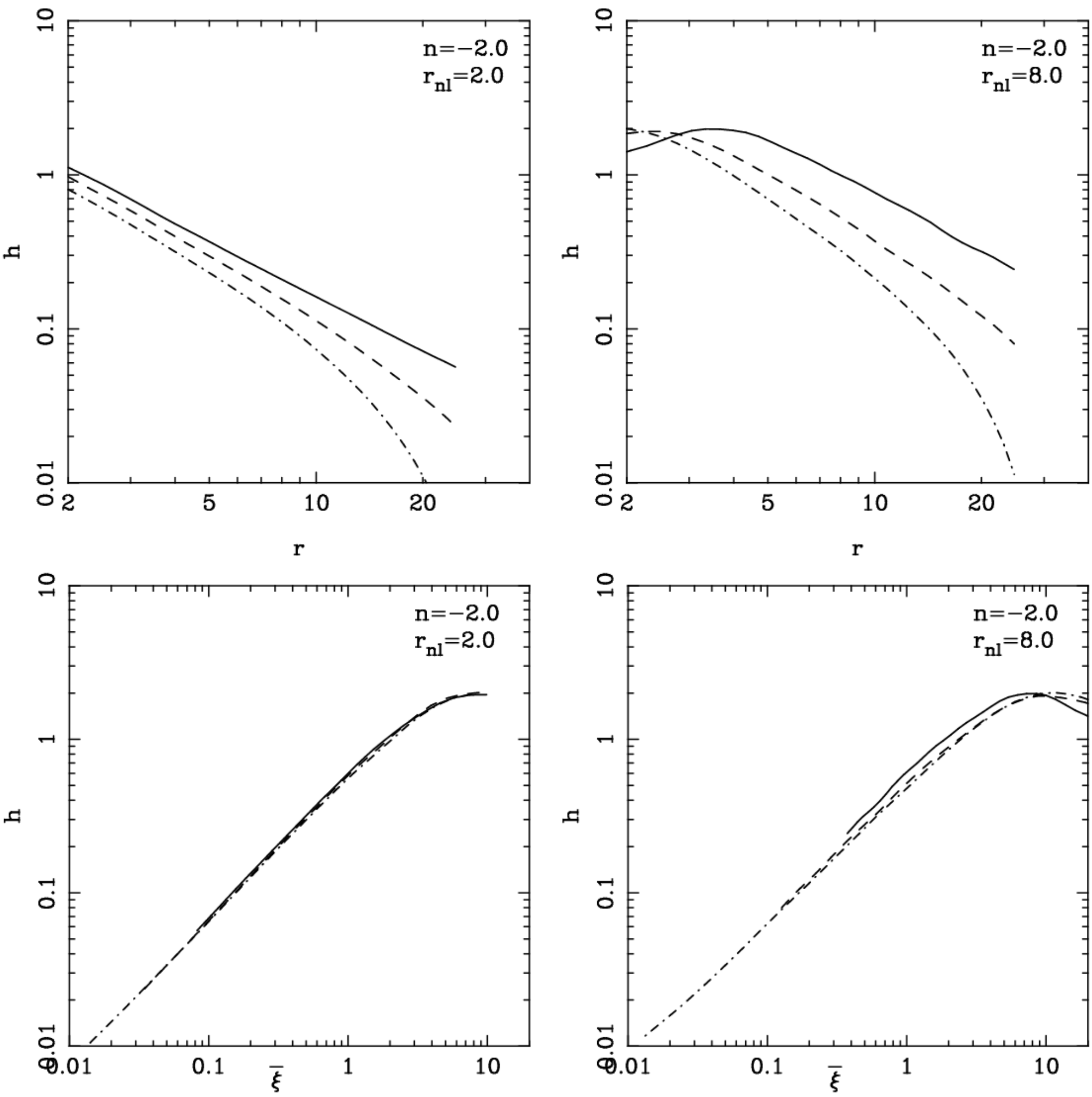

Figure 6.7: The top and bottom rows in the figure show the average pair velocity h (see text for definition) as function of distance and two point correlation function respectively for models A1, A2 and A3 at the early (left column) and later epoch (right column). In this figure also the same line styles are used for various models as are used in the previous figures.

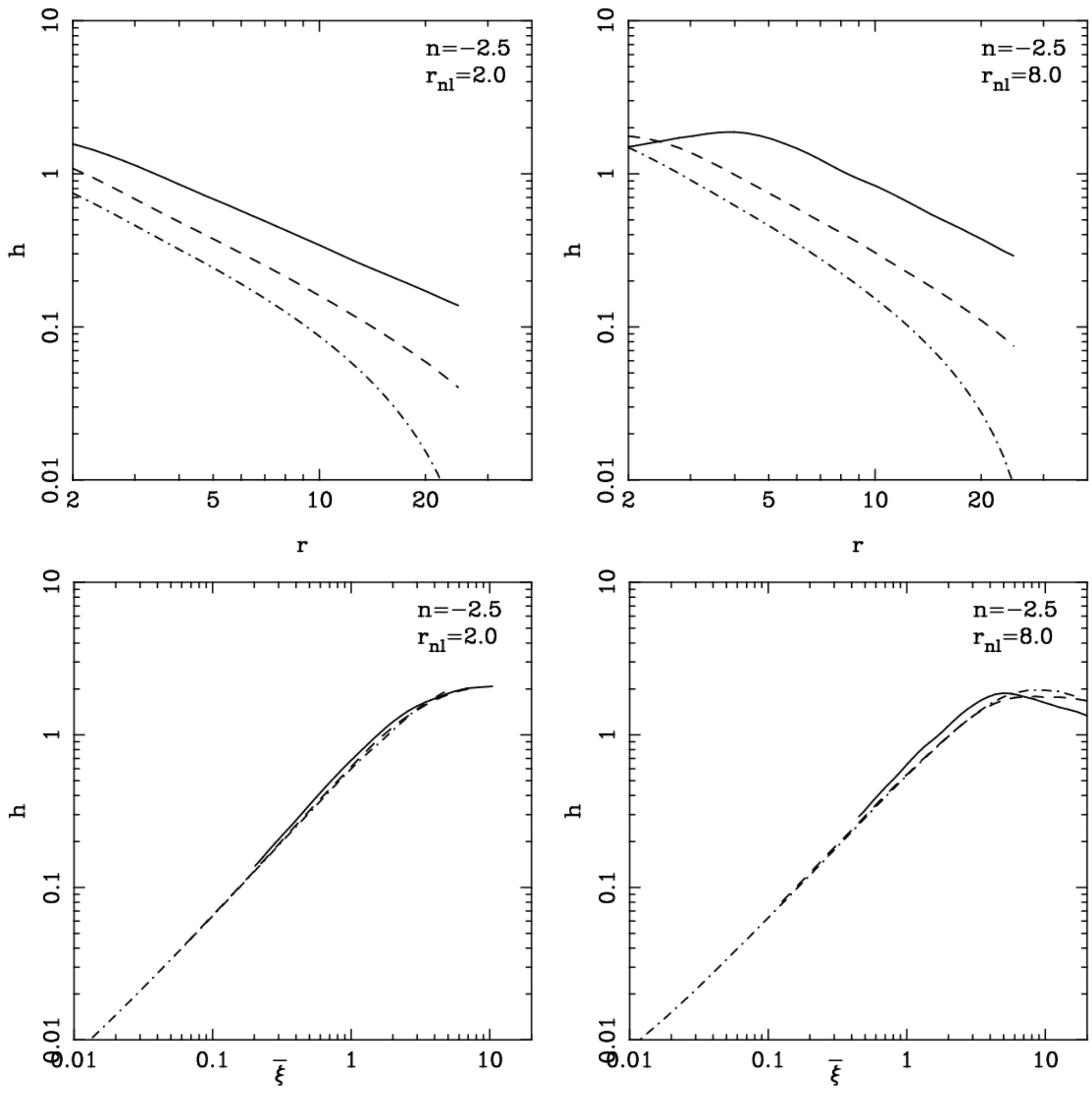

Figure 6.8: The top and bottom rows in the figure show the average pair velocity h (see text for definition) as function of distance and two point correlation function respectively for models B1, B2 and B3 at the early (left column) and the later epoch (right column). In this figure also the same line styles are used for various models as are used in the previous figures.

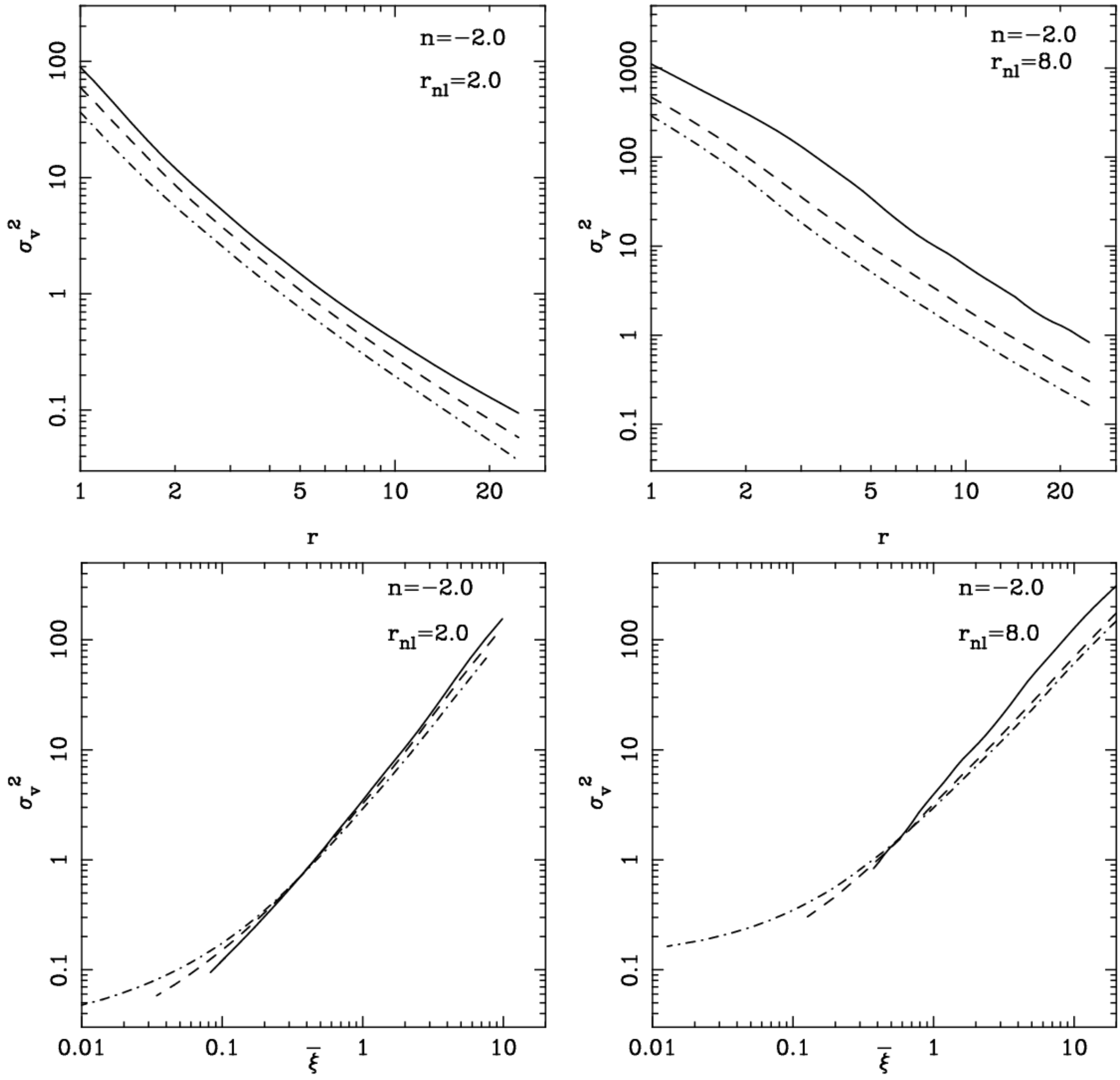

Figure 6.9: The top and bottom rows in the figure show the velocity dispersion σ_v (see text for definition) as function of distance and the average two point correlation function respectively, for models A1, A2 and A3 at the early (left column) and later epoch (right column). In this figure also the same line styles are used for various models as are used in the previous figures.

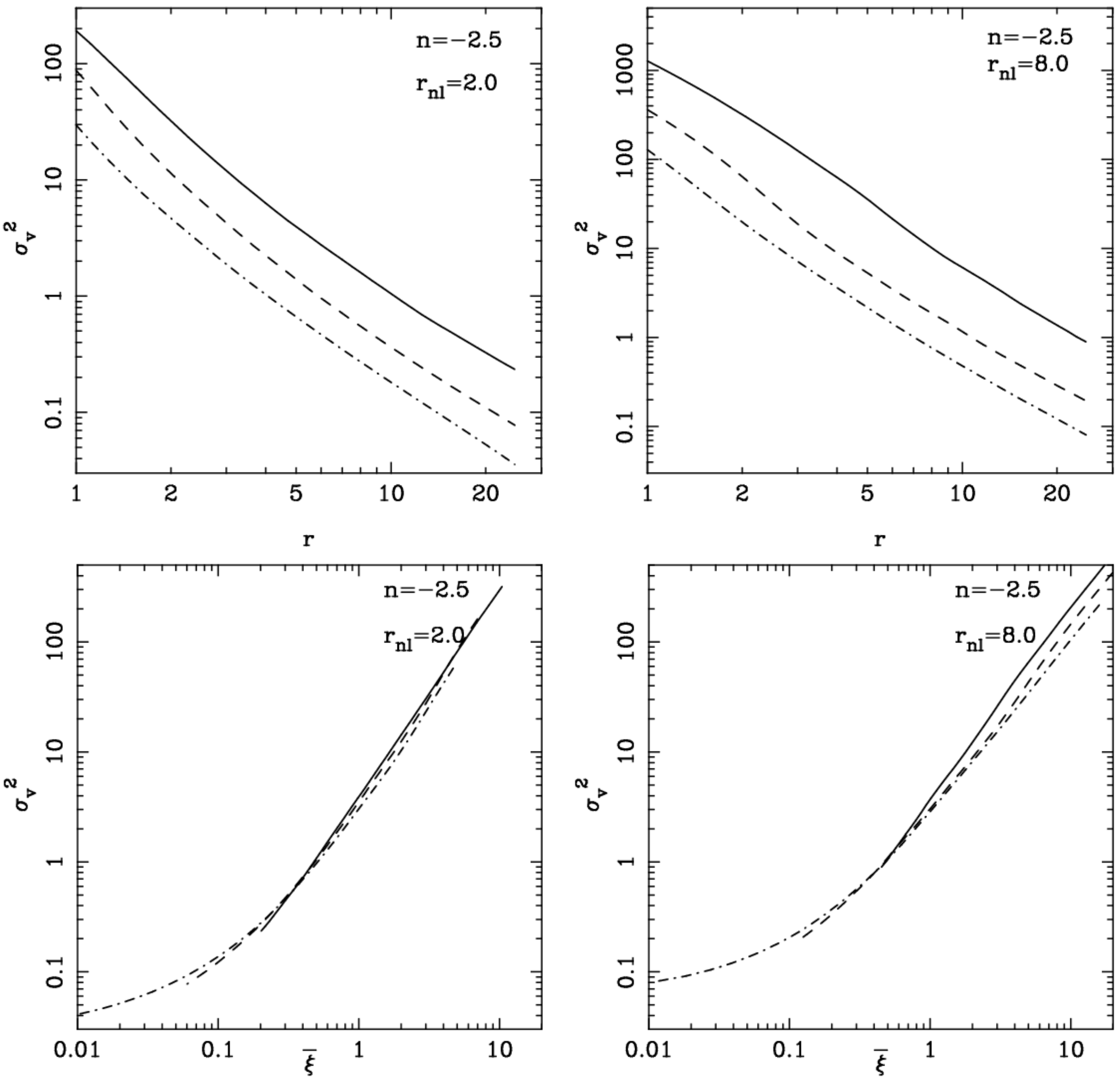

Figure 6.10: The top and bottom rows in the figure show the velocity dispersion σ_v (see text for definition) as function of distance and the average two point correlation function respectively, for models B1, B2 and B3 at the early (left column) and later epoch (right column). In this figure also the same line styles are used for various models as are used in the previous figures.

regime is sensitive to the box size we plot h as a function of $\bar{\xi}$ at the same scale in the bottom panels of Figure 6.7 at early (left column) and later epoch (right column). Identical quantities for B series models are being plotted in bottom panels of Figure 6.8. We find that all the models fall along the same line in this case and variations induced by the finite box size are small even in the weakly non-linear regime.

The top and bottom panels of Figure 6.9 show the relative velocity dispersion as a function of scale and the average two point correlation function $\bar{\xi}$ respectively at the early (left panel) and later epoch (right panel). Again, we find that although the relative pair velocity dispersion at a given scale is sensitive to the size of the simulation box, it remains an almost time independent function of $\bar{\xi}$ for a given model. Thus we can use estimates of the correction in $\bar{\xi}$ to get an estimate of corrections in pair velocity statistics. Identical quantities for B series models are being plotted in bottom panels of Figure 6.10.

6.3.5 Nonlinear scaling relations

We have outlined the method for estimating the initial/linearly extrapolated *rms* amplitude of density perturbations in N-Body simulations. The same approach can be used to estimate other measures of the amplitude of perturbations, e.g., the averaged two point correlation function $\bar{\xi}$ (Bagla & Prasad, 2006). Given that the radial component of pair velocity is an almost universal function of $\bar{\xi}$, as seen in Figure 6.7 and Figure 6.8, we can use scaling relations (Hamilton et al., 1991; Peacock & Dodds, 1994; Nityananda & Padmanabhan, 1994; Jain, Mo & White , 1995; Peacock & Dodds, 1996; Smith et al., 2003) to compute the nonlinear $\bar{\xi}$ from the linearly extrapolated estimate. There is one subtle issue here, namely, many of the scaling relations are written in terms of the power spectrum and this is realized correctly in N-Body simulations. Therefore we are limited to those variants of scaling relations that take the shape of the linearly extrapolated correlation function into account (Hamilton et al., 1991; Smith et al., 2003). We choose to work with (Hamilton et al., 1991) for the purpose of illustration as the scaling relation here is specified purely in terms of $\bar{\xi}$ and suits our purpose better.

The scaling relation due to (Hamilton et al., 1991) can be written as:

$$\bar{\xi}(a,r) = \frac{y + 0.358y^3 + 0.0236y^6}{1 + 0.0134y^3 + 0.00202y^{9/2}} \tag{6.7}$$

where $y = \bar{\xi}_L(a,l)$ is the linearly evolved $\bar{\xi}$ at scale l. Scales l and r are related as $l^3 = r^3(1+\bar{\xi}(r))$. This scaling relation is likely to be a poor approximation, particularly for large negative indices in the extreme non-linear regime but should suffice for the purpose of illustration.

Figure 6.11 shows the linearly extrapolated $\bar{\xi}$, the nonlinear $\bar{\xi}$ obtained from scaling relations and also the nonlinear $\bar{\xi}$ obtained from N-Body simulations for each of the six simulations listed in Table 6.1. The plots are for the late epoch corresponding to $r_{nl} = 8$ grid lengths in the model without a cutoff. We find that in cases with the natural cutoff of k_f, there is poor agreement between the simulated values and the analytical estimate. This is true even for the linearly extrapolated estimate and we believe it is caused by a few large scale modes with exceptionally high power. Simulations with an imposed cutoff agree well with the analytical predictions at scales where $\bar{\xi} \leq 10$, though there is some divergence at larger scales. Given that the disagreement occurs for the A1 and B1 simulations and can be seen in $\bar{\xi}$ as well as S_3, but there is no serious disagreement for simulations A2, A3, B2 and B3, we feel that our interpretation is correct. Further, we may claim that the method outlined for estimating the effect of box size in the linearly extrapolated $\bar{\xi}$, S_3, as well as the nonlinear $\bar{\xi}$ works fairly well, at least in the weakly non-linear regime.

6.4 Summary & Conclusions

In the present chapter we have studied the effects of a finite box size in cosmological N-body simulations on higher moments. Using the formalism which was developed in Chapter 4 we gave the expressions for corrections in Skewness and Kurtosis. We have presented the results of a set of cosmological N-body simulations which we have carried out to understand the effects of finite box size on physical quantiles. We have compared the theoretical estimates of the average two point correlations function, Skewness and number density of haloes and found a good agreements between these. In this chapter we have also studied the effects of finite box size in cosmological N-body simulations

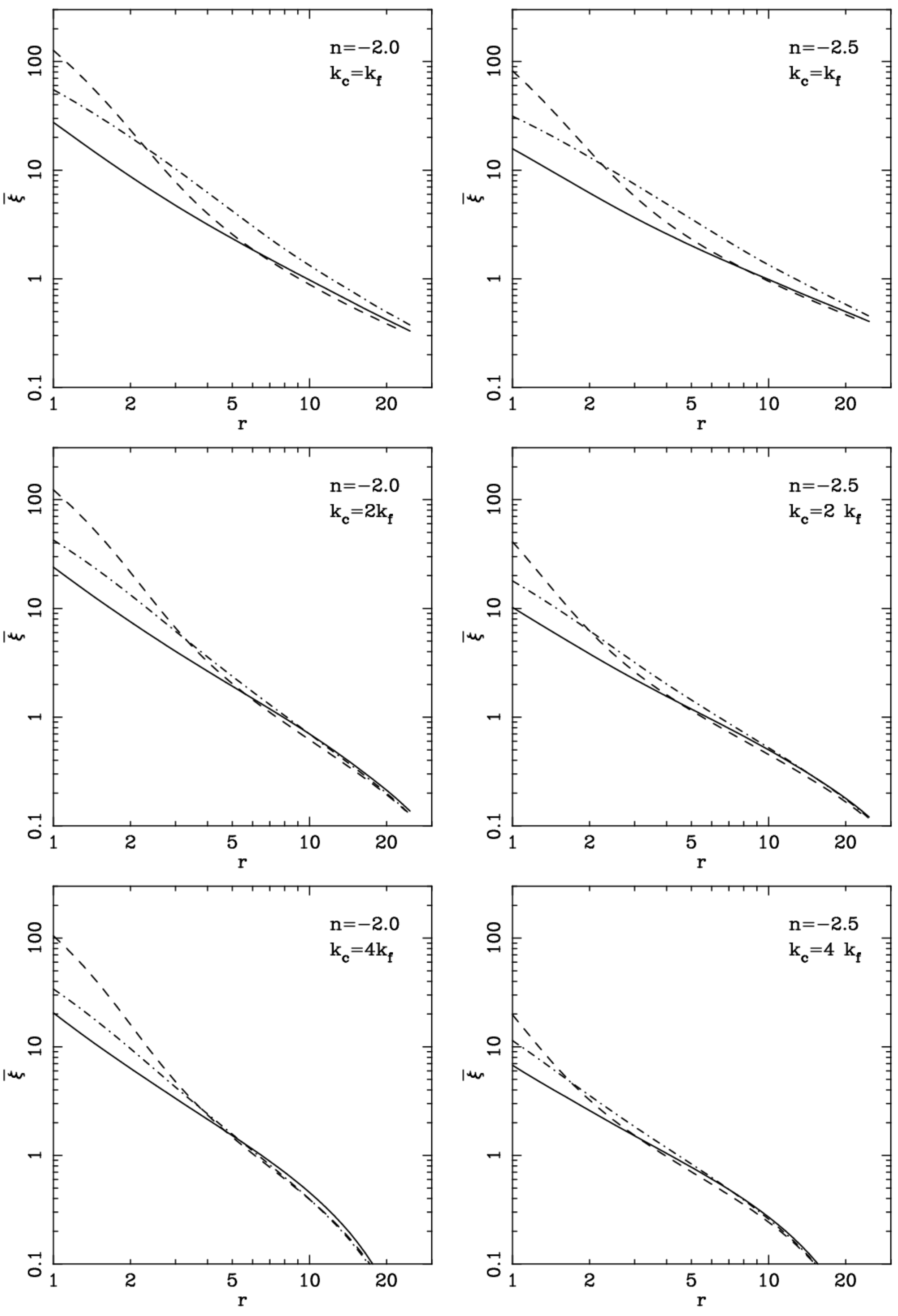

Figure 6.11: The left and right panels in this figure show the linear (solid line) and nonlinear (dot-dashed line) $\bar{\xi}$ average two point correlation functions from the simulations and estimated using the HKML procedure for models A1,A2,A3 and B1,B2,B3 respectively The first, second and third rows are for the models with $k_c = k_f$ (A1, B2), $k_c = 2k_f$ (A2, B2) and $k_c = 4k_f$ (A3, B3) respectively.

on pair velocity and nonlinear scaling relations.

The main conclusions of our present study may be summarized as follows:

- We have extended formalism for estimating the effects of a finite box size beyond the second moment of the density field. We have given explicit expressions for estimating the Skewness and Kurtosis in the weakly nonlinear regime when a model is simulated in a finite box size.
- We have tested the predictions of our formalism by comparing these with the values of physical quantities in N-Body simulations where the large scale modes are set to zero without changing the small scale modes.
- We find that the formalism makes accurate predictions for the finite box size effects on the averaged two point correlation function $\bar{\xi}$ and Skewness.
- We find that the formalism correctly predicts all the qualitative features of the mass function of a model simulated in a finite box size. In this case, we do not find a good quantitative match when the Press-Schechter mass function is used.
- We studied the effects of a finite box size on relative velocities. We find that the effects on relative velocities mirror the effects on $\bar{\xi}$.
- We argue that the formalism we have proposed for estimating corrections in the linearly extrapolated amplitude of clustering can be extended to the nonlinear regime with the help of nonlinear scaling relations.

Bibliography

Aarseth S. J., 2003, *Gravitational N-Body Simulations*, Cambridge University Press

Baertschiger T., Joyce M., Gabrielli A., Labini F. S., 2007a, PhRvE **75**, 059905

Baertschiger T., Joyce M., Gabrielli A., Labini F. S., 2007b, PhRvE **75**, 021113

Baertschiger T., Joyce M., Gabrielli A., Labini F. S., 2007c, PhRvE **76**, 011116

Bagla J. S., 2002, Journal of Astrophysics and Astronomy **23**, 185

Bagla J. S., 2005, Current Science, **88**, 1088

Bagla J. S., Padmanabhan T., 1994, MNRAS **266**, 227

Bagla J. S., Padmanabhan T., 1997a, Pramana - Journal of Physics, **49**, 161

Bagla J. S., Padmanabhan T., 1997b, MNRAS **286**, 1023

Bagla J. S., Prasad J., Ray S., 2005, MNRAS **360**, 194

Bagla J. S., Prasad J., 2006, MNRAS **370**, 993

Bagla J. S., Prasad J., 2008, ArXiv e-prints, 802, arXiv:0802.2796

Bagla J. S., Prasad J., Khandai N., 2008, ArXiv e-prints, 804, arXiv:0804.1197

Bagla J. S., Ray S., 2003, New Astronomy **8**, 665

Bagla J. S., Ray S., 2005, MNRAS **358**, 1076

Bagla J. S., Ray S., 2006, arXiv:astro-ph/0604598

Barnes J., Hut P., 1986, Nature **324**, 446

Barnes J., Hut P., 1989, ApJS **70**, 389

Bernardeau F., 1994, ApJ **433**, 1

Bernardeau F., Colombi S., Gaztaaga E., Scoccimarro R., 2002, Physics Reports **367**, 1

Bertschinger E., 1998, ARA&A **36**, 599

Blumenthal G. R., Faber S. M., Primack R. J., Rees M. J., 1984, Nature **311**, 517

Bond J. R., Cole S., Efstathiou G., Kaiser N., 1991, ApJ **379**, 440

Bond J. R., Myers S. T., 1996, ApJS **103**, 1

Bouchet F. R., Kanfrup H. E., 1985, ApJS **299**, 1

Bouchet F. R., Hernquist L., 1988, ApJS **68**, 521

Bower R. G., 1991, MNRAS **248**, 332

Brainerd T. G., Scherrer R. J., Villumsen J. V., 1993, ApJ **418**, 570

Carlberg R. G., 1990, ApJ **350**, 505

Chiu W. A., Ostriker J. P., 2000, ApJ **534**, 507

Cohn J. D., Bagla J. S., White M., 2001, MNRAS **325**, 1053

Colombi S., Bouchet F. R., Schaeffer R., 1994, A&A **281**, 301

Couchman H. M. P., Peebles P. J. E., 1998, ApJ **497**, 499

Davis D., Efstathiou G., Frenk C. S., White S. D. M., 1985, ApJ **292**, 371

Davis M. and Peebles P. J. E., 1977, ApJS **34**, 425

di Marco F., Finelli F., Gruppuso, A., 2007, PhRvD **76**, 043530

Diemand J., Moore B., Stadel J., 2005, Nature **433**, 389

Dolag K., Borgani S., Schindler S., Diaferio A., Bykov A. M., 2008, SSRv, 26

Efstathiou G., Davis M., Frenk C. S., White S. D. M., 1985, ApJS **57**, 241

Evrard A. E., Crone M. M., 1992, ApJL **394**, 1E

Fiedmann A., 1922, Z. Physs. **10**, 377 1922, MNRAS **10**, 377

Gelb J. M., Bertschinger E., 1994a, ApJ **436**, 467

Gelb J. M., Bertschinger E., 1994b, ApJ **436**, 491

Gurbatov S. N., Saichev A. I., Shandarin S. F., 1989, MNRAS **236**, 385

Hamilton A. J. S., Kumar P., Lu E., Matthews A., 1991, ApJ **374**, 1

Hinshaw et al., 2003, ApJS **148**, 135

Hinshaw et al., 2007, ApJS **170**, 288

Hockney R. W., Eastwood J. W., 1988, *Computer simulation using particles*, Bristol

Hubble E., 1929, Proc. Nat. Acad. Sci. **15**, 168

Jain B., Bertschinger E., 1996, ApJ **456**, 43

Jain B., Bertschinger E., 1998, ApJ **509**, 517

Jain B., Mo H. J., White S. D. M., 1995, MNRAS **276L**, 25

Jenkins A., Frenk C. S., White S. D. M., Colberg J. M., Cole S., Evrard A. E., Couchman H. M. P., Yoshida N., 2001, MNRAS **321**, 372

Kauffmann G., Melott A. L., 1992, ApJ **393**, 415

Kitayama T., Suto Y., 1996, MNRAS **280**, 638

Klypin A. A., Melott A. L., 1992, ApJ **399**, 397

Kofman L. A., Shandarin S. F., 1988, Nature **334**, 129

Lacey C., Cole S., 1993, MNRAS **262**, 627L

Lacey C., Cole S., 1994, MNRAS **271**, 676L

Lematre G., 1931, MNRAS **91**, 483

Lematre G., 1931, MNRAS **91**, 490

Liddle A. R, Lyth D. H., 2000, *Cosmological Inflation and Large-Scale Structure*, Cambridge University Press

Little B., Weinberg D. H., Park C., 1991, MNRAS **253**, 295L

Lynden-Bell D., 1967, MNRAS **136**, 101L

Ma Chung-Pei, Bertschinger E., 2004, ApJ **612**, 28

Ma Chung-Pei, Boylan-Kolchin M., 2004, PhRvL **93**, 021301

Malquarti M., Leach S. M., Liddle A. R., 2004, PhRvD **69**, 063505

Matarrese S., Lucchin F., Moscardini L., Saez, D., 1992, MNRAS **259**, 437

Melott A. L., Shandarin S. F., Splinter R. J., Suto Y., 1997, ApJL **479**, 79

Monaco P., Theuns T., Taffoni G., Governato F., Quinn T., Stadel J., 2002a, ApJ **564**, 8

Monaco P., Theuns T., Taffoni G., 2002b, MNRAS **331**, 587

Nityananda R., Padmanabhan T., 1994, MNRAS **271**, 976

Padmanabhan T., 1993, *Structure Formation in the Universe*, Cambridge University Press

Padmanabhan T., 2002, *Theoretical Astrophysics, Volume III: Galaxies and Cosmology*, Cambridge University Press

Peacock J. A., 1999, *Cosmological Physics*, Cambridge University Press

Peacock J. A., Dodds S. J., 1994, 1994, MNRAS **267**, 1020

Peacock J. A. and Dodds, S. J., 1996, MNRAS **280**, L19

Peebles P. J. E., 1990, ApJ **365**, 27

Peebles P. J. E., 1985, ApJ **297**, 350

Peebles P. J. E., 1974, A&A **32**, 391

Peebles, P. J. E., 1993, *Principles of physical cosmology*, Princeton University Press

Peebles, P. J. E., 1980, *The large-scale structure of the universe*, Princeton University Press

Power C., and Knebe A., 2006, MNRAS **370**, 691

Prasad J., 2007, Journal of Astrophysics and Astronomy **28**, 117

Press W. H., Schechter P., 1974, ApJ **187**, 425

Ray S., Bagla J. S., (arXiv:astro-ph/0405220)

Robertson H. P., 1929, Proc. Nat. Acad. Sci. **15**, 822

Sasaki S. 1994, Pub. Astr. Soc. Japan **46**, 427

Sellwood J. A., 1987, ARA&A **25**, 151

Shandarin S. F., Zeldovich Y. B., 1989, RvMp **61**, 185

Sheth R., Mo. H. J., Tormen G., 2001, MNRAS **323**, 1

Sheth R., Tormen G., 1999, MNRAS **308**, 119

Smith et al., 2003, MNRAS **341**, 1311

Smoot et al., 1992, MNRAS **396**, 1

Splinter R. J., Melott A. L., Shandarin S. F., Suto Y., 1998, MNRAS **497**, 38

Subramanian K., 2000, ApJ **538**, 517

Taffoni G., Monaco P., Theuns T., 2002, MNRAS **333**, 623

Tormen G., Bertschinger E., 1996, ApJ **472**, 14

Valinia A, d Shapiro P. R., Martel H., Vishniac E. T., 1997, ApJ **479**, 46

Walker A. G., 1936, Proc. London Math. Soc **42**, 90

Warren M. S., Abazajian K., Holz D. E., Teodoro L., 2006, ApJ **646**, 881

Weinberg S., 1972, *Gravitation and Cosmology: Principles and Applications of the General Theory* *of Relativity*, Wiley

Weinberg D. H., 2001, MNRAS **328**, 311

Weinberg D. H., Gunn J. E., 1990, MNRAS **247**, 260

White S. D .M, Frenk C., 1991, ApJ **379**, 52

Zhao H., Hooper D., Angus G. W., Taylor J. E., Silk, J., 2007, MNRAS **654**, 697

Zeldovich Y. B., 1970, A&A **5**, 84

Zeldovich Y. B., 1965, Adv. Astron. Astrophys. 3, 241